DOE/ER/53241--T2

DOE/ER/53241--T2

DE91 012397

Measurement of Magnetic Properties of Confined Compact Toroid Plasma (Spheromak)

by

Fu-Kwun Hwang

Dissertation submitted to the Faculty of the Graduate School
of the University of Maryland in partial fulfillment
of the requirements for the degree of
Doctor of Philosophy
1991

FG05-86ER53241

Advisory Committee:
Professor Alan DeSilva, Chairman/Advisor
Professor Hans Griem
Professor Thomas Antonsen
Professor Charles Striffler
Associate Professor Richard Ellis

Dedication

To my family:
my parents, my wife and my son.

Acknowledgements

It has been a great pleasure to learn and study at the University of Maryland. I deeply appreciate all those who have helped make this work possible during the years of my thesis studies at the Laboratory for Plasma Research. First and foremost is my advisor, Professor Alan DeSilva, who not only provided me with his expertise in experimental plasma physics, but also guided me with inspiration and encouragement. Professor George Goldenbaum provided valuable guidance and advice, especially in the theoretical aspects of this work. I would like to recognize my committee members for their efforts in reviewing this work, Professor Hans Griem, Richard Ellis, Thomas Anotnsen and Charles Striffler. Special thanks to Dr. Cecil Chin-Fatt who shared with me his research knowledge during the day-to-day operations of the MS machine.

Thanks to Dr. John Finn who provided me with his Grad-Shafranov code and valuable suggestions, and to Dr. Roger Hess who maintained an excellent computer systems. My appreciation to Mr. Ken Diller and Mr. Dave Miller for their technical assistance. I am grateful to fellow graduate students Jean-Luc Gauvreau, Alex Filuk, Claude Côté and Bruce Barrow for friendship, helpful discussions and shared data. I would like to acknowledge the effort of Jean-Luc who read my first draft of this thesis. It has been a great pleasure to work in such an enjoyable group research enviroment.

Last but certainly not least, I would like to offer my deepest love and gratitude to my wife Farn-Yi who supported me through all the difficult times.

Contents

List of Tables

List of Figures

Chapter 1.
Introduction

Thermonuclear fusion reactions are the source of the energy of the sun and the other stars. Nuclear fusion reactions are also the most promising solution for our future energy source. The ideal of controlled thermonuclear fusion is to heat a plasma hot enough so that the kinetic energy of some ions can overcome the long range Coulomb repulsion force and approach each other closely enough such that the short-range nuclear attraction force can lead to the formation of a compound nucleus. For light nuclei with $A \lesssim 60$, the average binding energy per nucleon increases as the mass number A increases, and energy is released when the fusion reaction occurs. The most attractive reactions for use in a thermonuclear fusion reactor appear to be the D-D reaction and the D-T reaction.[1] Deuterium fuel is almost inexhaustible, which is its major advantage.

The kinetic energy required to place two nuclei at a distance of the sum of the nuclear radii $\sim 10^{-14}$m can be estimated from the electric potential energy, $E_p \sim Z_1 Z_2 e^2/4\pi\epsilon_0 r = 0.15 Z_1 Z_2$ MeV. While quantum mechanical tunneling allows the nuclear fusion reaction to occur at lower energy, however, it is still necessary to raise the mean energy of particles to high enough temperature that high reaction cross sections for the nuclear reactions are obtained. For the D-T reaction, the reaction rate is negligible for temperatures below 4 KeV.[2]

Particles in gases at such temperature will be fully ionized due to collisions and turn into the plasma state. The plasma has to be heated to high enough temperature and confined for a sufficiently long time that the thermonuclear reactions release more energy than that necessary to maintain the hot plasma.

The design of a controlled fusion reactor has been approached by two different methods. One is related to the fact that the nuclei have finite mass, their accelerations are finite, and therefore it will take a finite time to disassemble when they are heated to high temperature. The fuel needs to be compressed to extremely high density in a small volume, $n \sim 10^{32}\mathrm{m}^{-3}$ which

is $\sim 5 \times 10^3$ denser than liquid DT, so that the fusion reactions can occur before the plasma expands significantly. This is called inertial fusion.[3] Another approach is to use fuel at much lower density ($\sim 10^{20}$ m^{-3}) in a larger volume and the plasma is confined by use of the magnetic field, which is called magnetic fusion. The condition for the fusion reactor to have net energy output is described by Lawson's parameter $n\tau_E$, where n is the plasma density and τ_E is the energy confinement time. At break-even condition, $n\tau_E = f(T)$, where typically $f(T) \sim 2 \times 10^{20}$m^{-3}sec for the optimized temperature $T \sim 20$ KeV.[4]

1.1. Magnetic Fusion

The plasma can be held away from the reactor walls by making use of the fact that free electrons and the bare nuclei move in spirals around the magnetic field lines. There have been several magnetic fusion confinement concepts developed. The ideal of a "magnetic mirror" utilizes the fact that charged particles spiraling along magnetic field lines tend to be reflected by a region of stronger magnetic fields. Plasma is confined between pairs of such mirrors. This is the linear or "open" type device in which magnetic field lines thread the plasma and terminate on the walls. Another approach is by wrapping the field lines into a torus, to eliminate the open field lines and keep the hot plasma away from the walls. The curved toroidal field lines, however, cause the particles to drift up or down, according to their charge states. The resulting charge separation will create an electric field, and the resulting $\vec{E} \times \vec{B}$ drift will dump all the particles to the outer wall of the ring. In order to generate closed magnetic surfaces in a torus, to compensate for outward drifts, and to provide MHD equilibrium, it is necessary to keep the magnetic field lines from closing on themselves after one pass around the torus by introducing a poloidal field in addition to the original toroidal field. This is the toroidal or "closed" type device in which magnetic field lines remain within the plasma volume. Several different devices have been developed to confine the plasma utilizing such a concept.[1]

- Stellarator: Both the toroidal field and the poloidal field are supplied by complicated external coils. The plasma is strongly constrained by the applied field. There is also a similar type of confinement device called the Torsatron.
- Tokamak: The toroidal component of the field is applied by external coils. The poloidal magnetic field, which is relatively weak compared to the toroidal field, is provided by the plasma currents. The plasma is free to distribute itself and adjust the toroidal current profile.
- Reversed field pinch (RFP): This is a device similar to the tokamak with approximately equal mean values of the poloidal and toroidal fields. The feature of the RFP is that the toroidal field has opposite directions on the inside and outside of the plasma column, and requires a close fitting conducting shell for stability.

The tokamak is the most technologically advanced fusion confinement device to date. A confinement parameter $n\tau_E \sim 10^{20}$ with plasma temperature ≥ 20 KeV has been reported.[5-6] A self-heated fusion plasma experiment is under design.[7] However, there are some inherent difficulties to develop the tokamak into an economic fusion reactor which are associated with the large size of tokamaks, their low power density and their relatively complex topology.

Spheromak is a compact toroid device which combines the favorable confinement properties of both the closed and open field line configurations.[8] A closed field line structure is formed in an axisymmetric mirror. This mirror provides the necessary external confinement field. Within the closed field lines, the toroidal magnetic field is generated entirely by the plasma current and most of the poloidal field is produced by the toroidal plasma current. The plasma is less constrained than in the tokamak and can adjust itself to form the lowest available magnetic energy state.

The spheromak is one of the most promising alternate confinement concepts. There are several advantages to choose the spheromak in the design of

an economic fusion reactor. Unlike the tokamak, there is no need of toroidal magnetic field coils linked through the center of the plasma. Spheromak is a much simpler configuration which would simplify the design and maintenance of the reactor. It is also possible to form the plasma in one region and translate it to a separate reactor region. The external magnetic field which is needed to confine the spheromak is much smaller than the magnetic field at the center of the spheromak, and it is possible to obtain higher internal field with appreciably smaller currents in the external coils than in the tokamak. All these features make the spheromak a very attractive fusion device. So far, however, the confinement and stability properties of this configuration have not been well established in experiment.

1.2. Spheromak Experiments

Spheromak plasma was first produced by a combination of theta and Z-pinch discharges (θ &Z) at the University of Maryland.[9] Since that time, a number of machines have been constructed to pursue the research. Even though a number of different formation schemes were used to form the plasma, the same spheromak configurations were produced; there are the θ-pinch & Z-pinch (θ & Z),[9] the flux core Electrodeless Induction (EI),[10] the Magnetized Coaxial Gun (MCG),[11] and the kinked Z-pinch.[12]

Table 1.1 lists some of the most recent efforts. The θ-pinch & Z-pinch formation scheme will be described in Chapter 3. The experiments listed in Table 1.1 and their formation schemes are discussed extensively in the literature.[10–16]

One of the most important scientific results that has come out of the spheromak experimental research is the verification of Taylor's relaxation theory (see Chapter 2 for more detail). The basic idea of such theory is that the plasma has a tendency to relax toward a force-free, minimum-energy state. The magnetic field profiles of the plasma are essentially independent of the

Institution	Univ. of Maryland	LANL	PPPL	Osaka Univ.
Device	MS[13]	CTX[14]	S-1[15]	CTCC[16]
Flux container(m)	.76 × .51	.67 × .67	.30 × .55	.20 × .25
Plasma current (MA)	0.8	1.0	0.3	0.1
Duration(msec)	0.4	2.0	1.0	0.8
Peak T_e(eV)	15	80	$\leq$ 100	40
density ($10^{20}m^{-3}$)	8.	0.45	0.5	0.5
Formation	θ&Z	MCG	EI	MCG

* LANL *(Los Alamos National Laboratory)*
* PPPL *(Princeton Plasma Physics laboratory)*

Table 1.1: Spheromak Experiments.

particular experiment or the previous history of the discharge. Taylor's theory first successfully explained the magnetic profiles in the RFP experiments, and later, has been applied in the spheromak research. The early experiments have demonstrated the ability to stabilize the spheromak against its most common magnetohydrodynamic (MHD) tilt and shift modes[17,18] by either using a conducting flux conserver or conducting coils ("figure-8" coils) at the plasma boundary,[19] or conducting cones on the axis of the plasma.[20] The early spheromaks produced were all reported to have radiation dominated cold plasmas, with electron temperature ranging from 10 to 20 eV.[21] The dominant factor which limited the temperature of the spheromak, was the low Z impurities, mostly carbon and oxygen.[22]

Because of the low temperature of the spheromak, the resistivity of the plasma became large and drove the plasma current to decay rapidly. The early experiments all had plasma life times less than 200 μsec. The most recent efforts were devoted to burn through the low Z radiation barrier, and to study the plasma at higher temperature with longer confinement time. Spheromaks with 100 eV electron temperature and plasma life time up to 2 msec have been reported.[14,15]

There have been a series of experiments designed to study the physics of spheromak at the University of Maryland. The previous experiments are PS-1, PS-2,[23] PS-3 and PS-3.5,[24] where PS means Paramagnetic Spheromak. The

MS and PS comparison				
Machine	Main chamber volume(ℓ)	Formation time(μsec)	Plasma life time(μsec)	Chamber material
PS-3.5	50.	10	50	pyrex glass
MS	600.	100	400	stainless steel

Table 1.2: Major differences between MS & PS.

current experiment is called the Maryland Spheromak (MS). The principal differences between the latest PS and MS are listed in Table 1.2.

The earlier PS experiments are characterized by fast θ-pinch/Z-pinch formation schemes. To avoid instabilities, and to keep the current density on electrodes small, a slow, inductive formation scheme was developed[25] and was proven to successfully form a spheromak.

The main objectives of the MS research program are

- To study the formation of ohmically heated spheromak with the new slow formation scheme.
- To study the physics of the spheromak configurations in the regimes where the radiation barrier has been exceeded.

The construction of the machine was finished in 1986. In early 1988, the plasma produced had configuration lifetimes of about 150μsec and 3 kilo-Gauss(kG) peak poloidal field. At that time, the plasma was forming initially off-center, and then drifting, generally further off center. The direction of the offset was consistently the same. Numerous passive stabilizing techniques were tried without much success. From the analysis of the fields obtained from the magnetic probe measurements, two modifications were made to the machine, resulting in major improvement in the plasma condition. First, the global shift of the plasma was eliminated by completely insulating the reversal coils of the machine to prevent any direct contact with the plasma. An axisymmetric plasma configuration with similar field strength was obtained. Then, attempts were made to modify the I_z discharge current paths, which led to the production of 10 kG field plasma. The details of these processes are all described in Chapter 5.

However, it is still a radiation dominated cold plasma with electron temperature ~ 15 eV. The limiting factors are the high plasma density (electron density $\sim 6 - 8 \times 10^{20} \mathrm{m}^{-3}$) and the presence of low-Z impurities (mainly carbon and oxygen).[26] The most recent MS studies have been concentrated on burning through the radiation barrier.

Magnetic helicity, which measures the linkage of the poloidal field and the toroidal field lines, describes the global topological property of the magnetic field structure.[27] Magnetic helicity injection is an important factor to be considered in the formation scheme and has been verified to be able to sustain the plasma.[28] Helicity injection as a means of current drive, and steady state operation is of great interest in the Tokamak, RFP and the compact toroid communities.[29–31] Current drive by injecting small spheromaks into the tokamak as a magnetic helicity injection process has been reported.[32]

This thesis describes studies of the magnetic field structure of the MS spheromak. The magnetic field structure of the plasma has been mapped out by arrays of passive magnetic pickup coils. Magnetic field configurations close to the Taylor's force-free states have been observed. Magnetic flux conversion between the toroidal field and the poloidal field during the formation phase of the spheromak was witnessed. Amplification of the poloidal magnetic flux was also seen in MS.

A numerical code first written by John Finn was modified to satisfy the boundary condition of the MS experiment. Axisymmetric equilibrium states that could exist in the MS configuration are calculated for various assumptions of the plasma pressure and the poloidal current profiles. Results from the Grad-Shafranov axisymmetry equilibrium code calculations are compared with the experimental measurements. Magnetic helicity for the axisymmetric system is studied and compared with the experimental results.

1.3. Outline of Thesis

The theoretical aspect of the spheromak is described in the next chapter. In chapter 3, the MS machine hardware will be explored along with the formation scheme and diagnostic systems.The magnetic pickup probes, their calibration procedures and the data analysis methods will be illustrated in chapter 4. Observations from the probe measurements are discussed in Chapter 5. In chapter 6, magnetic properties of the MS spheromak are studied. The axisymmetric Grad-Shafranov equilibrium code calculations are presented in chapter 7 and compared with the measurements. Magnetic helicity and its correlation with the experimental observations is described in chapter 8. The final chapter summarizes the main results and conclusions.

Chapter 2.
Spheromak

The first section covers a brief review of Taylor's relaxation theory.[33] The magnetic field structure of the ideal spheromak is described in the next section, followed by the magnetic properties of the axisymmetric equilibrium state.

2.1. Taylor's Relaxation Theory

For an ideal plasma which resembles a perfect conducting fluid,

$$\vec{E} + \vec{V} \times \vec{B} = 0.$$

where $\vec{V}$ is the fluid velocity, $\vec{E}$ and $\vec{B}$ are the electric field and the magnetic field respectively. This lead to the famous **frozen in theorem** which states that each magnetic field line maintains its identity and the magnetic flux through any closed contour moving with the fluid is a conserved quantity.

For plasma with linked fluxes, the above constraint can be expressed in terms of a new volume integral: "magnetic helicity"

$$H(\alpha,\beta) = \frac{1}{2\mu_0}\int_{\alpha,\beta} \vec{A}\cdot\vec{B}\,d\tau \tag{2.1}$$

where α, β are labels for the magnetic field lines and τ is the volume of the two flux tubes. Magnetic helicity describes the linkage of the magnetic field lines inside a magnetic surface.[34] For two localized and untwisted closed flux tubes linked once, other than the scalar factor, it is the product of the linked fluxes.

$$\begin{aligned} H &= \frac{1}{2\mu_0}\left(\int_{\tau_1} \vec{A}\cdot\vec{\ell}\;\vec{B}\cdot d\vec{S} + \int_{\tau_2} \vec{A}\cdot\vec{\ell}\;\vec{B}\cdot d\vec{S}\right) \\ &= \frac{1}{\mu_0}\Psi_1\Psi_2. \end{aligned}$$

where Ψ_1, Ψ_2 is the flux contained in each tube. The new constraint states that if one flux tube initially links with another flux n-times then in a perfectly conducting plasma the two fluxes must remain linked n-times during any plasma motion.

The equilibrium state of the plasma can be obtained by minimizing the magnetic energy,

$$W = \frac{1}{2\mu_0} \int_\tau B^2 \, d\tau \tag{2.2}$$

subject to the above constraint for every flux tube. We can find that the equilibrium state satisfies

$$\nabla \times \vec{B} = k\vec{B}. \tag{2.3}$$

for a flux tube, where k is different for each flux tube. This implies that the equilibrium state depends on every detail of the initial state.

The ingenious insight by Taylor was that : in the presence of finite resistivity, magnetic field lines are no longer "frozen-in" the plasma. In a time scale short compared with the resistive diffusion time, plasma relaxation occurs, which involves breaking and reconnecting of the magnetic field lines. Because it is no longer possible to identify the field lines, all the above invariants become invalid. However, the constraint applied globally is independent of the need to identify field lines and is still a good invariant as long as the resistivity is small. The relaxed state of the plasma with small resistivity is only subject to a single constraint: The total magnetic helicity integral over the whole plasma volume is invariant.

$$H = \frac{1}{2\mu_0} \int_\tau \vec{A} \cdot \vec{B} \, d\tau \tag{2.4}$$

The corresponding equilibrium satisfies Eq. (2.3) which is a force-free state, but with k the same everywhere. This equilibrium state is essentially independent of the details of the initial conditions of the plasma and can be solved subject to the appropriate boundary conditions. The solution of a force-free plasma enclosed in a spherical boundary is the classical spheromak and will be described in the next section.

2.2. Force Free Spheromak

The spheromak was observed always relaxed to the minimum magnetic energy state allowed by a given magnetic helicity, as described by Taylor's relaxation theory. For plasma in equilibrium,

$$\nabla P = \vec{J} \times \vec{B} \qquad \text{and} \qquad \mu_0 \vec{J} = \nabla \times \vec{B} \tag{2.5}$$

The ideal spheromak is a force-free configuration which satisfies

$$\mu_0 \vec{J} = k\vec{B} \tag{2.6}$$

where k is a constant, independent of position. The magnetic field can be expanded in terms of spherical scalar eigenfunctions

$$\Psi_m^n = j_m(kr)\, P_m^n(\cos\theta)\, e^{in\phi} \qquad \text{which satisfy} \qquad \nabla^2\Psi + k^2\Psi = 0$$

where $P_m^n(x)$ is the associated Legendre function, $j_m(x)$ is the spherical Bessel function. Then the magnetic field can be written as[35]

$$\begin{aligned}
\vec{B} =& \vec{r} \times \nabla\Psi + \frac{1}{k}\nabla \times \vec{r} \times \nabla\Psi \\
=& \sum_{m=0}^{\infty} \sum_{n=-m}^{m} b_m^n e^{in\phi} \left\{ \left[m(m+1)\, P_m^n \frac{j_m(kr)}{kr} \right] \hat{e}_r \right. \\
&+ \left[\frac{in}{\sin\theta} P_m^n j_m - \sin\theta P_m^{n\prime} \frac{1}{kr} \frac{\mathrm{d}}{\mathrm{dr}} (r j_m) \right] \hat{e}_\theta \\
&\left. + \left[\sin\theta P_m^{n\prime} j_m + \frac{in}{\sin\theta} P_m^n \frac{1}{kr} \frac{\mathrm{d}}{\mathrm{dr}} (r j_m) \right] \hat{e}_\phi \right\}
\end{aligned}$$

where, $P_m^{n\prime} = \frac{\mathrm{d}}{\mathrm{dx}} P_m^n(x)$.

The classical spheromak equilibrium solution is given by $m = 1, n = 0$.

$$\begin{aligned}
\vec{B}_r &= 3B_c \cos\theta \frac{j_1(kr)}{kr} \\
\vec{B}_\theta &= -1.5B_c \sin\theta \left(j_0(kr) - \frac{j_1(kr)}{kr} \right) \\
\vec{B}_\phi &= 1.5B_c \sin\theta\, j_1(kr)
\end{aligned} \tag{2.7}$$

where B_c is the magnetic field strength at the center of the spheromak. The boundary (separatrix) is given by the first zero of the spherical Bessel function

$j_1(x) : |k|R = 4.4934$. Notice that k can be either positive or negative which corresponds to positive or negative helicity spheromaks. The magnetic field outside the separatrix can be characterized by

$$\vec{B} = \nabla \left[\sum_{m=0}^{\infty} \sum_{n=-m}^{m} e^{in\phi} \left(a_{mn} r^m + b_{mn} r^{-(m+1)} \right) P_m^n \right]$$

For a classical spheromak, if we match the fields at the separatrix radius, the external magnetic field is

$$\begin{aligned} \vec{B}_r^{ext} &= j_0(kR)\, B_c \left(1 - \frac{R^3}{r^3}\right) \cos\theta \\ \vec{B}_\theta^{ext} &= -j_0(kR)\, B_c \left(1 + \frac{R^3}{2r^3}\right) \sin\theta \\ \vec{B}_\phi^{ext} &= 0. \end{aligned} \tag{2.8}$$

The magnetic field structure for the classical spheromak is shown in Fig. 2.1, and the parameters are calculated and listed in Table 2.1. A similar table has been presented by M. N. Bussac[35] at the *7th* international conference on plasma physics and controlled nuclear fusion research. However, the ratio between B_ϕ on the magnetic axis and the magnetic field at the center of the spheromak is believed to be a misprint (It was listed as 0.72). The total magnetic field energy is equally distributed between the poloidal field and the toroidal field. The magnetic axis is located at $kr = 2.744$ in the midplane, while the toroidal magnetic field peaks at a smaller radius $kr = 2.08$. Table 2.1 is very useful when combined with the experimental measurements to get a rough idea about the parameters of the plasma.

The total magnetic helicity of the classical spheromak is

$$\begin{aligned} H &= \frac{1}{2\mu_0} \int_\tau \vec{A} \cdot \vec{B}\, d\tau \\ &= \frac{1}{2\mu_0} \int_\tau \frac{B^2}{k}\, d\tau \\ &= W/k \end{aligned} \tag{2.9}$$

with $\vec{B} = \nabla \times \vec{A} = k\vec{A}$ and W is the total magnetic energy.

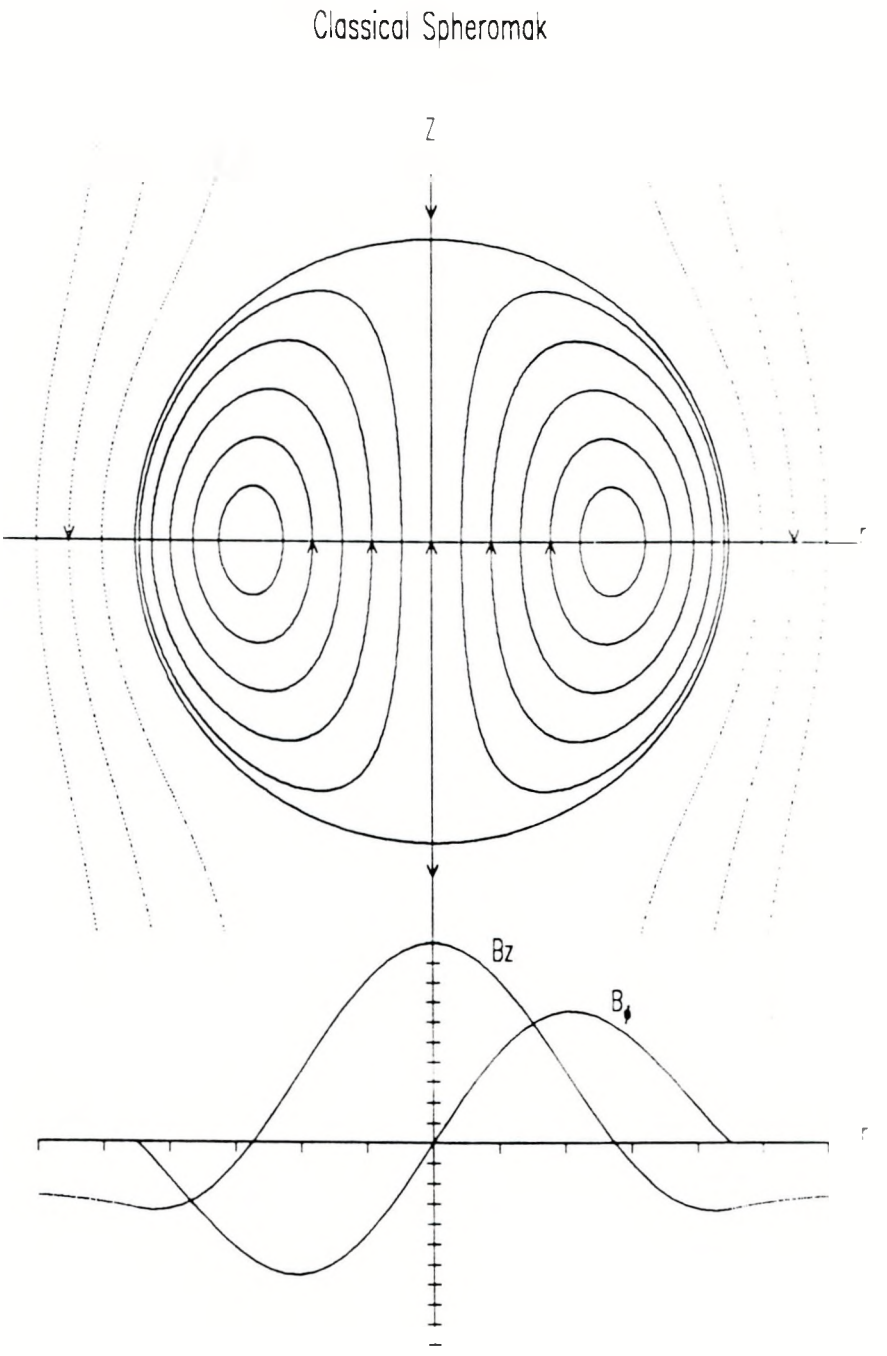

Figure 2.1: Poloidal flux contours of the classical spheromak and its magnetic field profiles on the midplane.

Parameters of the Classical Spheromak		
B_ϕ on magnetic axis	$0.58B_c$	Tesla
B_ϕ maximum	$0.65B_c$	Tesla
B_p at $r = R, \theta = \pi/2$	$0.33B_c$	Tesla
B_p at $r = \infty$	$-0.22B_c$	Tesla
Total toroidal current	$1.40B_cR$	MA
Total poloidal current	$1.74B_cR$	MA
Total poloidal flux	$0.49B_cR^2$	Weber
Magnetic energy $W_\phi = W_p$	$0.18B_c^2R^3$	MJ

* R(m) is the separatrix radius,
B_c(Tesla) is the magnetic field at the center of the spheromak.

Table 2.1: Parameters of the classical spheromak.

The magnetic moment of a plane circular current loop with radius a is $I(\pi a^2)$. For the classical spheromak, the magnetic moment due to the toroidal current is

$$\begin{aligned}\vec{M} &= \int J_\phi \pi \,(r\sin\theta)^2\, r\,dr\,d\theta\;\hat{z} \\ &= \frac{3\pi k B_c}{2\mu_0}\int_0^\pi \sin^3\theta\,d\theta\int_0^R r^3\, j_1(kr)\;dr\;\hat{z} \\ &= -\frac{2\pi}{\mu_0}B_c\, j_0(kR)\;R^3\;\hat{z} \end{aligned} \tag{2.10}$$

where $j_0(kR) = -0.217$. Notice that the external magnetic field consists of a uniform magnetic field of magnitude $j_0(kR)B_c$, plus a magnetic dipole field produced by the plasma (toroidal) current inside the separatrix.

$$\vec{B}^{ext} = j_0(kR)\,B_c\hat{z} - \frac{\mu_0}{4\pi}\frac{|\vec{M}|}{r^3}\left(2\cos\theta\,\hat{r} + \sin\theta\,\hat{\theta}\right). \tag{2.11}$$

This uniform magnetic field needs to be supplied from the external sources, and is much smaller than the peak field of the spheromak: this is one of the advantages of the spheromak confinement concept. The same uniform magnetic field also exists inside the separatrix. For the force free spheromak, the current density $\vec{J}$ is parallel to the total magnetic field inside the separatrix which is the sum of the magnetic field generated by the plasma current and the uniform external field. To have a force-free spheromak, we need either

an external current source or a metal boundary, which will generate an image current on the metal surface, in order to confine the plasma, as stated by the virial theorem.[36]

2.3. Axisymmetric Equilibrium

For axisymmetric systems, where the toroidal angle ϕ is an ignorable coordinate (*i.e.* $\frac{\partial}{\partial \phi} = 0.$), the vector fields can be represented by a toroidal component and a poloidal component. From Ampère's law,

$$\int_s \nabla \times \vec{\mathrm{B}} \cdot \mathrm{d}\vec{\mathrm{S}} = \int_s \mu_0 \vec{\mathrm{J}} \cdot \mathrm{d}\vec{\mathrm{S}}$$

$$\oint_c \vec{\mathrm{B}} \cdot \mathrm{d}\vec{\ell} = \mu_0 I \tag{2.12}$$

where I is the total current passing through an open surface S bounded by a closed curve c. For an axisymmetric field in a cylindrical coordinate system $(\hat{r}, \hat{\phi}, \hat{z})$,

$$\vec{\mathrm{B}}_\phi = \frac{\mu_0 I_p}{2\pi r} \hat{\phi} \tag{2.13}$$

$$\begin{aligned} \vec{\mathrm{J}}_p &= \frac{1}{\mu_0} \nabla \times \vec{\mathrm{B}}_\phi \\ &= \nabla I_p \times \frac{\hat{\phi}}{2\pi r} \end{aligned} \tag{2.14}$$

where indices ϕ and p represent the toroidal and poloidal components, respectively, and $\hat{\phi}$ is a unit vector. The poloidal component of a vector is its projection in the r-z plane. The poloidal current I_p is the total current flowing inside the radius r.

From the definition of the vector potential $\vec{\mathrm{A}}$,

$$\int_s \nabla \times \vec{\mathrm{A}} \cdot \mathrm{d}\vec{\mathrm{S}} = \int_s \vec{\mathrm{B}} \cdot \mathrm{d}\vec{\mathrm{S}}$$

$$\oint_c \vec{\mathrm{A}} \cdot \mathrm{d}\vec{\ell} = \Psi \tag{2.15}$$

where Ψ is the total magnetic flux enclosed within the closed curve c. Eq. (2.15) and Eq. (2.12) have similar mathematical forms, so

$$\vec{A}_\phi = \frac{\Psi}{2\pi r}\hat{\phi} \tag{2.16}$$

$$\vec{B}_p = \nabla\Psi \times \frac{\hat{\phi}}{2\pi r} \tag{2.17}$$

Equation (2.5) shows that the plasma is confined entirely by the magnetic force due to the interaction between the plasma current and the magnetic field. Taking the scalar product of Eq. (2.5) with $\hat{\phi}$,

$$\hat{\phi}\cdot\left(\vec{J}\times\vec{B}\right) = \hat{\phi}\cdot\nabla P = 0.$$

For axisymmetric plasma with scalar pressure in equilibrium, the poloidal current density is parallel to the poloidal magnetic field,

$$\mu_0\vec{J}_p = K\vec{B}_p \tag{2.18}$$

Taking the scalar product of Eq. (2.5) with $\vec{B}$ and $\vec{J}$ respectively, we have

$$\vec{B}\cdot\nabla P = 0.$$

$$\vec{J}\cdot\nabla P = 0.$$

These two equations show that in the equilibrium state, the magnetic field and the plasma current density lie on a constant pressure surface. This surface is also a magnetic flux surface, and therefore the current flows on magnetic flux surfaces (*i.e.* $P \equiv P(\Psi)$ and $I_p \equiv I_p(\Psi)$). The limiting magnetic flux surface, which approaches a single magnetic field line where the pressure is maximum, is called the magnetic axis. Combining Eqs. (2.14),(2.17) and (2.18), we have

$$\frac{J_p}{B_p} = I_p'(\Psi) \qquad \text{where } I_p' = \frac{dI_p}{d\Psi} \tag{2.19}$$

$$\begin{aligned}\nabla P &= \vec{J}_p\times\vec{B}_\phi + \vec{J}_\phi\times\vec{B}_p \\ &= \vec{B}_p\times\left(I_p'\vec{B}_\phi - \vec{J}_\phi\right) \\ &= -\frac{I_p'B_\phi - J_\phi}{2\pi r}\nabla\Psi\end{aligned}$$

$$\frac{J_\phi}{B_\phi} = I_p'(\Psi) - \frac{(2\pi r)^2 P'(\Psi)}{\mu_0 I_p(\Psi)} \tag{2.20}$$

where $P' = \frac{dP}{d\Psi}$. For axisymmetric equilibrium, J_p/B_p is a function of Ψ. However, J_ϕ/B_ϕ is not a function of Ψ unless $P' = 0$, which corresponds to the force free configuration case. In such case, $\mu_0 I_p' = k(\Psi)$, this represents the constraint for the equilibrium state. If k becomes a constant, then we have a Taylor minimum energy state and $\mu_0 I_p = k\Psi$.

From Eqs. (2.20) and (2.19), it follows that

$$\vec{J} = I_p' \vec{B} + 2\pi r P' \hat{\phi} \tag{2.21}$$

$$\nabla P = 2\pi r P' \hat{\phi} \times \vec{B}_p \tag{2.22}$$

The pressure gradient will vanish at the symmetry axis ($r = 0$) and at the magnetic axis, where the pressure has its maximum value.

$$\begin{aligned} J_\parallel/B &= \vec{J} \cdot \vec{B}/B^2 \\ &= I_p' \left(1 + \frac{\beta}{2} \frac{P'/P}{I_p'/I_p}\right) \end{aligned}$$

where $\beta = \frac{P}{B^2/2\mu_0}$. For the case where the plasma pressure profile is not too different from the poloidal current profile, $\frac{P'/P}{I_p'/I_p} \approx 1$, then $J_\parallel/B \approx I_p'(1 + \beta/2)$. Then, for low β devices, the equilibrium magnetic field structure observed would be similar to the force free plasma where $\beta = 0$.

We now proceed to rewrite Eq. (2.20) in terms of the flux function Ψ, in order to obtain the differential equation for the plasma equilibrium. J_ϕ may be written in terms of Ψ by use of Faraday's law and Eq. (2.17).

$$\begin{aligned} \mu_0 J_\phi &= \nabla \times \vec{B}_p \cdot \hat{\phi} \\ &= \frac{\partial}{\partial z}\left(-\frac{1}{2\pi r}\frac{\partial \Psi}{\partial z}\right) - \frac{\partial}{\partial r}\left(-\frac{1}{2\pi r}\frac{\partial \Psi}{\partial r}\right) \end{aligned} \tag{2.23}$$

The Grad-Shafranov equation expressing the plasma equilibrium then follows from Eqs. (2.20) and (2.13)

$$\begin{aligned} \triangle^* \Psi &= -2\pi r \mu_0 J_\phi \\ &= -(2\pi r)^2 \mu_0 P' - \mu_0^2 I_p I_p' \\ \triangle^* &= \frac{\partial^2}{\partial r^2} - \frac{1}{r}\frac{\partial}{\partial r} + \frac{\partial^2}{\partial z^2} \end{aligned} \tag{2.24}$$

This is a two dimensional, nonlinear, partial differential equation. Because of the nonlinearity, it must in general be solved numerically. The standard method is to specify the function, $P = P(\Psi)$ and $I_p = I_p(\Psi)$, the boundary condition or externally imposed constraints on Ψ, and then to invert the Laplacian-like operator $\triangle^*\Psi$ to determine $\Psi = \Psi(r, z)$. Numerical calculation of the Grad-Shafranov equation is described in Chapter 6.

Chapter 3.
Maryland Spheromak

The goal of the Maryland Spheromak Experiment is to produce plasma of temperature T$\sim$ 100 eV, density n$\sim 3\times10^{20}$m^{-3}, confinement time $\tau_E \sim$ 2msec and peak poloidal field $\sim$ 1 Tesla. The hardware description of the machine is covered in the first section, then follows the plasma formation scheme. The diagnostic systems for the experiment are described in the last section.

3.1. Machine Description

The MS machine is shown in Fig. 3.1. The machine is described in terms of the main vacuum vessel, bias coil system, reversal coil system, I_z electrodes and puff valves.

3.1.1 Main Vacuum Vessel

The main vacuum vessel, with a total volume of 818 ℓ, has three cylindrical sections. The central section is the plasma chamber. It is constructed from a 40 in. I.D., 0.75 in. wall thickness, 30 in. long cylinder. The two expansion sections, on each side of the plasma chamber, are constructed from 18 in. O.D., 0.25 in. wall thickness, 24 in. long cylinders. The two endplates, located between the plasma chamber and the expansion sections, are constructed from 2.5 in. thick stainless steel sheet. The vessel is constructed entirely from type 304L stainless steel. The vacuum chamber is pumped down through two ports located on the plasma chamber wall by two 6 in. turbo-molecular-pumps and a 8 in. cryo-pump at one end of the expansion chamber. Because of the strong magnetic field produced by the bias coils, the turbo pumps are located approximately 2.5 m away from the vessel. The cryo-pump thus has much higher effective pumping speed. The normal base pressure is $\lesssim 1\times10^{-7}$ Torr.

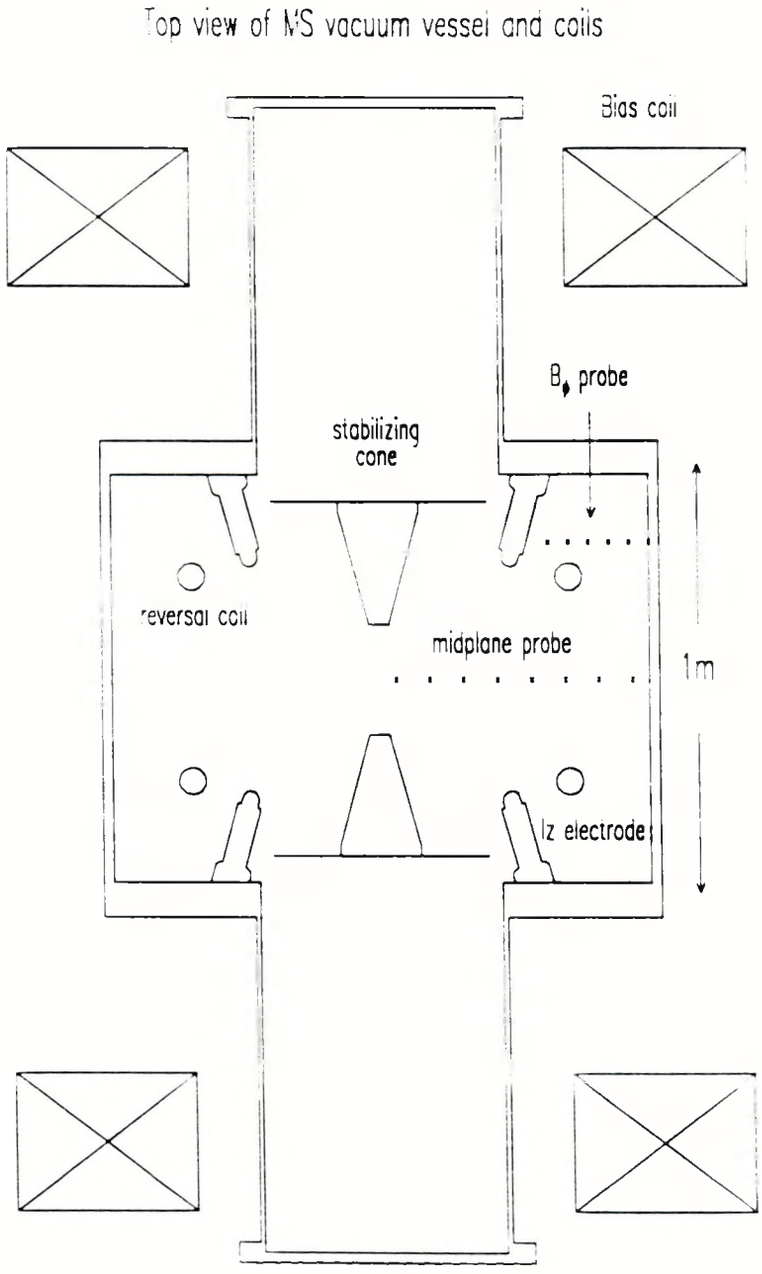

Figure 3.1: MS vacuum vessel and coils.

Bias coil system parameters		
liquid nitrogen cooled, high purity aluminium foil coils		
600 turns/coil (3 foil spirals, each 200 turns connected in series)		
DC power supply		
power consumption	< 1	MW
operating voltage	220	V
coil bore radius	31	cm
coil separation	$130 - 180$	cm
(L/R) decay time	9.7	sec
Max. design current	4.2×600	kA-turns/coil
Field on center	2.2	kG/kA-600turns
Current Flat Top Time	$1 - 10$	sec

Table 3.1: Bias coil system parameters.

3.1.2 Bias Coil System

The bias coils provide the external confinement field for the spheromak. The coils are operated in series, and are placed in a mirror configuration with their axes coinciding with the machine axis. The coil case is a liquid nitrogen dewar, capable of containing 200 gallons of liquid. Each coil has a resistance of 36 mΩ when it is cooled, and an inductance of $\sim$ 350 mH.

The parameters for the bias coil system are listed in Table 3.1.

3.1.3 Reversal Coil System

The two single turn coils, 28 in. major diameter, 2 in. minor diameter, located at 7.5 in. on both sides away from the midplane, are called the reversal coils. These two coils driven by a capacitor bank, reverse the magnetic field on the axis prior to the plasma formation. The reversal coils, along with the bias coils, form the closed field configuration in which the I_z discharge is initiated. The reversal capacitor bank is fired and crowbarred by ignitron switches, which are triggered through a series of firing circuits. During the normal operation, the reversal capacitor bank is crowbarred after a half cycle.

The parameters for the reversal coil system are listed in Table 3.2.

Reversal coil system parameters		
inductive load		
two single turn stainless steel coils		
coil major radius	35.56	cm
coil minor radius	2.54	cm
Max. charge voltage	+/−11	kV
total capacitance	24.6	mF
total stored energy	1.49	MJ
Max. output current	0.69	MA/coil
current rise time	90	μsec
total pulse time	180	μsec
Reversed field on center	11.6	kG/MA

Table 3.2: Reversal coil system parameters.

3.1.4 I_z Electrodes

There are 16 I_z electrode holders on each end of the vacuum vessel, symmetrically placed on a 20 in. circle. The I_z electrodes are located on a 15° half angle conical surface with its axis coinciding with the machine axis. The circuit is designed such that the vacuum vessel itself can act as a return path for the I_z current, resulting in a low inductance circuit. The electrode body is a 1.5 in. diameter, 10 in. long stainless steel cylinder. The electrode tips are constructed separately so that different materials can be used. Pure aluminum, stainless steel and Elkonite have been used as electrode material. The Elkonite electrode has shown much less damage as a result of repeated high I_z current discharges than the other electrode.

The parameters for the I_z electrode system are listed in Table 3.3.

3.1.5 Puff Valves

There are 4 pulsed gas puff valve holders on the endplate of each side of the plasma chamber, located in between the electrodes and the reversal coils. They are aimed toward the center of the plasma chamber. The function of the pulsed puff valves is to inject the main fill gas into the vacuum chamber vessel a few milliseconds before the start of the main discharge. Those puff

I_z electrode system parameters		
Max. charge voltage	20.0	kV
total capacitance	5.8	mF
total stored energy	1.2	MJ
Max. circuit current	1.5	MA
current rise time	80	μsec
number of electrodes	32	
electrode tip radius	25	cm
electrode tip material	Elkonite	

Table 3.3: I_z electrode system parameters.

valves were later replaced by 2 puff valves installed from the far endplates. The purpose was to have higher concentration of gas fill the center region of the vessel and less gas around the reversal coils. Some of the plasma shots have been taken with static fills by closing all the gate valves in front of the pumps.

3.2. Formation Scheme

The formation scheme of MS is a relative slow and inductive method when compared with the earlier PS fast θ-pinch & Z-pinch formation. It is best illustrated with Fig. 3.2.

1. The I_z capacitor bank and the reversal capacitor bank are charged to the preset voltages separately. The circuit is set up so that they both reach full charge at the same time.
2. The bias coils are energized to the desired current to produce the external confinement field. The bias current lasts for more than five seconds so that the magnetic field has enough time to penetrate the metal chamber wall. On the time scale of the plasma life time (less than 1 msec), the bias field acts as a DC magnetic field.
3. The gas, usually deuterium, is injected into the chamber 1-4 msec before the reversal bank is triggered. The amount of gas puffed

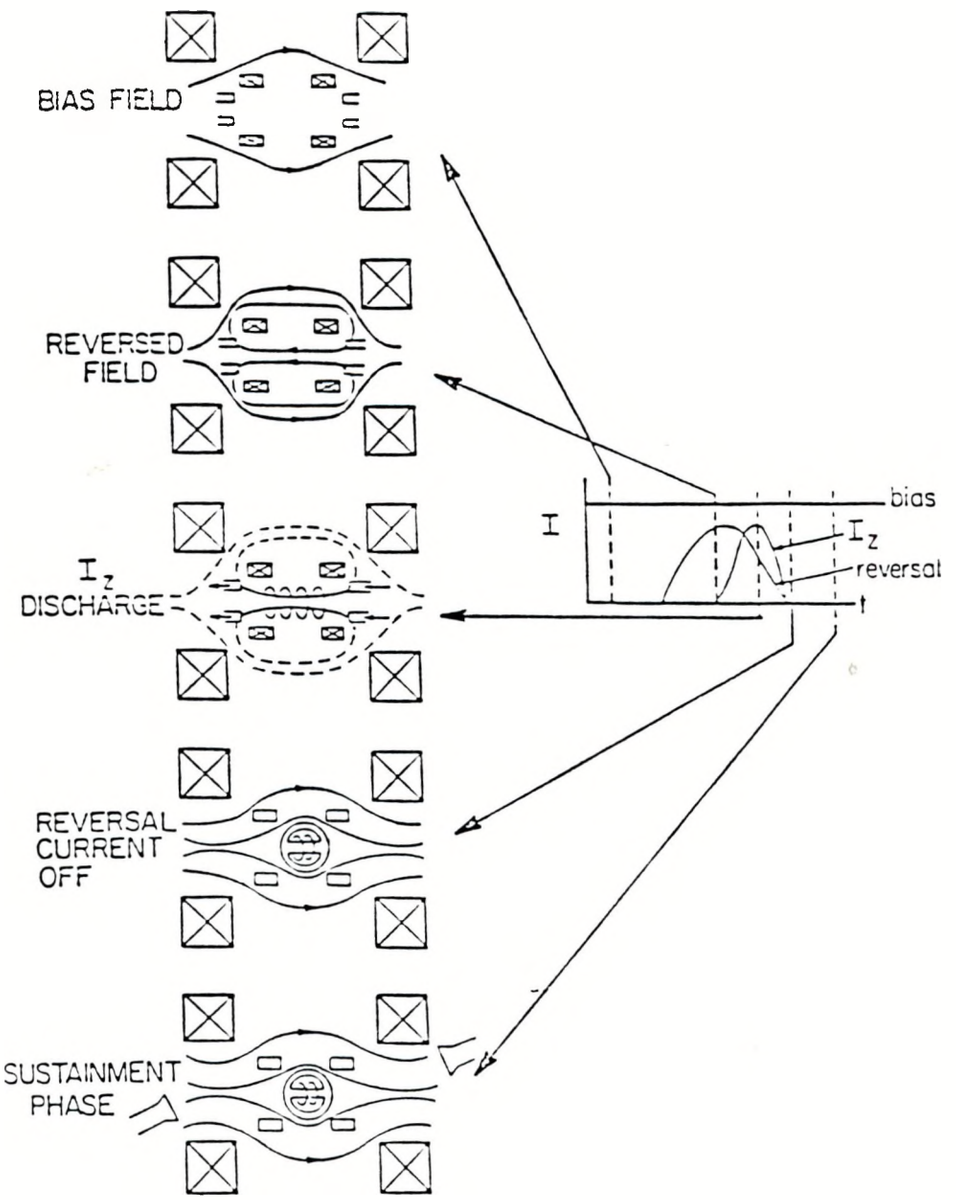

Figure 3.2: MS formation scheme.

into the system produces a static fill of about 3-12 mTorr in the chamber when all the pumps are isolated from the system.

4. The reversal coils are energized to reverse the magnetic field on axis. The rise time of the reversal coil current is about 90 μsec. The vacuum vessel acts as a flux conserver for the magnetic flux produced by the reversal coils, causing the bias flux to be pushed against the wall. The closed flux surfaces are formed inside the vacuum chamber. Figure 5.13 shows the vacuum poloidal flux surfaces produced by the bias coils and the reversal coils.
5. The I_z discharge triggered at the peak of the reversal current, forms the plasma and the toroidal field; the currents in the reversal coils then start to decay.
6. As the flux inside the reversal coils decreases in magnitude, an electric field is induced and drives the toroidal plasma current. When enough current is generated, the poloidal field inside the reversal coil is reversed; reconnection occurs and forms closed field lines within the coil. The reversal coil current usually is crowbarred to prevent the current from ringing over.
7. The relaxation process takes place and leads the plasma close to the minimum energy state; the spheromak is formed.
8. The spheromak starts to decay due to radiation loss of the energy and finite resistivity of the plasma.

3.3. Diagnostic Systems

Several diagnostic systems were installed on the machine to measure its performance. There are the machine operation monitors, density measurement, spectroscopic analysis and magnetic properties diagnostic. A Thomson scattering electron temperature/density apparatus were not operational at the moment, so there were no direct electron temperature measurements available when this study was performed.

3.3.1 Machine Operation Monitor

The following diagnostics are used to monitor the basic machine operations:

- The vacuum condition is monitored by an RF quadrupole residual gas analyzer along with standard vacuum gauges.
- The bias coil current is monitored by the voltage drop across a precision resistor inside the power supply. This current is used to calculate the bias field inside the vacuum, and added to the magnetic field measurement to obtain the total magnetic field at the probe location.
- The currents of the two reversal coils are measured by two Rogowski loops. Two other Rogowski loops are set up around all 16 I_z electrodes on each side of the vessel to measure the total I_z current. The total I_z current and reversal current wave forms are shown in Fig. 3.3.
- The voltage across the I_z electrodes is measured indirectly by two sets of RC compensated voltage dividers (11400:1 ratio). Each voltage divider measures the voltage between one of the electrodes on either side and the ground of the screen room. Each voltage probe is installed inside a copper cylinder tube and forms a coaxial circuit to prevent pickup.

3.3.2 Density Measurement

The line-integrated electron densities along chords at the midplane are measured by a He-Ne laser interferometer. The interferometry resolves the phase shift of light passing through the plasma, and the phase shift $\Delta\phi$ is linearly proportional to the line-integrated density. The phase shift may be expressed as

$$\begin{aligned}\Delta\phi &= \frac{\pi}{fc}\int f_{pe}^2\,d\ell \\ &= 1.78\times 10^{-22}\lambda_e L\end{aligned}$$

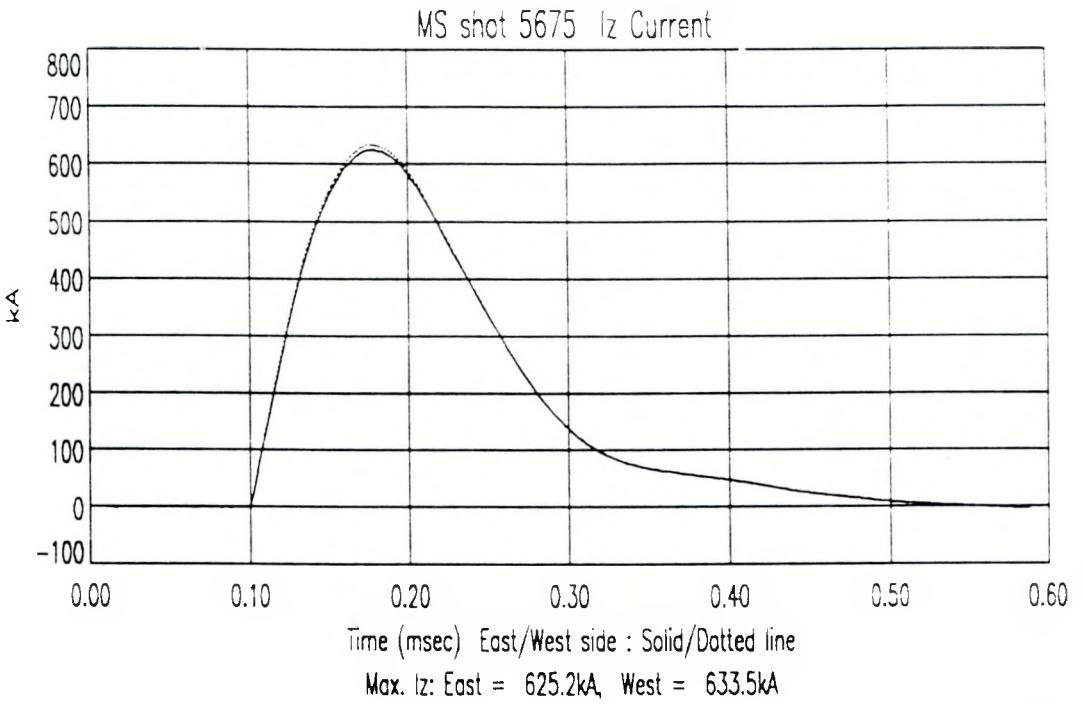

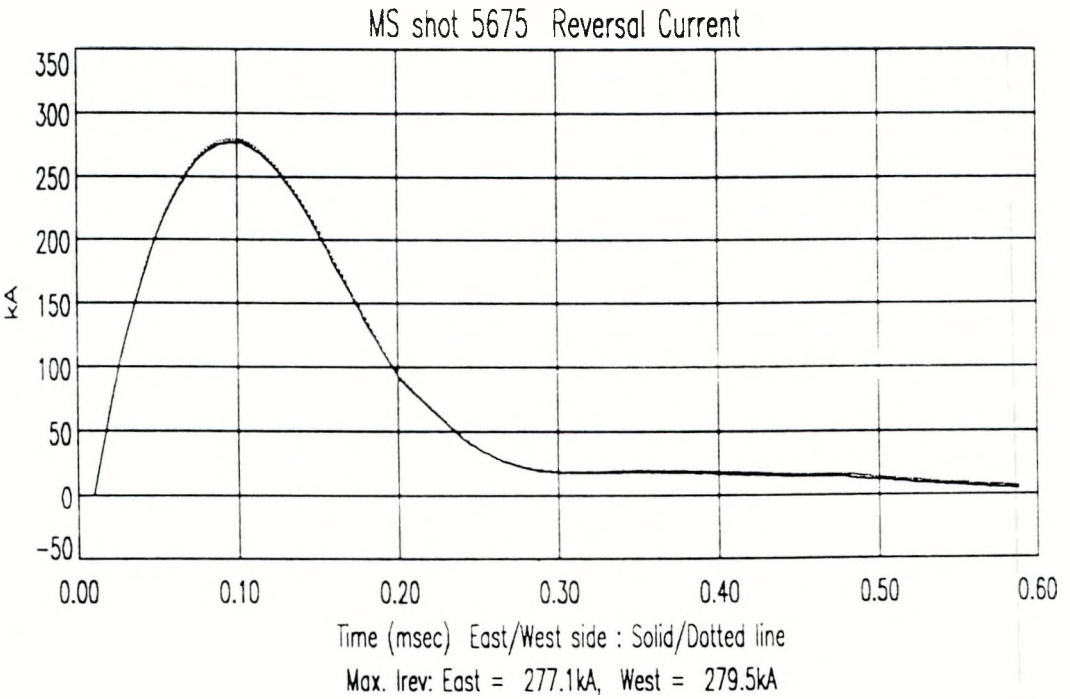

Figure 3.3: The total I_z current and reversal current wave forms.

where $f_{pe} = \sqrt{n_e e^2/4\pi^2\varepsilon_0 m_e}$ is the electron plasma frequency, $f = 4.74 \times 10^{14}\text{s}^{-1}$ is the laser light frequency (for visible light $\lambda = 6328\text{Å}$), $\bar{n}_e = \frac{1}{L}\int n_e \, d\ell$ is the line-averaged density in m^{-3}, and L is the total plasma path length in meters.

The laser beam was divided into a 4 channel system, mounted on an air-supported granite optical table, and the beams were set up to view chords across the lower half of the midplane of the plasma chamber. A total of 8 chords of line-integrated density can be obtained by moving the laser beam positions. With the assumption of cylindrical symmetry, the chord data $\bar{n}_e(L,t)$ are converted to density profiles $n(r,t)$ by an inversion technique. A typical temporal record of 4 interferometer chord line densities are shown in Fig. 6.14. An electric probe having 4 tips also has been used as double probe or triple probe to measure the local electron density near the wall.

3.3.3 Spectroscopy Analysis

A two dimensional Optical Multichannel Analyzer (OMA) was combined with a 1 meter spectrometer for the spectroscopy diagnostic, to measure the emission spectral lines from impurity radiation. The spatial and wavelength information of the plasma radiation can be obtained simultaneously. The OMA is sensitive over a broad range of the spectrum, from 2000Å to 8000Å. An optical rotating slit was added in front of the spectrometer entrance slit. The spatial resolution is then traded off for temporal information.[37]

Ion temperature is obtained from observed impurity spectral linewidths based upon the Doppler line broadening mechanism.[38] The ion temperatures of CIII, CIV and OIV roughly follow the I_z current in time. For OIV, $T_i > 100$ eV was observed during plasma formation in the center region of the plasma. An indication of the electron temperature range is obtained by examining the presence or absence of various ionization stages of impurities, mainly carbon and oxygen. Based on the highest ionization stage observed (OV), the maximum electron temperature is estimated to be $T_e \sim 15$ eV.

The main impurities observed are

- Carbon: the chamber has been discharge cleaned with methane.
- Oxygen: when the vessel was brought to air, oxygen could be absorbed in the walls. It also can come from minor air leaks into the system or water vapor being broken into oxygen and hydrogen.
- Aluminum: insulating supports for the electrodes are made of Alumina ceramic.
- Fluorine: This became present after the reversal coil was covered with teflon tape.
- Copper: "figure-8" coils used for stabilizing the plasma are made of copper.

3.3.4 Magnetic Properties Diagnostic

The magnetic field was measured by several sets of passive flux probes. Details of these diagnostics are presented in the next chapter.

Chapter 4.
Magnetic Probes

Several sets of passive magnetic probes have been constructed to diagnose the magnetic structure of the plasma. The principal diagnostic, other than spectroscopy before early 1988, was a six-position (with 7.62 cm spacing) magnetic flux probe inserted radially on the midplane of the machine. Each position has two passive pickup coils to measure the B_z field and the B_ϕ field on the midplane. This probe was later replaced by an eight-position (with 6.35 cm spacing) magnetic flux probe, and a thin stainless jacket (0.001 in. thickness) was used to cover the glass body of the probe to reduce possible impurities introduced from the probe into the plasma. For each plasma shot, temporal information of the magnetic field as a function of radius at the midplane is obtained. The data were interpreted assuming an axisymmetric plasma configuration, however, the plasma produced was suspected to have shift and/or tilt instabilities. It became impossible to understand the details of the configuration behavior with measurements only in the midplane when the plasma was not axisymmetric. To aid in understanding the details of the configuration behavior, another magnetic probe was constructed to allow more complete coverage of the interior of the machine when additional digitizers were available. This probe, which is called L-probe in this study, consists of seven sets of coils with 2.54 cm spacing. Each set of coils has three orthogonal coils so that all three components of the magnetic field can be obtained. The position of the first set of coils is 3.175 cm away from the "L" joint.

The L-probe is inserted radially from one of the diagnostic ports at the midplane, at an angle of 45 degrees with respect to the top of the vessel. By adjusting the location and/or orientation of the probe, the magnetic field structure on the R-Z plane or on the midplane of the vessel can be measured with multiple shot averaged scans (Fig. 4.1).

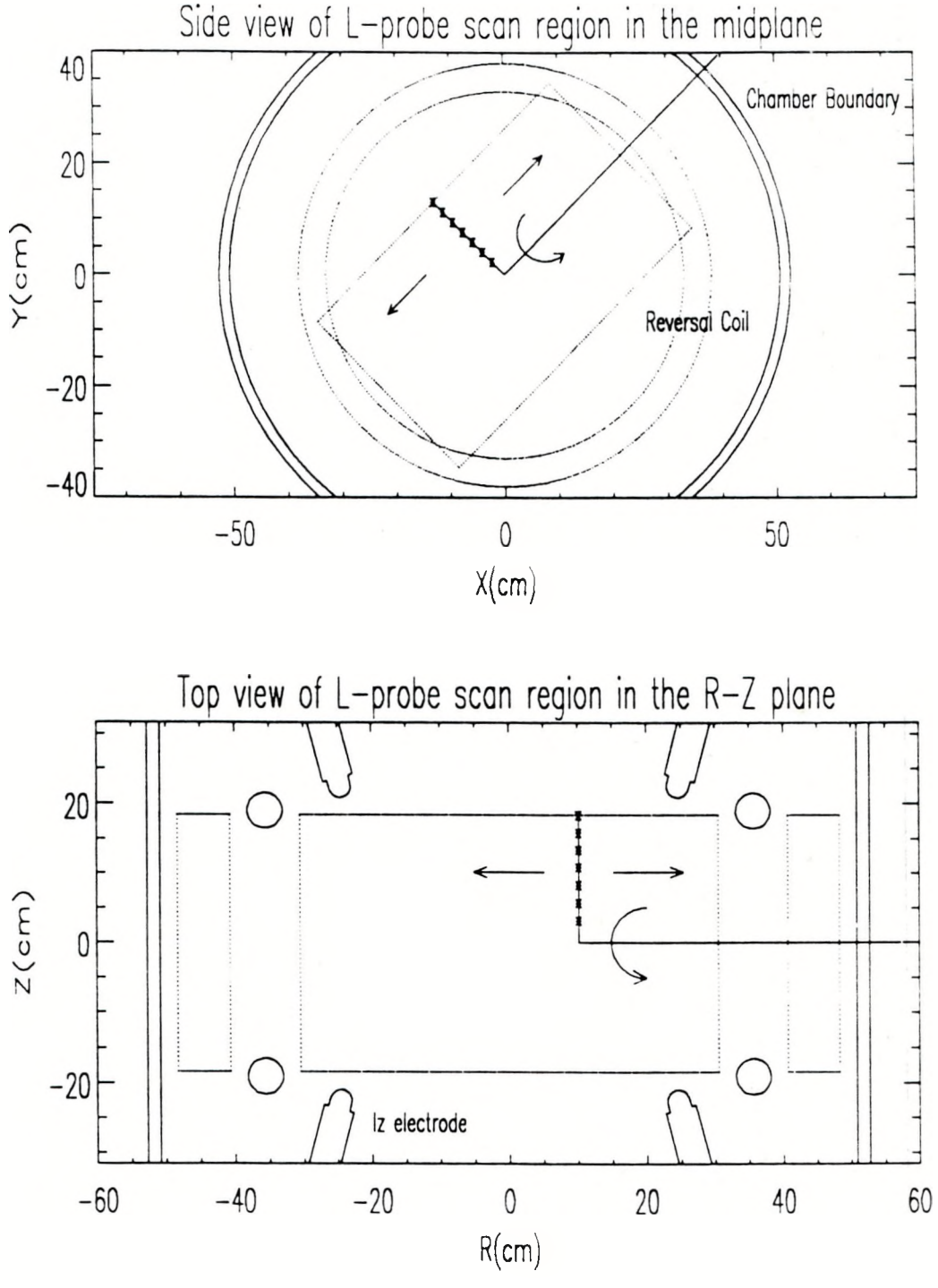

Figure 4.1: (a) Side view of the L-probe scan region in the midplane. (b) Top view of the L-probe scan region in the R-Z plane.

4.1. Probe Construction

The magnetic probes were designed to have as small size as possible to minimize the perturbations of the plasma, and at the same time to pick up large enough signals for processing. To facilitate winding, all the pickup coils for each probe were wound on a single lexan form with 5 mm space cross section with appropriate holes drilled in it (Fig. 4.2), to ensure the proper relative positions and orientations of the coils. Each coil was wound with #38 copper wire, with 18-22 turns per coil. The leads for each coils were then twisted to cancel pickup of magnetic flux along the leads. All the twisted pairs of leads at one end of the lexan form were bound together with some polyethylene shrink tubing and ran down inside a quarter inch O.D. copper tube to minimize the electrostatic pickup and to insulate from the outside magnetic fluxes. The lexan form and the copper tube were then installed inside a 9 mm O.D. glass tube and filled with epoxy. For the L-probe, the "L" joint was made from a machineable ceramic. All the leads were terminated inside a copper can, which was clamped on the copper tube, with a lemo-type socket in it. The signals were carried by coaxial cables plugged into each socket to the screen room.

4.2. Probe Calibration

The calibration for the magnetic probes was performed by measuring the effective area for each magnetic pickup coil. A Helmholtz coil with 8 cm O.D., 20 turns on each coil was made to measure the response of the probe. The magnetic field at the center of the Helmholtz coils is 4.5 Gauss/A. The current was supplied from a standard signal generator with a 40 kHz sinusoidal wave and measured by a Tektronix current probe. The current probe was also checked by connecting the signal to a precision resistor, and measuring the voltage across it, then comparing with the current signal response. The current signal and the probe response were both fed into a digitizer. The effective area was then calculated and stored into a file for later processing. The relative error of the effective areas obtained are between 1-2%, however,

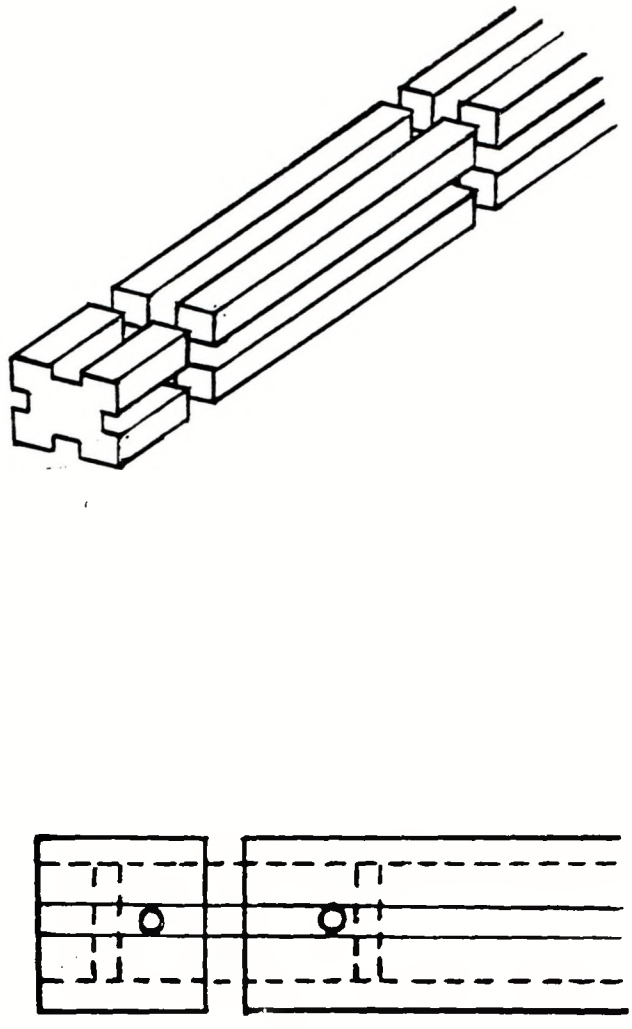

Figure 4.2: Lexan form used for building a magnetic probe.

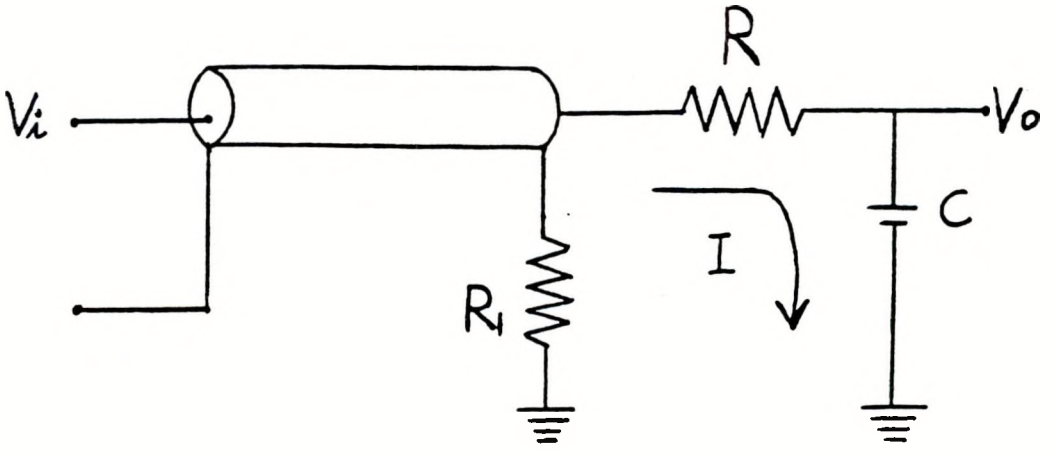

Figure 4.3: Equivalent circuit for the magnetic pickup coils. V_i is the probe signal, V_o is the signal input to the digitizer. R_1 is the 50Ω termination resistor.

the measured field could have 3-5% of error due to misalignment of the probe and noise pickup.

The vacuum field produced by the reversal coils can be calculated from the Grad-Shafranov code (Chapter 6). The magnetic field measured with the above calibration method, was compared with the Grad-Shafranov code calculation, when only the reversal bank was fired without any plasma current in the chamber. A good agreement was obtained, the deviation between the measured and calculated field was less than 4%.

4.3. Data Processing

Figure 4.3 shows the equivalent circuit for the magnetic probe signal measurement. The voltage signal is

$$V_i(x,t) = -\frac{\mathrm{d}}{\mathrm{d}t}\int_s \vec{B}\cdot\hat{n}\,\mathrm{d}S \simeq -S_{eff}\frac{\mathrm{d}}{\mathrm{d}t}B_\perp(x,t) \qquad (4.1)$$

where $B_\perp(x,t)$ is the component of the magnetic field $\vec{B}$ in the direction of the axis of the pickup coil at the coil position x, and S_{eff} gives the effective coil area, which is approximately the cross section of the coil multiplied by the number of turns. The output signal of the integrator is given by

$$V_o(T) = \frac{1}{C}\int_0^T I(t)\,dt = \frac{1}{RC}\int_0^T (V_i(t) - V_o(t))\,dt \qquad (4.2)$$

where RC is the integrator time constant. From Eqs. (4.1) and (4.2), the magnetic field can be calculated as

$$B(T) = -\frac{RC}{S_{eff}}\left(V_o(T) + \frac{1}{RC}\int_0^T V_o(t)\,dt\right) \qquad (4.3)$$

The second term, which contains the integration, usually is small compared to $V_o(t)$ if a large enough RC-integrator is used. However, large RC will also reduce the magnitude of the output signal.

The time constants of the RC-integrators are 1.0 millisecond for the midplane probe and 500 microseconds for the L-probe. The finite RC correction term was integrated numerically from the output signal of the RC-integrator for this study.

4.4. Data Collection Procedure

The passive pickup coil measures the rate of change of the magnetic flux inside the coil area. The signal was terminated with a 50Ω resistor to avoid reflection, then fed into a passive RC-integrator and finally connected to a digitizer. Those digitizers are 12 bits, with variable full scale range from 0.3125 to 5.0000 volts, and were made by the electronics shop at the University of Maryland. The clock for the digitizer is fed by a 500 kHz digital signal.

The midplane probe usually is located at fixed position on the midplane to monitor the plasma behavior. The L-probe is used to scan the magnetic field structure for given plasma conditions. For the R-Z plane scan, the probe stays on the R-Z plane at some radius to measure the time history of the magnetic field for different Z locations for a single shot. The data were taken at least

twice at each probe location and checked for consistency, the probe was then moved to a different radius. A similar procedure was used for the R-o scan on the midplane with the probe located on the midplane.

The magnetic field measured by the midplane probe indicated good reproducible plasma conditions. Shot-to-shot variation was normally less than 5%, and at most 10%. Some of the variations may be due to slight differences in bank voltages, e.g. the reversal current could have 1-3% shot-to-shot variation. The fractional shot-to-shot variations are about the same when the L-probe is moved to different locations during the magnetic field scans. The interferometer measurement indicated at most 5-10% electron density increases when the probes were located inside the plasma separatrix. The OMA impurity radiation measurements showed that the perturbation due to the probe were within shot-to-shot variations. This indicates that impurity emissions from the glass probe are small compared to impurities already present in the plasma. The midplane probe was later covered with a thin stainless steel jacket to reduce the boil-off from the surface of the glass probe which could inject impurities into the plasma. The signal shows no more than 1% attenuation in the signal and less than 4 microseconds delay in the probe signals which are due to the effect of the metal jacket.

Chapter 5.
Magnetic Field Measurements

This chapter describes observations and results obtained from the midplane probe and the L-probe. The first section covers the global shift of the plasma and how the problem was solved. Observation of current flowing in opposite direction to the main I_z discharge before the peak of the I_z current, will be discussed in the next section. In the last section, the effects of modifications to the I_z discharge current paths were studied. Plasma configurations with 10 kG magnetic field were obtained after properly controlling the I_z current path.

5.1. The Global Shift of the Plasma

The magnetic field measured on the midplane for MS shot 2307 is shown in Fig. 5.1. Notice that time t=0 is chosen to be 0.1 msec before the main I_z discharge is triggered. The DC offset of each B_z signal represents the magnetic field produced by the bias coils at the probe location. On the midplane, the magnetic axis can be identified as the position where the B_z field is zero. It appears to be located between 22-26 cm in radius (between coil #3 and coil #4) during t= 0.25-sim 0.35 msec (assuming an axisymmetric configuration).

The data at t=0.25 msec were compared with the magnetic field structure of the classical spheromak and are shown in Fig. 5.2. The B_ϕ fields of coils #5 and #6 are much larger than the fitted classical spheromak fields. This could be due to the I_z still having an appreciable amount of current flowing inside the vessel at t=0.25 msec. Assuming that all the current flowed inside coil #5, then the two triangles in Fig. 5.2 show the fields after subtracting contributions from the I_z current. The probe showed what was apparently a well formed spheromak configuration developing about 100 μsec after the axial I_z current was switched on. However, the plasma terminated suddenly in an interval of less than 10 μsec at about t=0.38 msec.

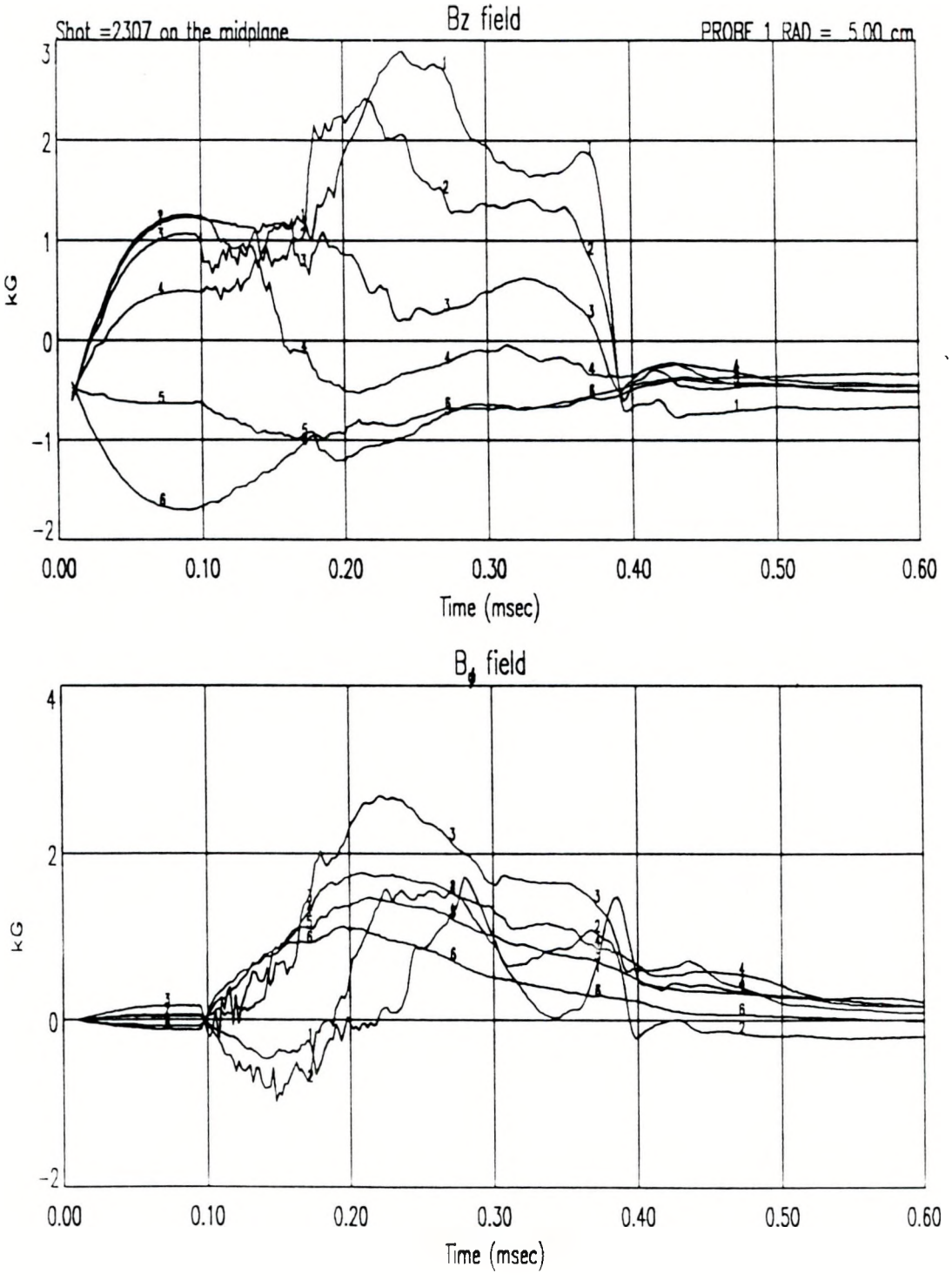

Figure 5.1: Magnetic fields measured with six-position magnetic flux probe on the midplane of the machine. Locations # 1-6 are at r=(5.0, 12.6, 20.2, 27.9, 35.5, 43.1) cm.

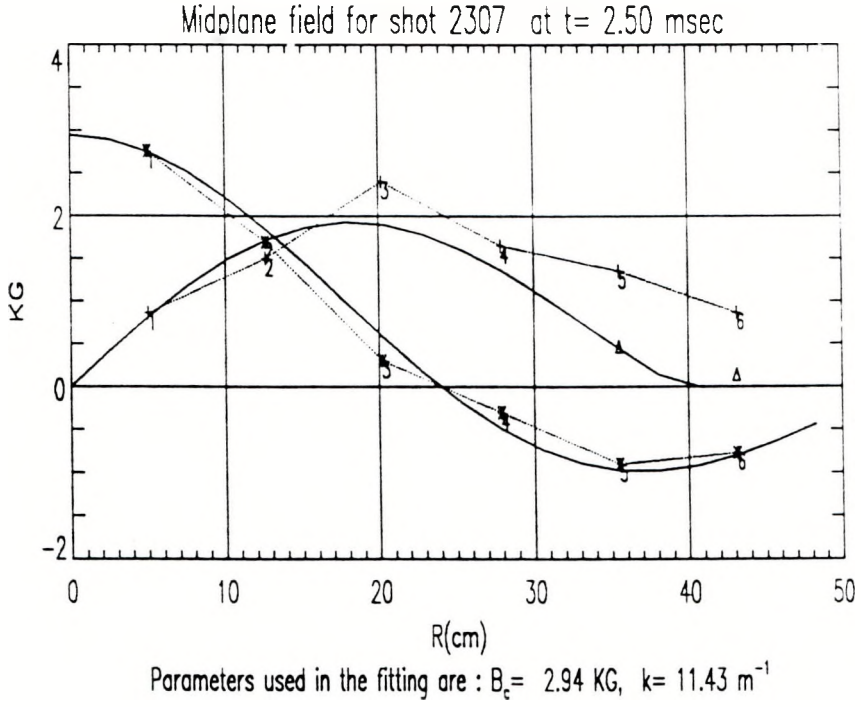

The parameters for the fitted classical spheromak are listed as following:

- the radius of the magnetic axis = 24 cm.
- $k = 2.744/0.24 = 11.43\ \mathrm{m}^{-1}$.
- separatrix radius = $4.4934/k = 0.393$ m.
- coil #1 showed $B_z = 2.75$ kG, then the magnetic field at the center of the plasma $B_c = 2.94$ kG.
- total toroidal current = 162 kA.
- total poloidal current = 201 kA.
- total poloidal flux = 22.2 mWeber.
- total magnetic energy = 1.88 kJ.

Figure 5.2: Comparison of shot 2307 midplane field data with the classical spheromak field. ($*$ B_z field, $+$ B_ϕ field, $\triangle$ is B_ϕ after subtracting the field produced by the I_z current).

As the probe data suggested the onset of a shift or tilt instability, numerous stabilizing conductor configurations were installed in the chamber to improve the plasma performance. Initially, two planar "figure-8" coils[39] were installed at either end of the main vessel near the tips of the I_z electrodes to stabilize the plasma. The "figure-8" coils had proven effective in extending the lifetime of the plasma in the early PS spheromak devices.[40] The position of the "figure-8" coils relative to the machine midplane was varied, and better stabilizing effect was obtained when the "figure-8" was located closer to the midplane.

Figure 5.3 shows the vector plot of the B_ϕ field in the midplane of the vessel with the "figure-8" located at $\pm$22.86 cm off the midplane (SCAN13). At t=0.25 msec, the plasma was already off-center and had larger B_ϕ fields in the lower half of the machine. The center of the plasma shifted up about 10 cm in 100μsec. Without the "figure-8", the plasma shifted much faster and terminated earlier.

A scan of the R-Z plane (SCAN14) was performed under the same plasma conditions. The poloidal field structure of the scan is shown in Fig. 5.4. The positive R is in the direction of 45 degrees from the top to the right when viewing from the west side of the machine, as shown in Fig. 5.3. It clearly indicates that the configuration was initially formed off-center (at r=5 cm), and then drifted even further off center, accompanied with tilting of the plasma at t=0.35 msec.

A cylindrical hard core, 10 cm in diameter, running completely through the machine axis and electrically either connected with or insulated from the vacuum vessel wall, was installed to stabilize the plasma, but showed little effect on the shift. We then tried stabilizing the shift by using aluminum cones, 10 cm diameter at the large end, 3 cm at the small end, and having a 20 degree apex angle, as stabilizer. The cones were located symmetrically on the axis with their ends separated by 20.32 cm (shown in Fig. 5.11). They did increase the plasma life time, but it still seemed to end with a shift.

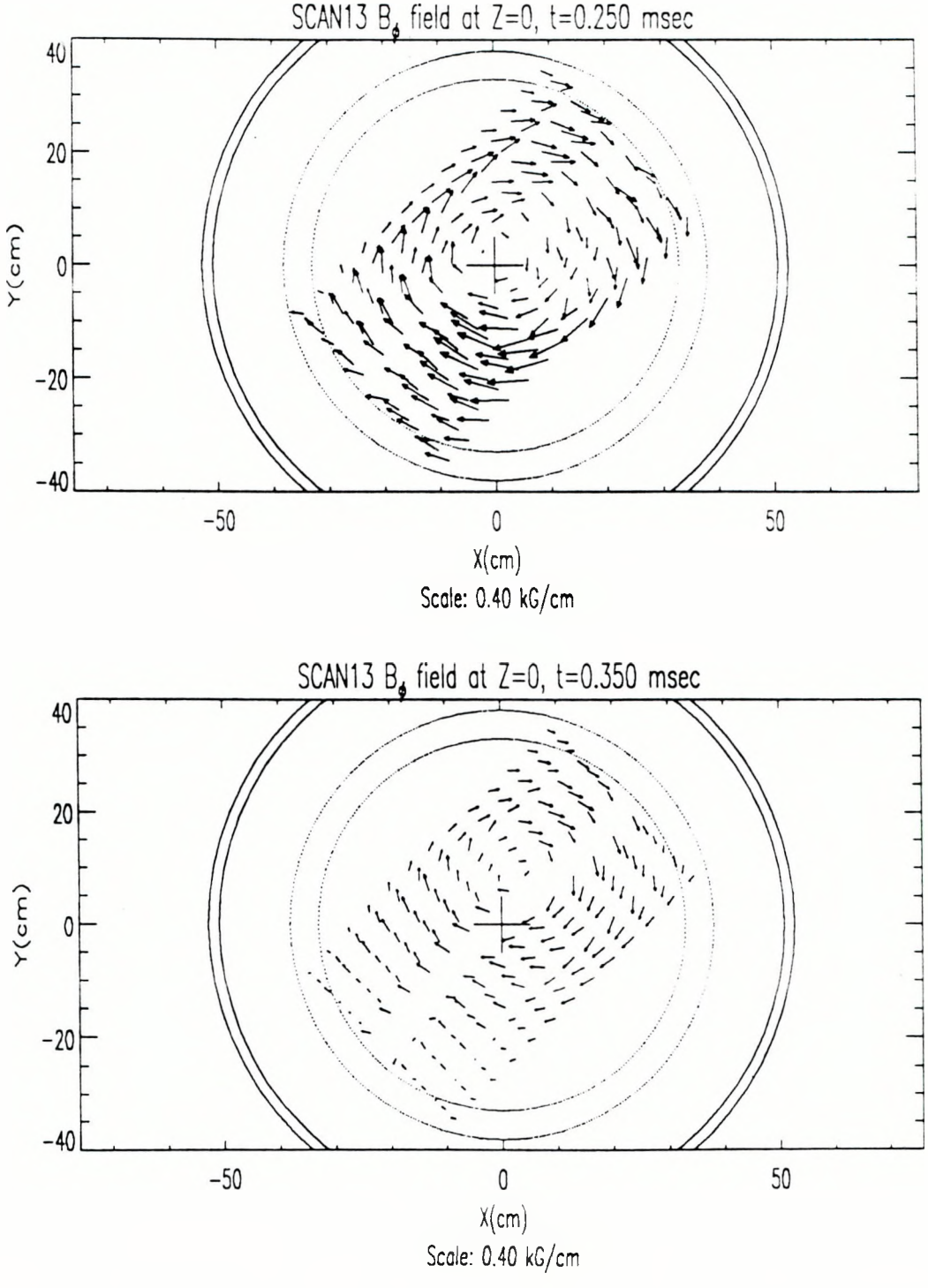

Figure 5.3: Midplane B_ϕ magnetic field structure for SCAN13 at t=(0.25, 0.35) msec, shows that the plasma was off-center. The solid lines represent the chamber wall, the dotted circular lines indicate the radial location of the reversal coils (which are located off the midplane at Z=$\pm$19.05 cm).

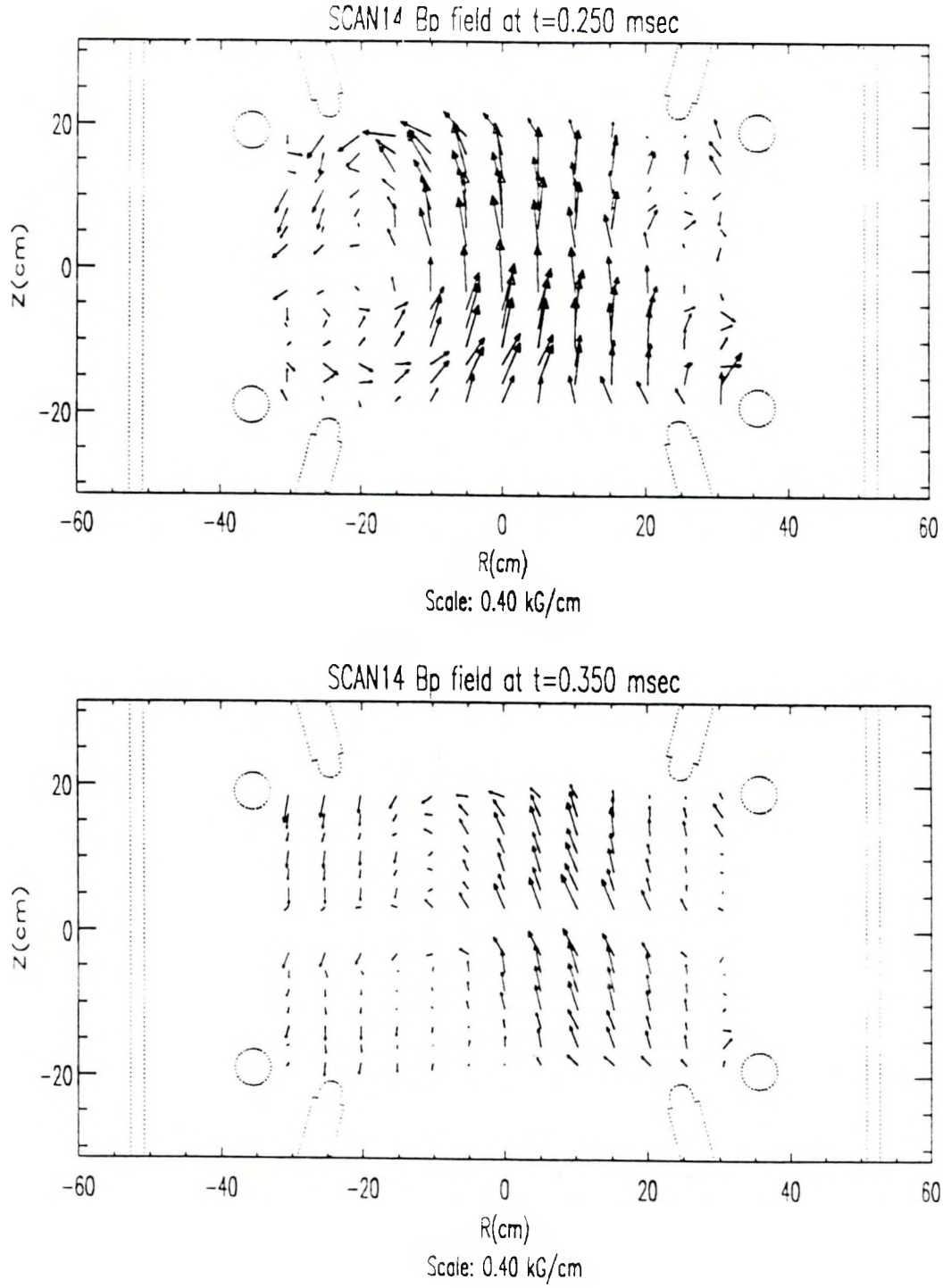

Figure 5.4: R-Z plane poloidal field structure for SCAN14 at t=(0.25, 0.35) msec, shows that the plasma was formed off-center, and then drifted even further off-center, accompanied with tilting of the plasma at t=0.35 msec.

All the stabilizing techniques tried showed some effects of reducing the shift, but failed to eliminate the offset of the configuration. The direction of the shift was quite repeatable (always upward shift [illegible] magnetic field signals were very reproducible from shot to shot.

The puff valves used were located in the upper half of the vessel. As we suspected uneven distribution of the gas puffed into the chamber, these were replaced with two puff valves inserted from the axis on either side of the endplate. This had no effect on the shift, either.

In Figure 5.4, at t=0.250 msec, the poloidal fields near the lower half of the reversal coils reversed, however, the fields near the upper half of the reversal coils did not. This indicated that, near the top of the reversal coils, the poloidal fluxes were linked with the reversal coils, while in the lower part of the coils, the poloidal fluxes were detached and formed closed flux surfaces inside the coils. The reversal circuit usually was crowbarred to prevent current from ringing over as shown in Fig. 3.3. In this case, the reversal circuit was even crowbarred late, to allow some ringing over of the current, to push the linked fluxes away from the reversal coils, but without any success.

In Fig. 5.5, the reversal current waveform for SCAN14 is shown for four different shots when one set of the L-probe coil is located at r=±30.5 cm, z=±18.4 cm. The dotted lines are signals obtained from the probe and normalized to the peak reversal coil current (the peak B_z field measured was 7.1 kG). If there were no plasma current in the vessel, the two signals should be identical. The difference between the two signals is an indication of how much plasma current exists near the reversal coils.

The first and third diagrams of Fig. 5.5 are signals near the lower half of the coils. Both of them show little difference from the probe signal waveform before t=0.25 msec, which indicates that most of the field measured was produced by the reversal coil current. However, the other two diagrams show appreciable differences between the signals. This was a clear indication that there were anomalously high toroidal currents flowing in the vicinity of the reversal coils.

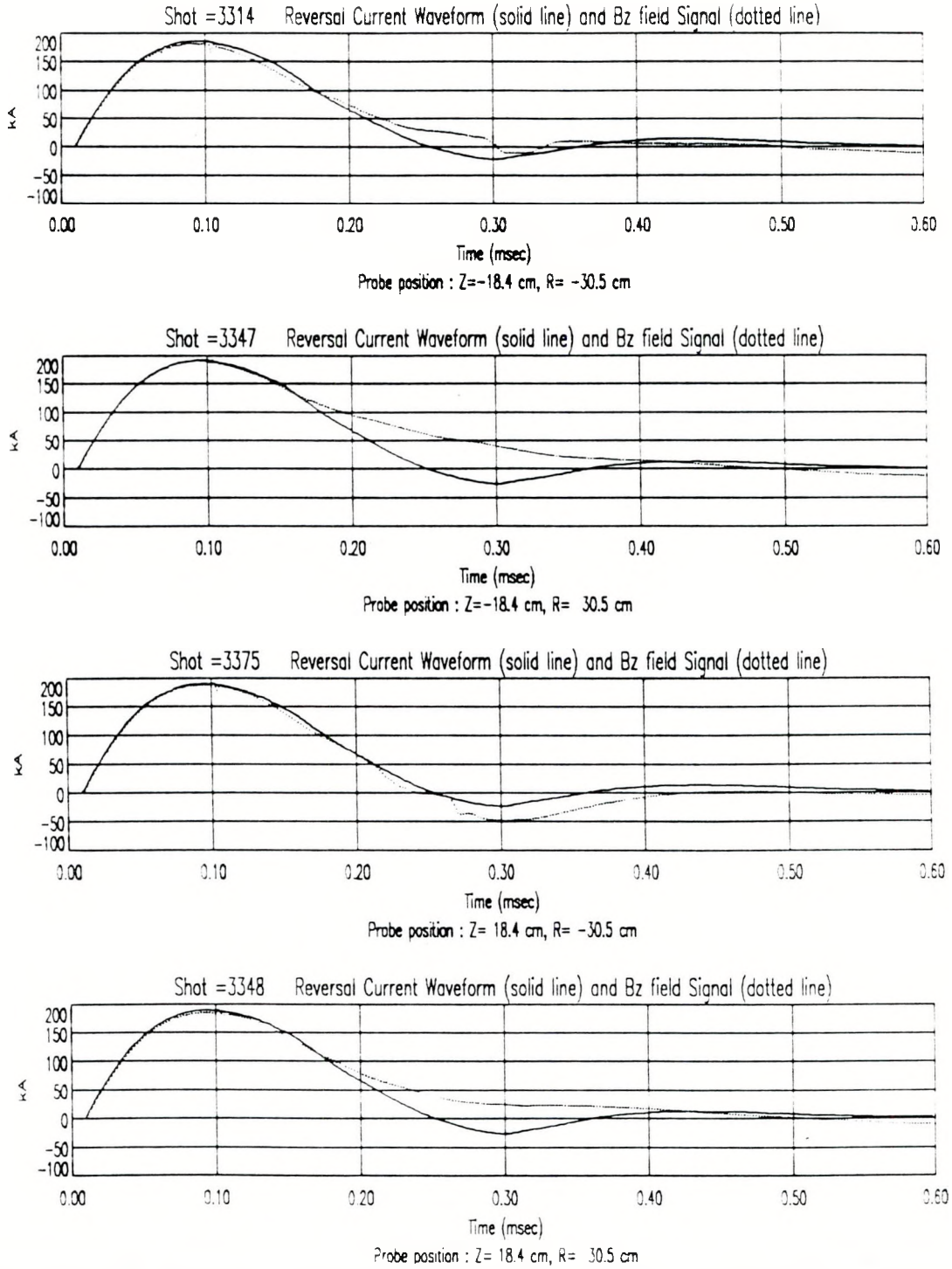

Figure 5.5: Comparison of reversal current waveform with B_z signals near the reversal coils for SCAN14 shots. The B_z signals were normalized to the peak reversal current.

At t=0.25 msec. it indicated ~50 kA of plasma current near the top parts of the coils. As the minor radius of the reversal coil is 2.54 cm. we can estimate the current density around the top part of the coils to be

$$\frac{I_{plasma}}{\pi\,(r^2 - r_{coil}^2)} \sim \frac{50 \times 10^3 A}{\pi(0.0508^2 - 0.0254^2)} = 8.2\ \mathrm{MA/m^2}$$

For the classical spheromak, the peak toroidal current density is about 1.74 MA/m^2, with B_ϕ =2.94 kG. R=39.3 cm as estimated from MS shot 2307 (Fig. 5.2). The current density near the top parts of the reversal coils was much higher than the peak current density of the spheromak. Also, it should be the edge current density which is normally small. This analysis led to the conclusion that the problem was due to current flowing from the plasma to the bare metal of the reversal coils.

Following a suggestion by a visitor from the University of Tokyo, Dr. Yasushi Ono, the reversal coils were completely wrapped with teflon tape to prevent direct contact with the plasma. The currents flowing into the reversal coils were then eliminated, and the probe scan immediately showed that the plasma was forming symmetrically on axis, and remained centered through out its life-time (SCAN20 in Fig. 5.6). A subsequent scan, (SCAN22 in Fig. 5.7), also showed that a symmetric plasma was produced and that the poloidal fields were all reversed inside the reversal coils.

Titanium foil and Nichrome foil were later tried separately to cover the teflon tape in order to prevent sputtering, evaporation or gas desorption in the presence of plasma. The titanium foil became shredded and torn due to magnetic forces after a few hundred shots. It is also a very good material for absorbing oxygen and hydrogen (Titanium is one of the common materials used for gettering). The oxygen being absorbed could recycle, due to the plasma impact, and degrade the plasma performance. The Nichrome withstands the magnetic force much better than the titanium and does not absorb as much oxygen. Teflon tape with the Nichrome covering was used in subsequent work.

Figures 5.8 and 5.9 show the magnetic field measured on the midplane for MS shot 4150 after the shift motion of the plasma was eliminated. The

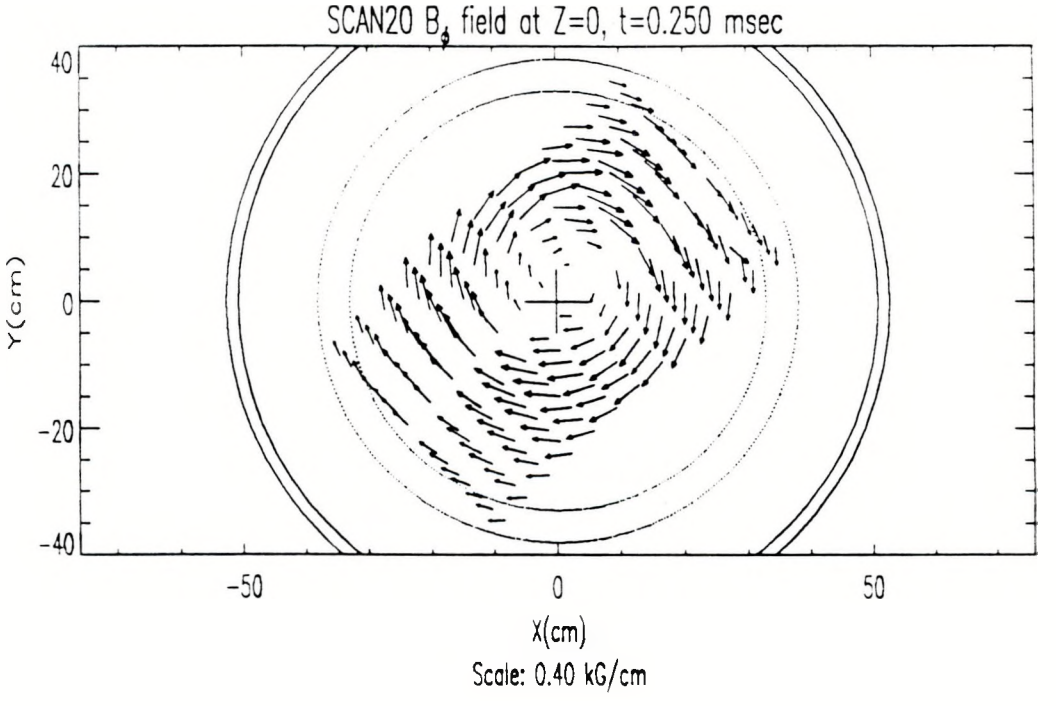

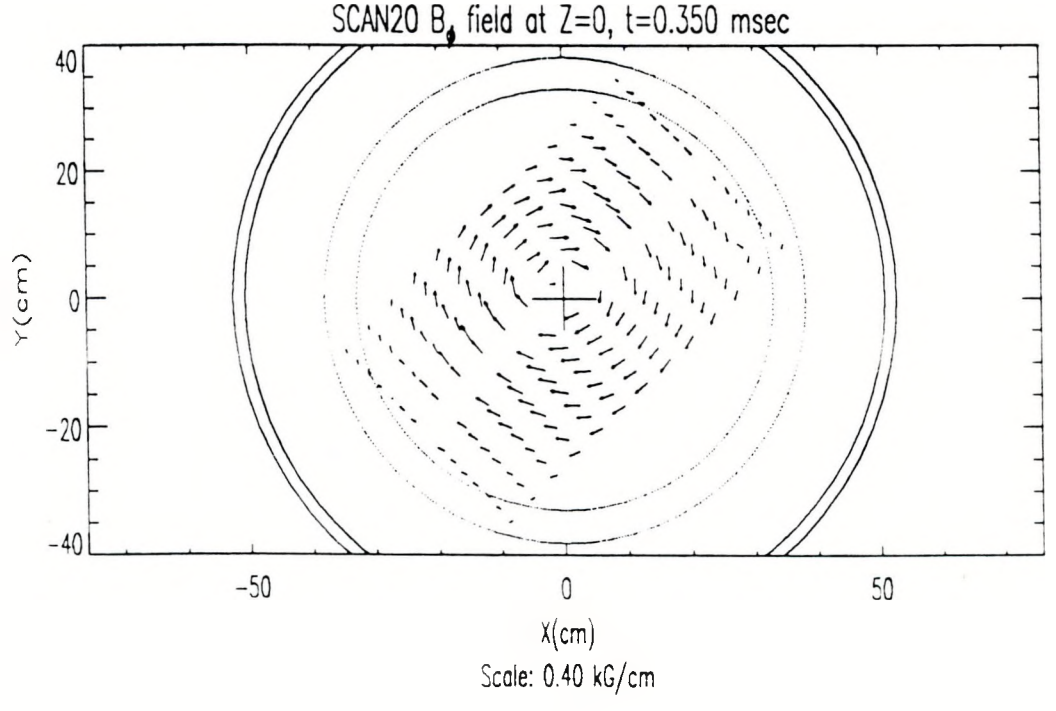

Figure 5.6: Midplane B_ϕ fields for SCAN20 at t=(0.25, 0.35) msec, show that the plasma was forming symmetrically on axis, and remained centered.

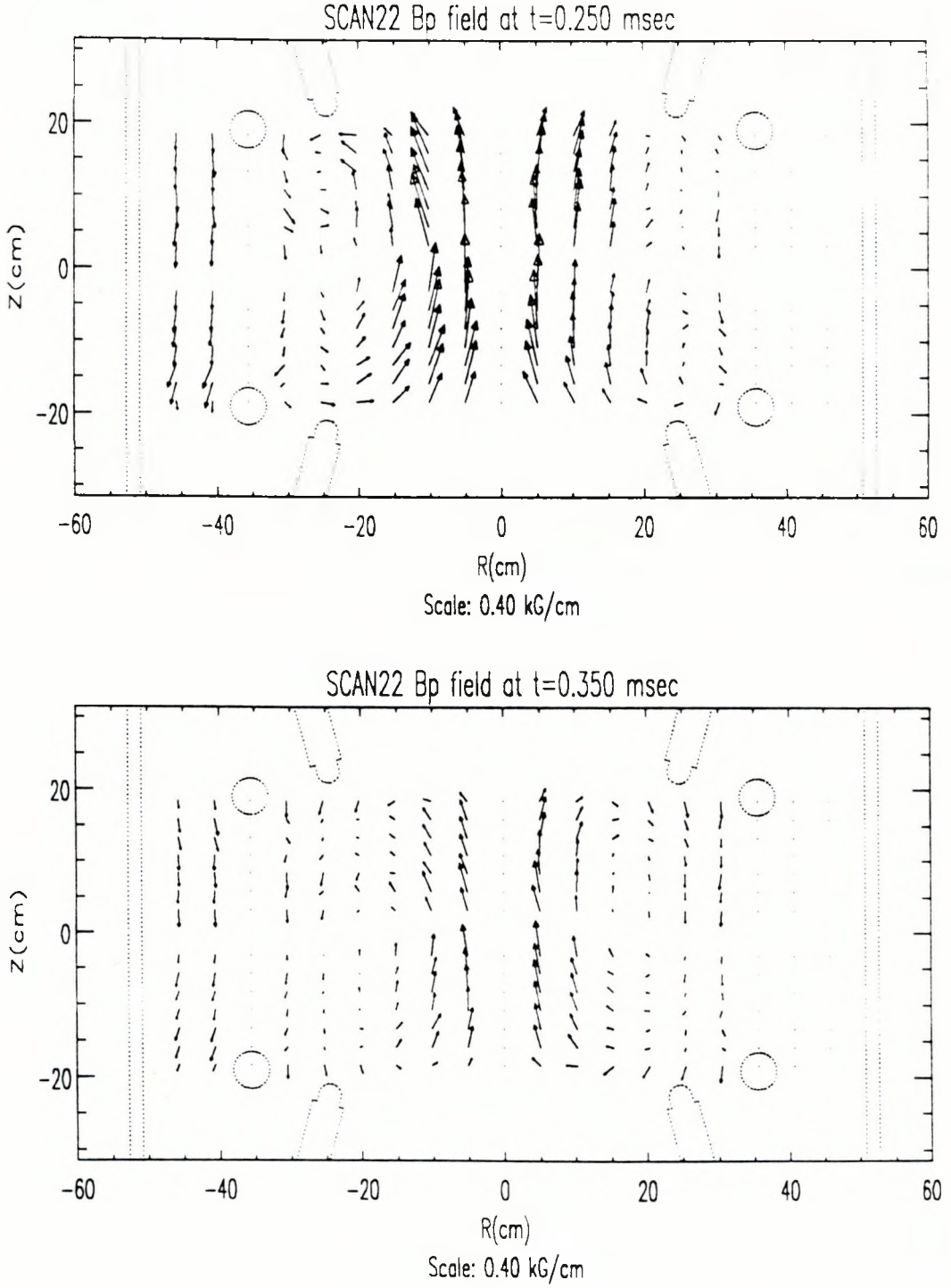

Figure 5.7: R-Z plane poloidal fields show that the plasma was forming centered and the fields were all reversed near the reversal coils for SCAN22 at t=(0.25, 0.35)msec.

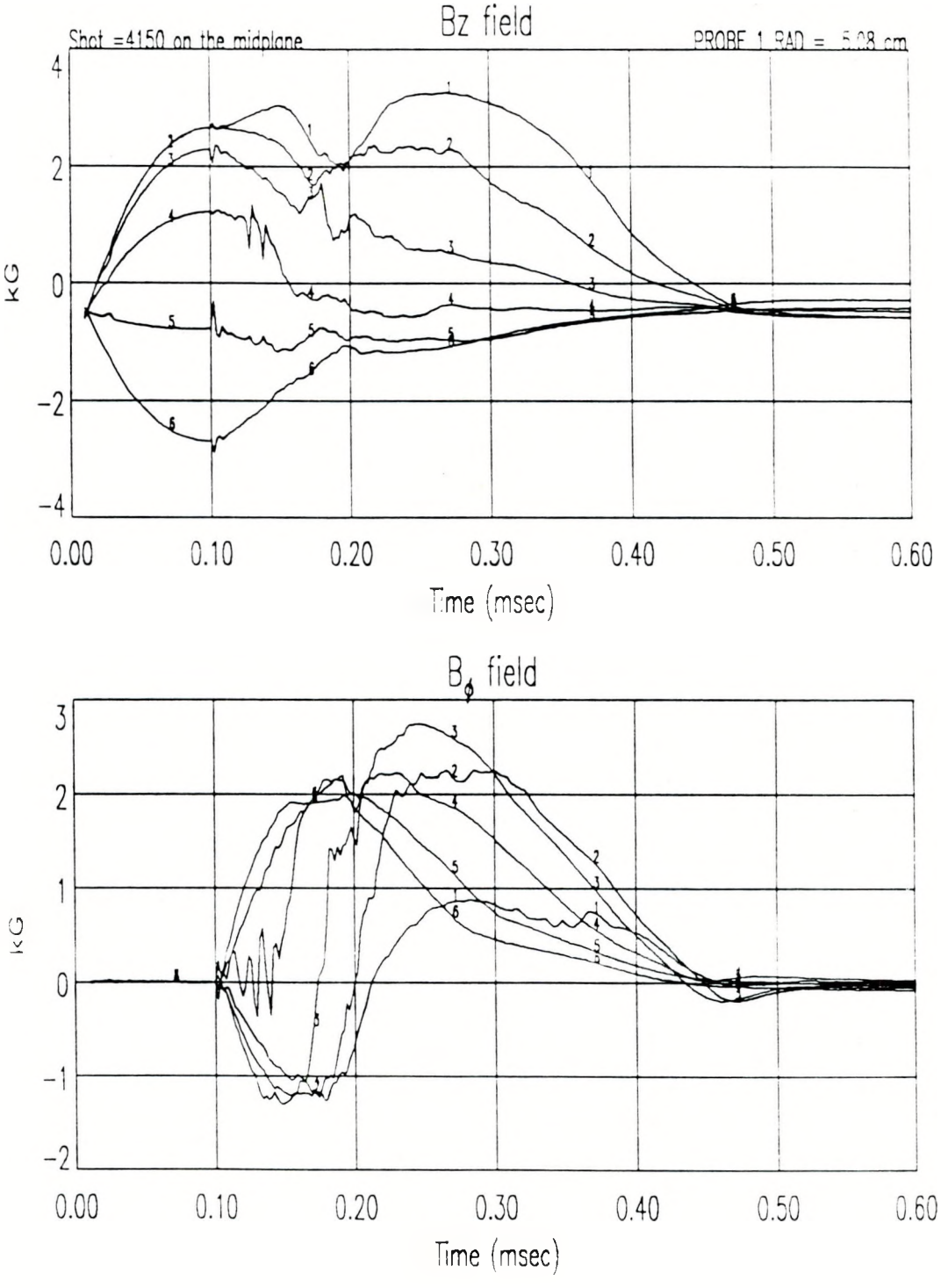

Figure 5.8: Magnetic fields measured with six-position magnetic flux probe on the midplane of the machine. Locations # 1-6 are at r=(5.0, 12.6, 20.2, 27.9, 35.5, 43.1) cm.

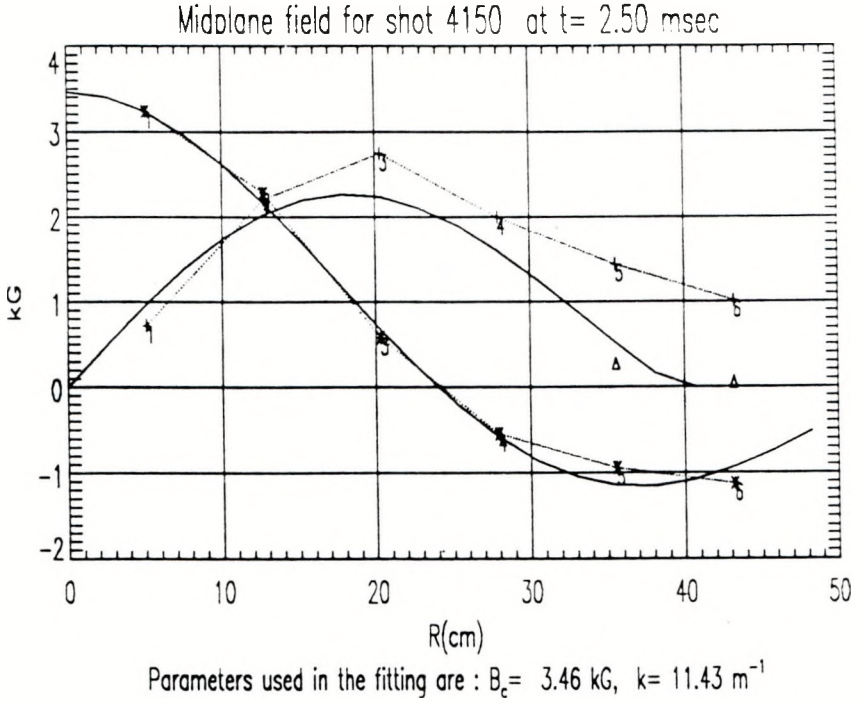

The parameters for the fitted classical spheromak are listed as following:

- the position of the magnetic axis was chosen to be 24 cm.
- $k = 2.744/0.24 = 11.43\ \mathrm{m}^{-1}$.
- separatrix radius $= 4.4934/k = 0.393$ m.
- coil #1 shows $B_z = 3.23$ kG, then the magnetic field at the center of the plasma $B_c = 3.46$ kG.
- total toroidal current = 190 kA.
- total poloidal current = 237 kA.
- total poloidal flux = 26.2 mWeber.
- total magnetic energy = 2.62 kJ.

Figure 5.9: Comparison of shot 4150 midplane field data with the classical spheromak field. ($*$ B_z field, $+$ B_ϕ field, $\triangle$ is B_ϕ after subtracting the field produced by the I_z current.)

magnetic field profile was close to the classical spheromak when the spheromak configuration was formed at t=0.25 msec. After t=0.30 msec, the plasma decays exponentially instead of terminating suddenly. During the decay phase, it remained close to the equilibrium state described by the Grad-Shafranov equation (see Chapter 6).

5.2. Observation of the Reversed Current

It has been observed in MS that the B_ϕ field reversed near the axis of the vessel, mostly before the peak of the I_z (t~0.1-0.2 msec). This was indicated in Fig. 5.8 where the B_ϕ fields of coils #1-3 were reversed. The midplane B_ϕ field structures, for SCAN20 at t=0.15 and 0.25 msec, are shown in Fig. 5.10 At t=0.15 msec, the direction of the B_ϕ fields reversed at radii less than 20 cm. The reversed B_ϕ fields near the axis of the vessel indicated that there were currents flowing in a direction opposite to that of the main I_z discharge. This reversed B_ϕ field usually disappeared about 20~30 μsec after the peak of the I_z .

The poloidal current I_p was calculated for SCAN23 with $\mu_0 I_p = 2\pi r B_\phi$, and is shown in Fig. 5.11. The dotted contours, before t=0.22 msec, indicate currents flowing in a direction opposite to that of the main I_z discharge near the axis of the vessel. At t=0.15 msec, there was more than 113 kA reversed current (the main I_z current was about 350 kA at that same time). The net current inside the radius of 20 cm was about zero at t=0.18 msec.

This same phenomena was observed during the formation phase in S-1 experiments.[41] The reversed B_ϕ field was not seen in the reported two-dimensional simulations of S-1[42] or MS.[25] However, three-dimensional numerical simulations of the relaxation process in spheromak[43] found reversed B_ϕ fields near the axis. It occurred during the relaxation process only for the cases when part of the poloidal flux was converted to toroidal flux. In MS, reversed B_ϕ fields were also seen for the cases when some toroidal flux was converted to poloidal flux (SCAN24 in Fig. 6.12).

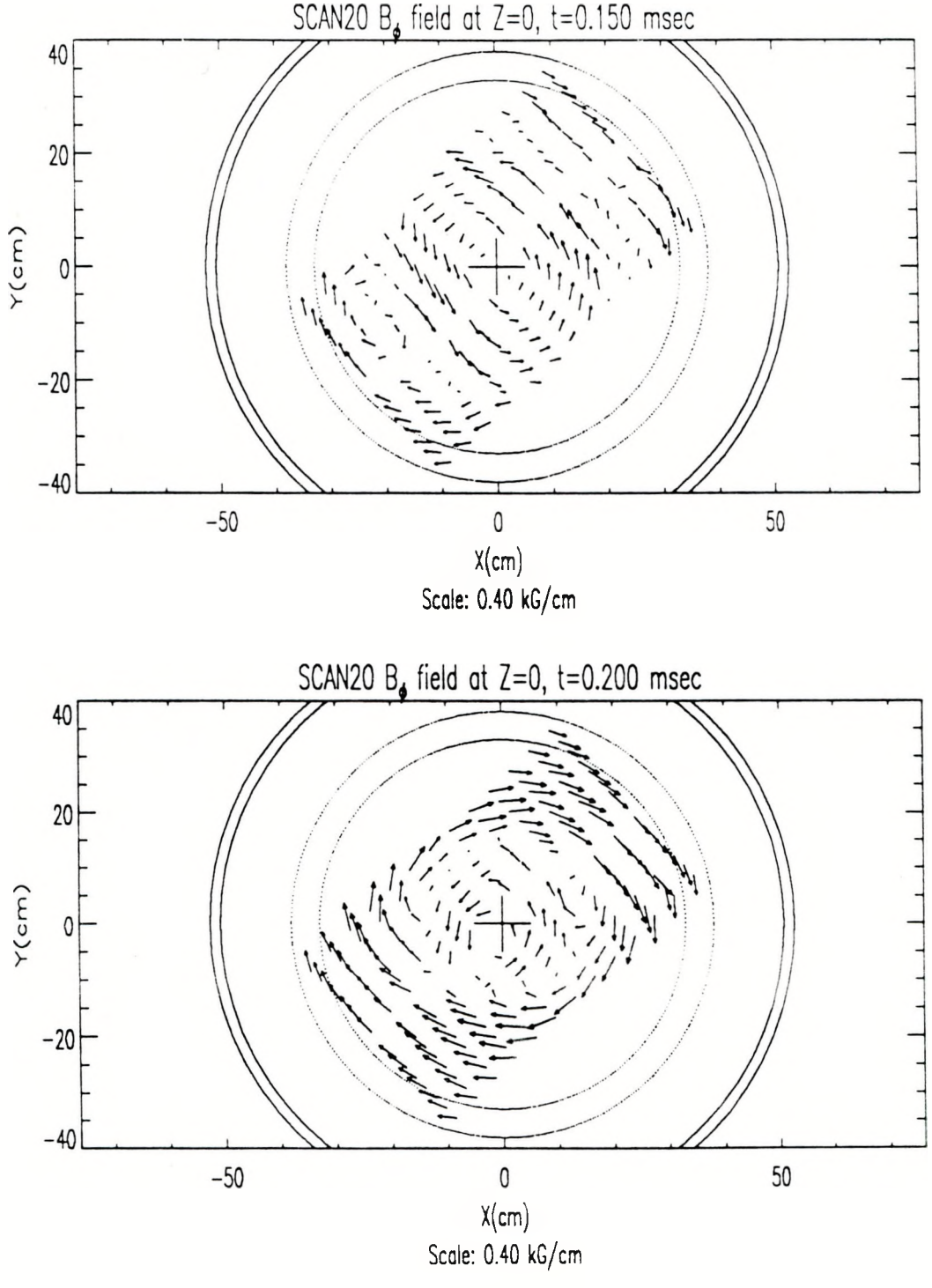

Figure 5.10: Midplane B_ϕ field structure for SCAN20 at t=(0.15, 0.20)msec, shows that B_ϕ fields reversed near the axis of the vessel.

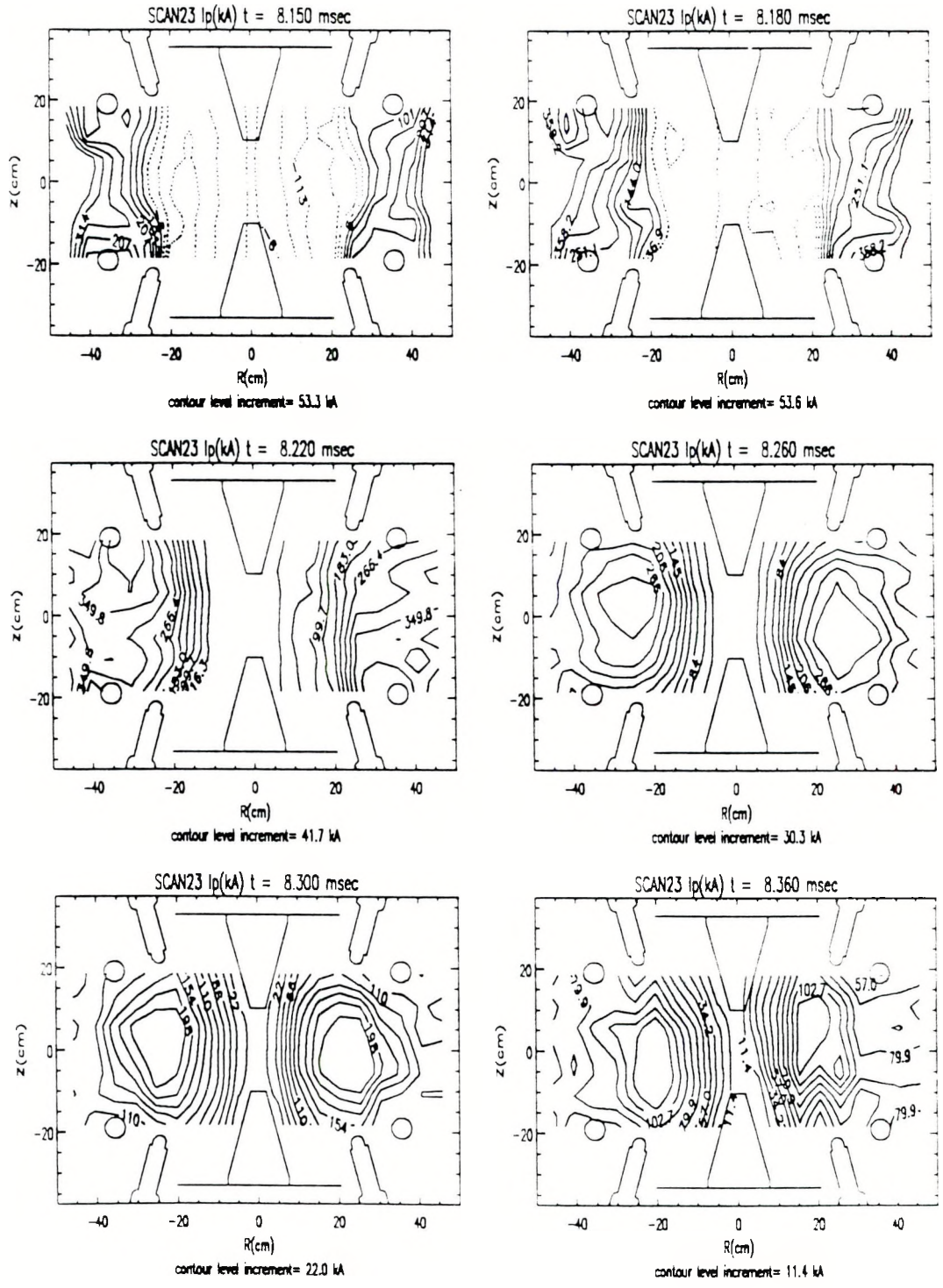

Figure 5.11: R-Z plane poloidal current ($R \cdot B_\phi$) contours of SCAN23. The dotted lines are reversed poloidal current contours. The stabilizing cones located in the axis are also shown.

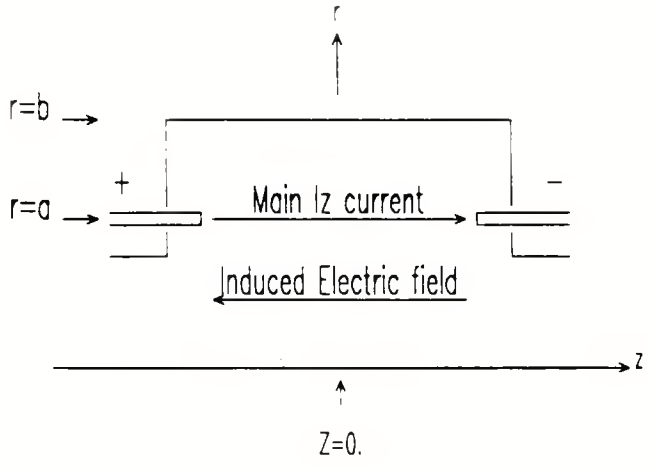

Figure 5.12: Model for explaining the reversed I_z current.

This reversed B_ϕ field may be related to the counter-rotating plasma cells observed in PS-3.5 experiments during spheromak formation.[44] The gradient in velocity causes conversion of poloidal into toroidal field, resulting in the observed reversed B_ϕ field.

The reversed current may also be explained by the axisymmetric model indicated in Fig. 5.12. Assuming that there is a constant strong magnetic field in the $\hat{z}$ direction, so the I_z current flows on a surface of constant radius a, and $\partial/\partial z = 0$. The B_ϕ field is

$$B_\phi(r) = \begin{cases} \dfrac{\mu_0 I}{2\pi r}, & b \geq r \geq a; \\ 0. & r < a. \end{cases}$$

We can chose a gauge such that $\vec{A} = 0$ on the metal wall boundary. For an axisymmetric configuration, A_z can be calculated as

$$A_z(r) = \begin{cases} \dfrac{\mu_0 I}{2\pi} \ln\left(\dfrac{b}{r}\right) & b \geq r \geq a\ ; \\ \dfrac{\mu_0 I}{2\pi} \ln\left(\dfrac{b}{a}\right) & r < a. \end{cases}$$

The electric field, $\vec{E} = -\nabla\Phi - \partial\vec{A}/\partial t$, is electrostatic if the current I is a constant. When I varies with time, as in the MS discharge, there is a contribution due to the time variation of the current to the electric field,

$$E_z(r,t) = -\nabla\Phi \cdot \hat{z} - \begin{cases} \dfrac{\mu_0 \dot{I}}{2\pi} \ln\left(\dfrac{b}{r}\right) & b \geq r \geq a; \\ \dfrac{\mu_0 \dot{I}}{2\pi} \ln\left(\dfrac{b}{a}\right) & r < a. \end{cases}$$

where $\dot{I} = \partial I/\partial t$. If this electric field were large enough, it could cause the breakdown of the plasma and form the reversed current near the axis which flowed from one side of the vessel to the other side, as seen in MS.

We can look at the situation from another point of view, the voltage was induced to prevent changing of the toroidal fluxes inside the vacuum vessel when the I_z was discharged.

$$\begin{aligned} L_{vessel} &= \frac{\mu_0}{2\pi} \ell \ln\left(\frac{b}{a}\right) \\ V &= -L_{vessel}\dot{I} \\ &= -\frac{\mu_0 \dot{I}}{2\pi} \ell \ln\left(\frac{b}{a}\right) \end{aligned}$$

where L_{vessel} is the inductance of the vacuum vessel, ℓ is the length of the main cylinder. This is a consequence of **Lenz's law**.

5.3. Effect of the I_z Discharge Paths

Another feature which can be seen from Fig. 5.11 is that in the early phase of the I_z discharge, the poloidal current closely followed the vacuum poloidal field lines. The vacuum flux surfaces produced by the reversal coil and bias coil currents, at the time I_z was triggered, are shown in Fig. 5.13. The flux surfaces near the tip of the electrodes were closed flux surfaces inside the chamber. There were two different paths that link the anode and the cathode electrodes. One was the path inside the inner radius of the the reversal coils and the other one went between the outer radius of the reversal coils and the vacuum chamber wall. If the I_z current did follow the field lines when break down occurred, the I_z current could have flowed both ways.

Another magnetic probe with 6 coils was built to measure the toroidal field near the I_z electrode and study the I_z discharge current paths. The probe was installed radially from one of the diagnostic ports located at Z=25.4 cm. The coils were 3.81 cm apart, and positioned at R=31.75-50.8 cm (also shown in Fig. 3.1 as B_ϕ probe). The total poloidal current distribution flowing inside the vessel was calculated from the field measurement.

The data for MS shot 5187 is shown in Fig. 5.14(a). The signal shows that, for the first 10 μsec of the I_z discharge, there was almost no net current flowing inside the radius of coil #3. It also indicates that all the current flowed through the region between coil #3 and coil #4. The results indicated that those currents flowed between the reversal coils and the vacuum chamber wall and that they were mostly confined to the flux surfaces which link the anode and the cathode I_z electrodes.

The I_z cables and the metal chamber walls formed a coaxial system. When the I_z was discharged, the same amount of current flowed on the inner surface of the vessel wall as a return path. In such case, the path outside the outer radius of the reversal coils was the lowest inductance path, so the I_z broke down there first. Once the I_z discharge occurred, the plasma was initiated. The current started to flow through the path inside the inner radius of the

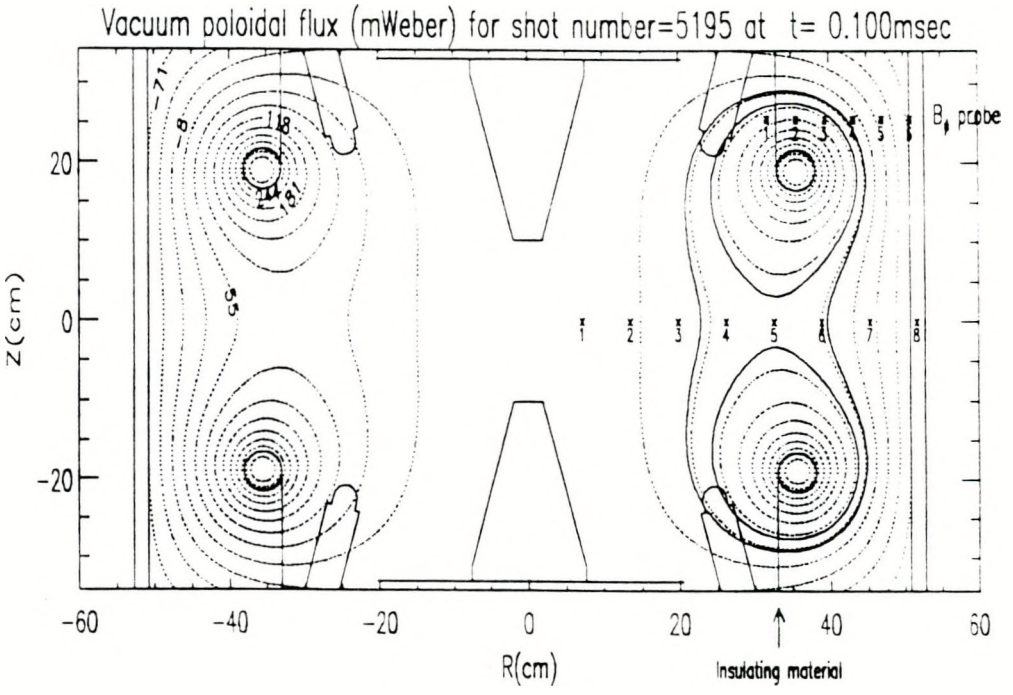

Figure 5.13: Vacuum poloidal fluxes for MS shot 5195 at t=0.1 msec. The dotted lines show the vacuum poloidal flux surfaces produced by the bias coil current and the reversal coil current. The solid flux lines indicate flux surfaces linking the anode and the cathode electrodes. Note that those flux lines were located between coils #3 and #4 of the B_ϕ probe. ($*$ near the top right corner represent the B_ϕ probe and coils are numbered 1-6, $\times$ indicates coil locations of the midplane probe.) The solid lines between the endplate and the reversal coils represent insulating material temporarily used to block the current paths.

reversal coils in 10 μsec. When the total current inside coil #3 reached $\simeq$ 200 kA, it remained about the same for almost 30 μsec. This was due to the fact that the reversed axial current was also forming and had the largest driven voltage at the same time. The current inside coil #3 increased by an appreciable amount after t=0.15 msec. At that moment, the derivative of the I_z became smaller and then started to reverse sign after the peak of the I_z current (t=0.18 msec).

The spheromak configuration is formed mostly from current flowing through the central region of the vessel. The current flowing between the reversal coils

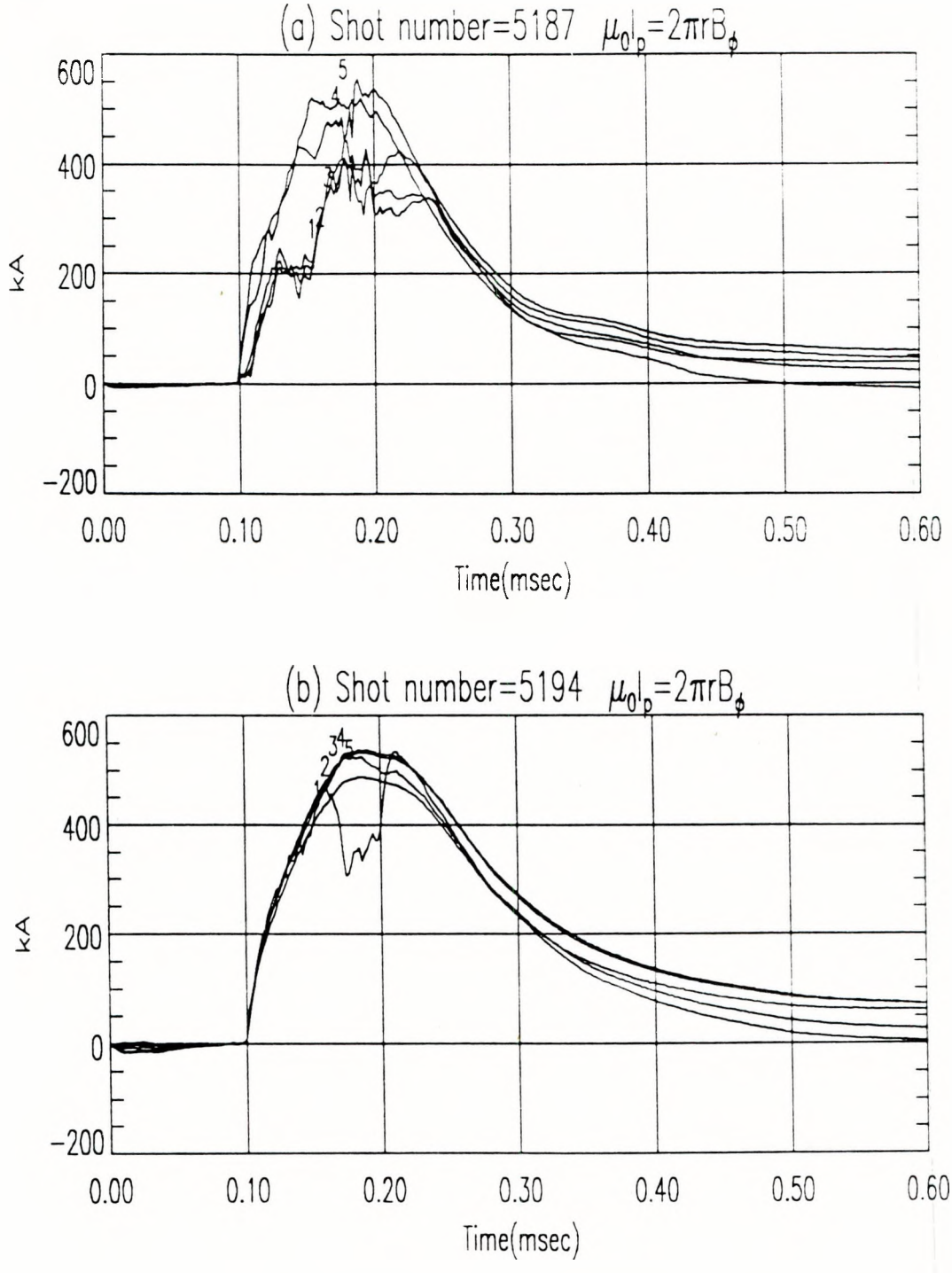

Figure 5.14: I_p signals near the I_z electrodes before/after installation of polyethylene sheets to stop the I_z current from flowing between the reversal coils and the vacuum chamber wall. Locations #1-5 are at r=(31.75, 34.93, 38.10, 41.28, 44.45, 47.63) cm. (a) Before the current paths were blocked. (b) After the current paths were blocked.

and the chamber wall diverted a large fraction of the energy and could also bring in impurities when the flux surfaces crossed the reversal coils.

As a first attempt to modify this pattern of current flow, two 15 cm wide sheets made of polyethylene material were installed inside the chamber (shown in Fig. 5.13) to intercept the current path between the reversal coils and the chamber wall. Figure 5.14(b) shows that all the current then flowed inside the coil #1 throughout the whole I_z discharge and that the waveforms were closer to the I_z current waveform. A small deviation of the coil #1 signal, near the peak of the I_z current, was due to a small hole in the polyethylene sheet that let the current pass through, and coil #1 was the only coil located inside the radius of the polyethylene sheet.

Figure 5.15 shows the poloidal current distribution on the midplane before/after the current path between the reversal coils and the chamber wall was intercepted (MS shot 5187/5194). Figure 5.13 showed that coil #3 of the midplane probe was located inside the flux surface linking the I_z electrodes at t=0.1 ms. The negative I_p currents of coils #1-3 for both cases are another evidence of the reversed current. For shot 5187, before t= 0.15 msec, most of the current was flowing between coils #4-7 and the net current inside coil #4 was almost zero. For shot 5194, before the peak of the I_z current, all the current flowed inside coil #5. The dotted lines in Fig. 5.15 are the reversal coil current and I_z current waveforms. This was consistent with the measurements shown in Fig. 5.14 which indicated that all the current was flowing inside the inner radius of the reversal coils after the other path was blocked. Figure 5.16 showed that the B_z magnetic fields at the midplane of the vessel, after the spheromak was formed (at t$\simeq$0.25 msec), were more than doubled when the current path between the reversal coils and the chamber wall was blocked.

Two annular glass plates later replaced the polyethylene sheets. These have outer radius 100 cm, inner radius 76 cm and are installed at Z=$\pm$22.86 cm, to block the current from flowing between the reversal coils and the vacuum chamber wall.

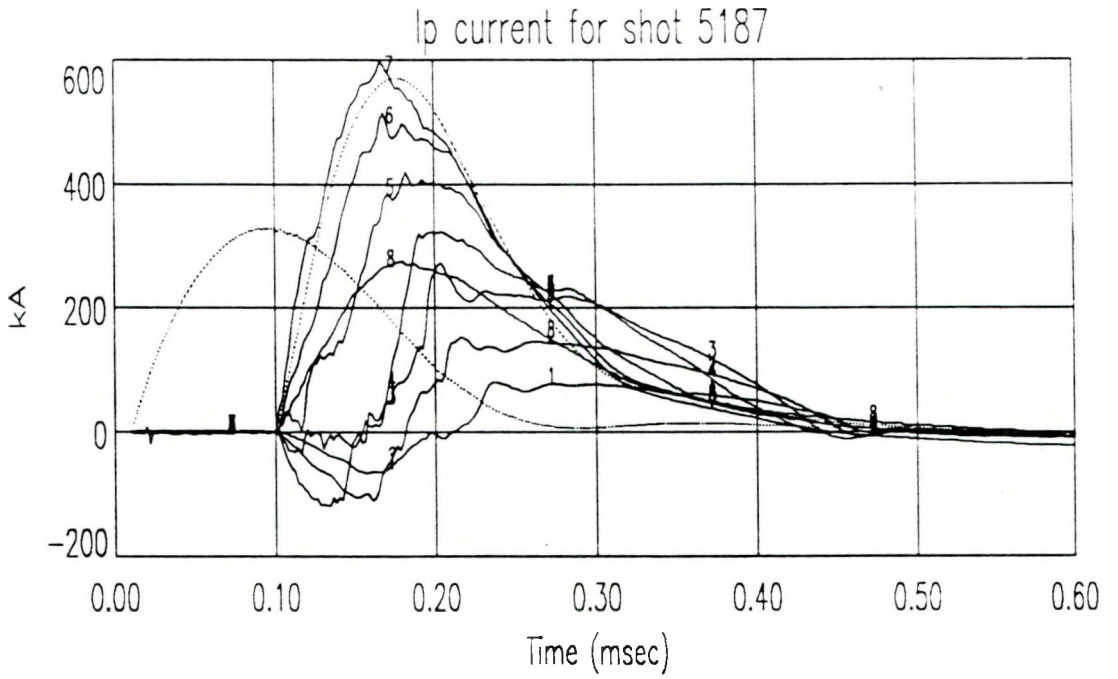

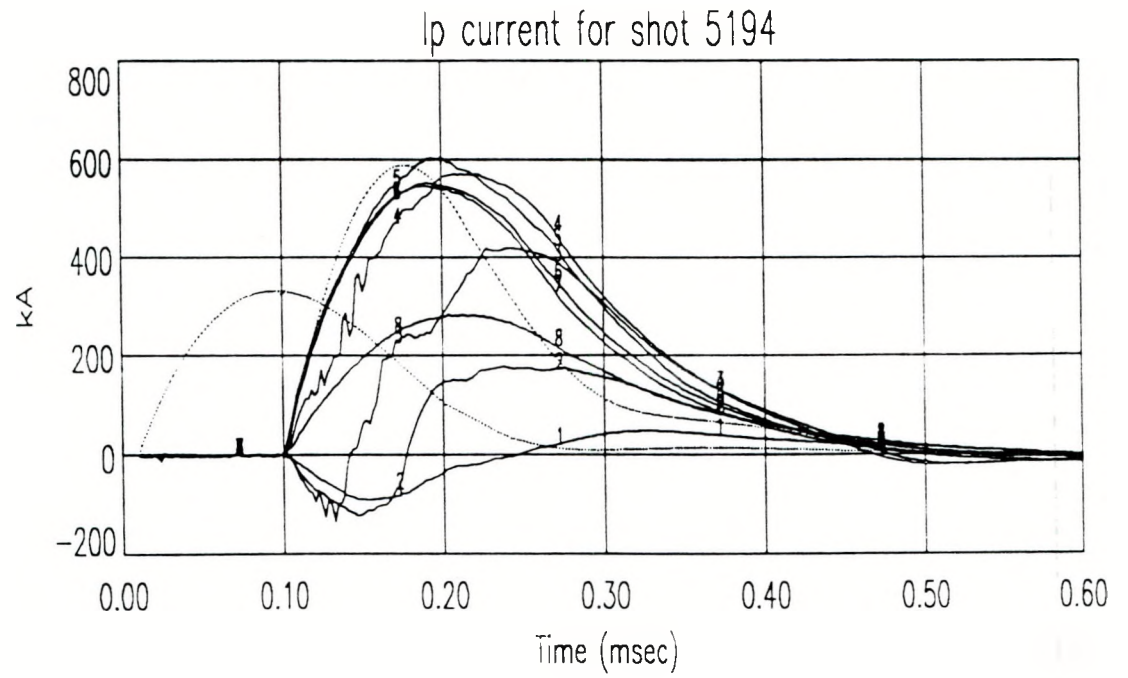

Figure 5.15: I_p at the midplane shows the effect of I_z discharge current path. (a)/(b) before/after the current path between the reversal coils and the chamber wall was intercepted. Locations # 1-8 are at r=(7.18, 13.53, 19.88, 26.23, 32.58, 38.93, 45.28, 51.63) cm.

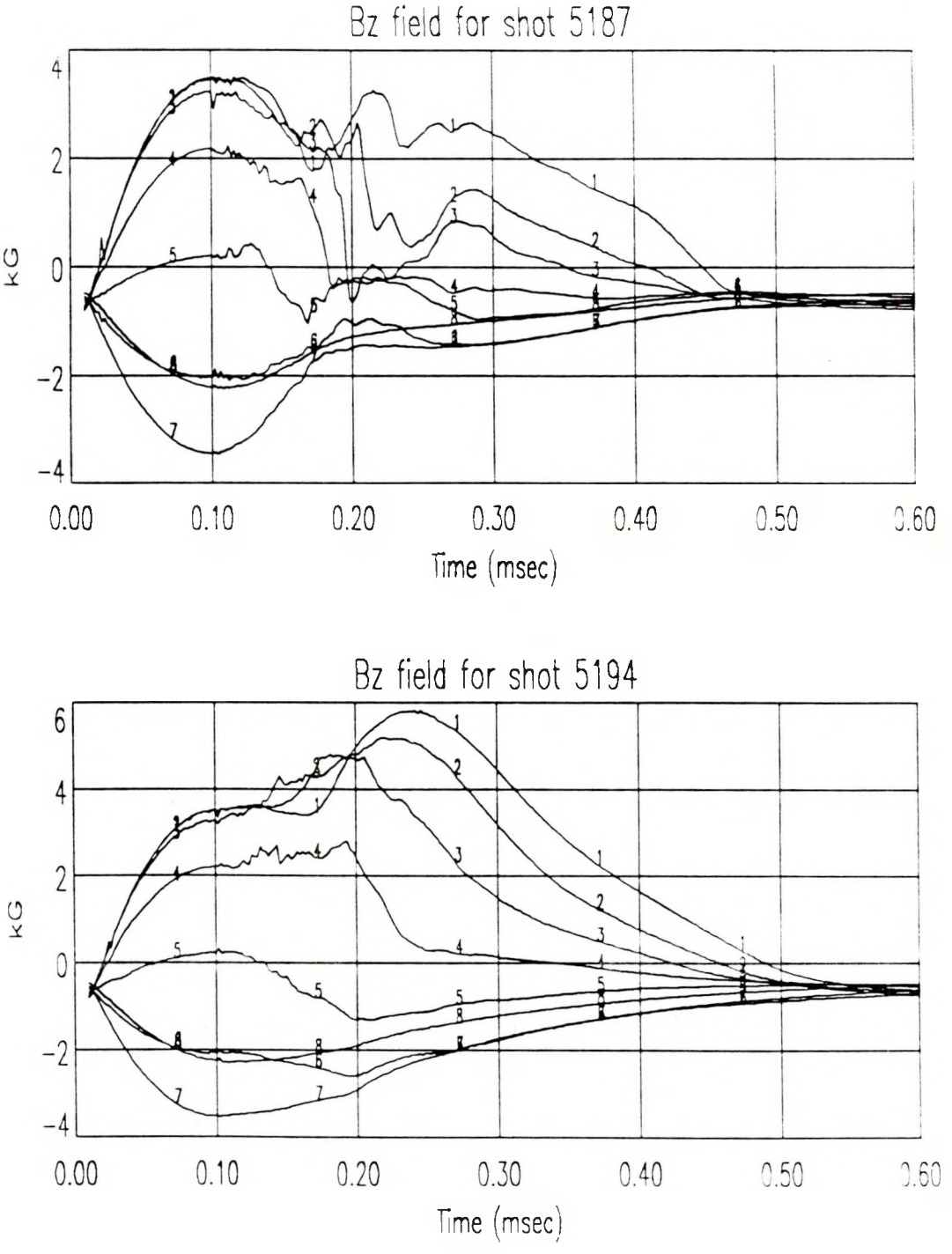

Figure 5.16: B_z field at the midplane shows the effect of I_z discharge current path. (a)/(b) before/after the current path between the reversal coils and the chamber wall was intercepted. Locations # 1-8 are at r=(7.18, 13.53, 19.88, 26.23, 32.58, 38.93, 45.28, 51.63) cm.

Chapter 6.
Magnetic Properties of the MS Spheromak

The magnetic properties of the MS spheromak are discussed based on the magnetic probe measurements. It was observed that during the formation phase, the magnetic profile evolves in such a way that the ratio of the poloidal current to poloidal flux in the plasma approaches a constant value. This constant is related to the size of the spheromak produced. The plasma is close to Taylor's minimum energy state when the spheromak configuration formed. The magnetic field then decays exponentially, and the magnetic field profile remains close to the equilibrium state during the decay phase (more discussion in Chapter 7).

Most of the measurements presented in this chapter are data taken from two R-Z plane magnetic field scans, SCAN23 and SCAN24. The major difference between SCAN23 and SCAN24 is that the I_z current path between the reversal coils and the vacuum vessel wall was blocked by two annular glass plates (described in Chapter 5) for SCAN24 plasma shots. Typical I_z current and reversal current wave-forms for the two scans are shown in Fig. 6.1. The current wave-forms and their timing are similar in both cases, except that there was more reversal current in the SCAN23 case, while for SCAN24 more I_z current was discharged. The bias coil currents used were 302 ± 3 A for SCAN23 and 458 ± 7 A for SCAN24.

Two aluminum cones were used to stabilize the plasma for SCAN23 MS shots. For SCAN24 conditions, two sets of "figure-8" coils with cone-shape configuration replaced the aluminum cones. The poloidal field structures are shown in Figs. 6.2 and 6.3 for the two scans. The "stabilizers" used are also shown in the two figures. Spheromak configurations were formed symmetrically in both cases. The magnitudes of the magnetic fields are almost twice as large in SCAN24 compared with the magnitude of the fields in SCAN23. In the figure, for SCAN23, the arrow with 1 cm length (scale of the plot)

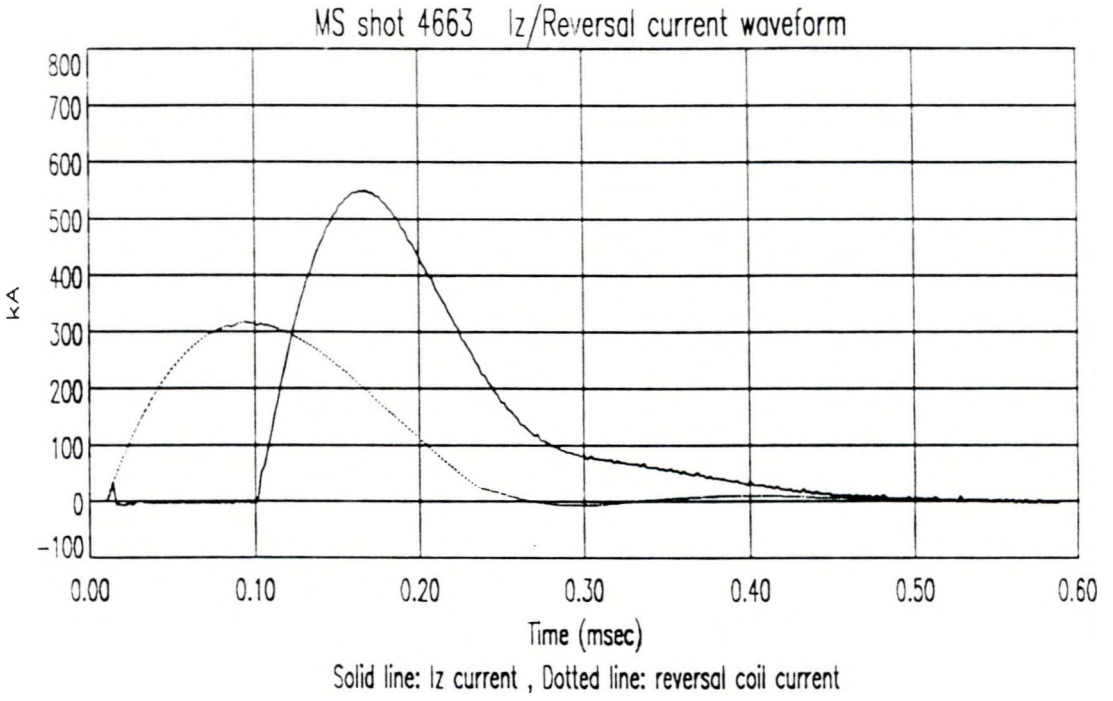

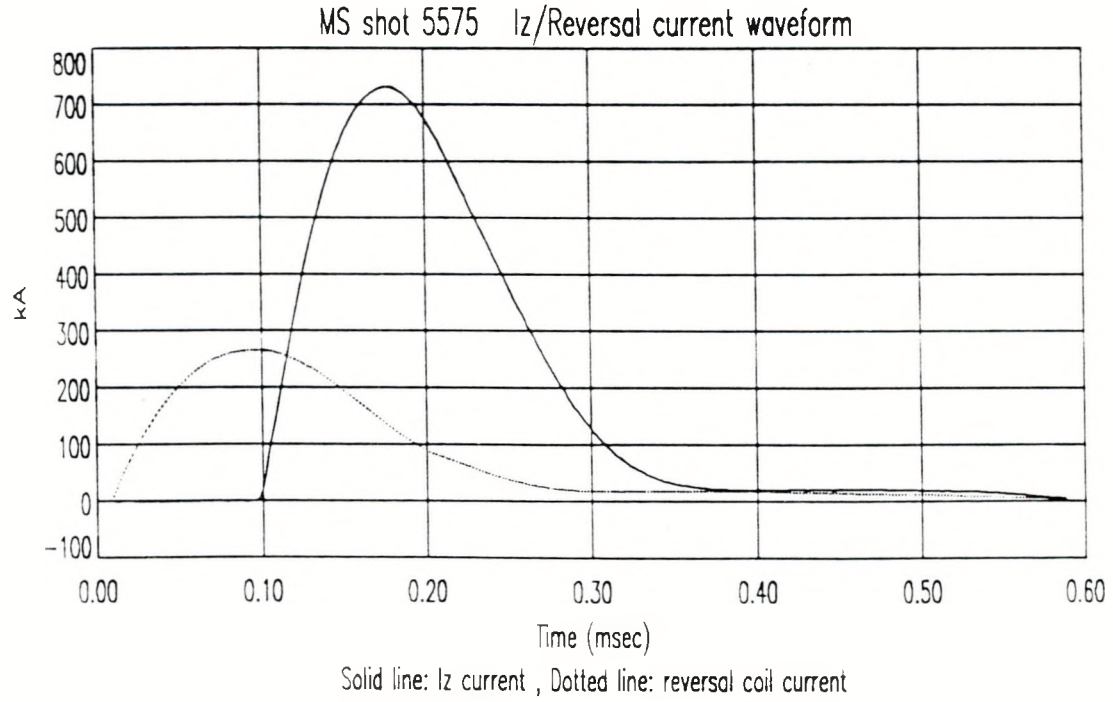

Figure 6.1: Typical I_z current and reversal current wave-forms for SCAN23 (MS shot 4663) and SCAN24 (MS shot 5575)

represents 0.5 kG field, and it represents 0.8 kG field for SCAN24. For the SCAN23 case, a tilt motion developed when the plasma started to decay at t=0.30 msec. There was no tilt motion of the plasma for SCAN24 shots. The cone-shape "figure-8" coils stabilized the plasma more effectively than the aluminum cones.

6.1. Formation Phase

The poloidal and toroidal fields on the midplane for MS shot 5187 are shown in Fig. 6.4. The signal is plotted with 1 kG DC offset between successive pairs of coils. The B_ϕ signals of coil #1–3 have a sudden increase in magnitude during the period between t=0.17–0.22 msec. The change of the B_ϕ signals is related to the change of the I_z current profile. Figure 5.11 shows that, at t=0.15 msec, most of the I_z current on the midplane was flowing in an annulus outside a radius of 26 cm, and at the same time was drifting radially toward the axis. When the current sheet drifts across a coil position, there is a sudden change of the net current inside the radius of that coil position. The B_ϕ signal is a measure of the total poloidal current inside the coil radius. It changes dramatically in response to the sudden increase of the net current.

Figure 6.4 also shows that correlations exist between the B_z signal and the B_ϕ signal for coils #1-4. The fluctuations of the B_z and B_ϕ signals occurring at the same locations are always out of phase between t=0.17-0.24 msec (formation time). The local minimum of the poloidal signals roughly corresponds to the local maximum of the toroidal signals. At t$\simeq$0.17 msec, B_ϕ signal #4 starts to increase by more than 2 kG in $\simeq$18 μsec, while during the same period B_z signal #4 drops by 1.5 kG. Then B_ϕ signal #3 starts to jump to a higher level and the B_ϕ signal at the same location drops to a lower value. The process continues to occur in coils #2 and #1. Coil #5 also shows a similar relation between the B_z and B_ϕ signals but with smaller fluctuations.

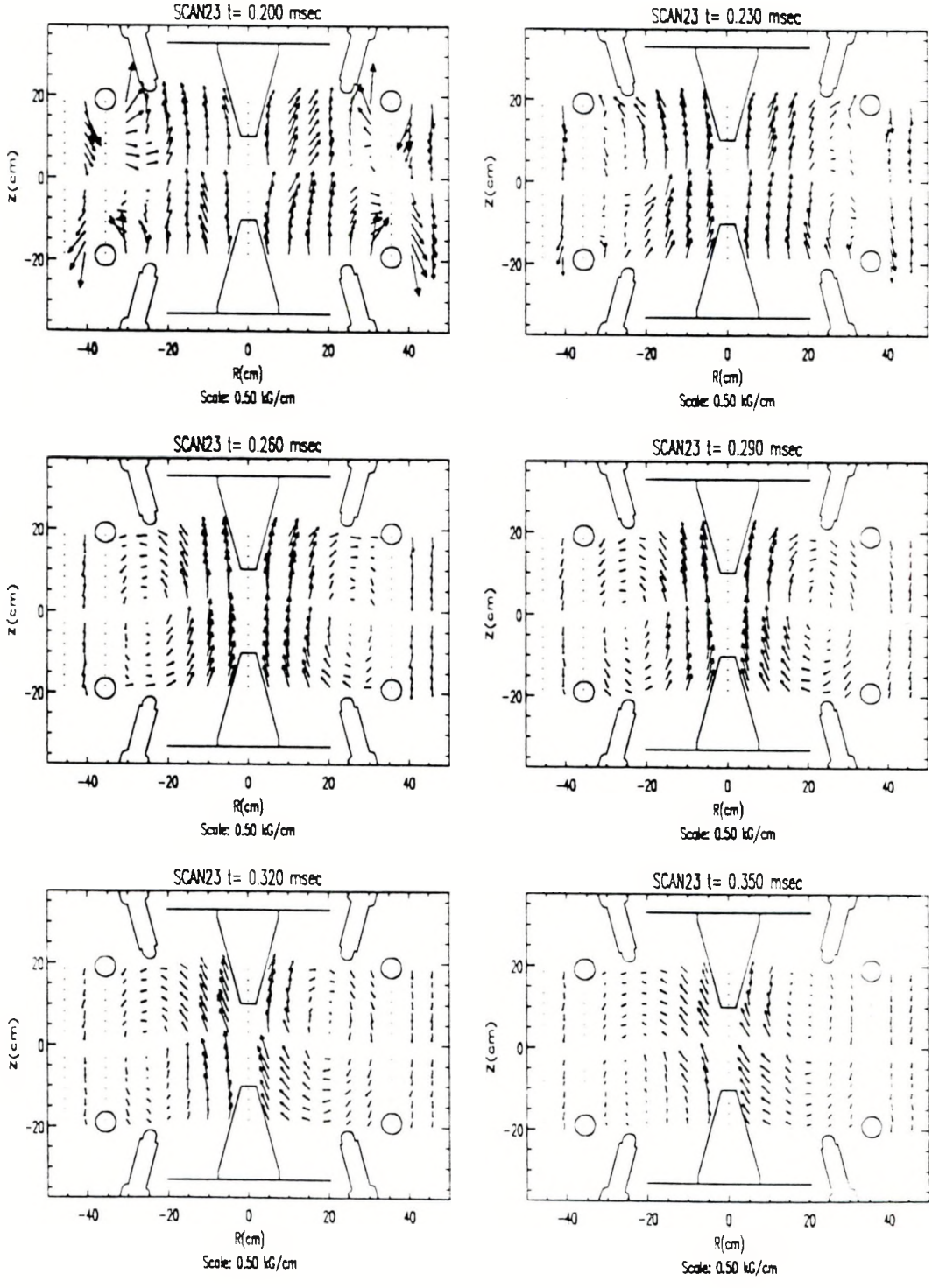

Figure 6.2: Poloidal field structure on the R-Z plane for SCAN23.

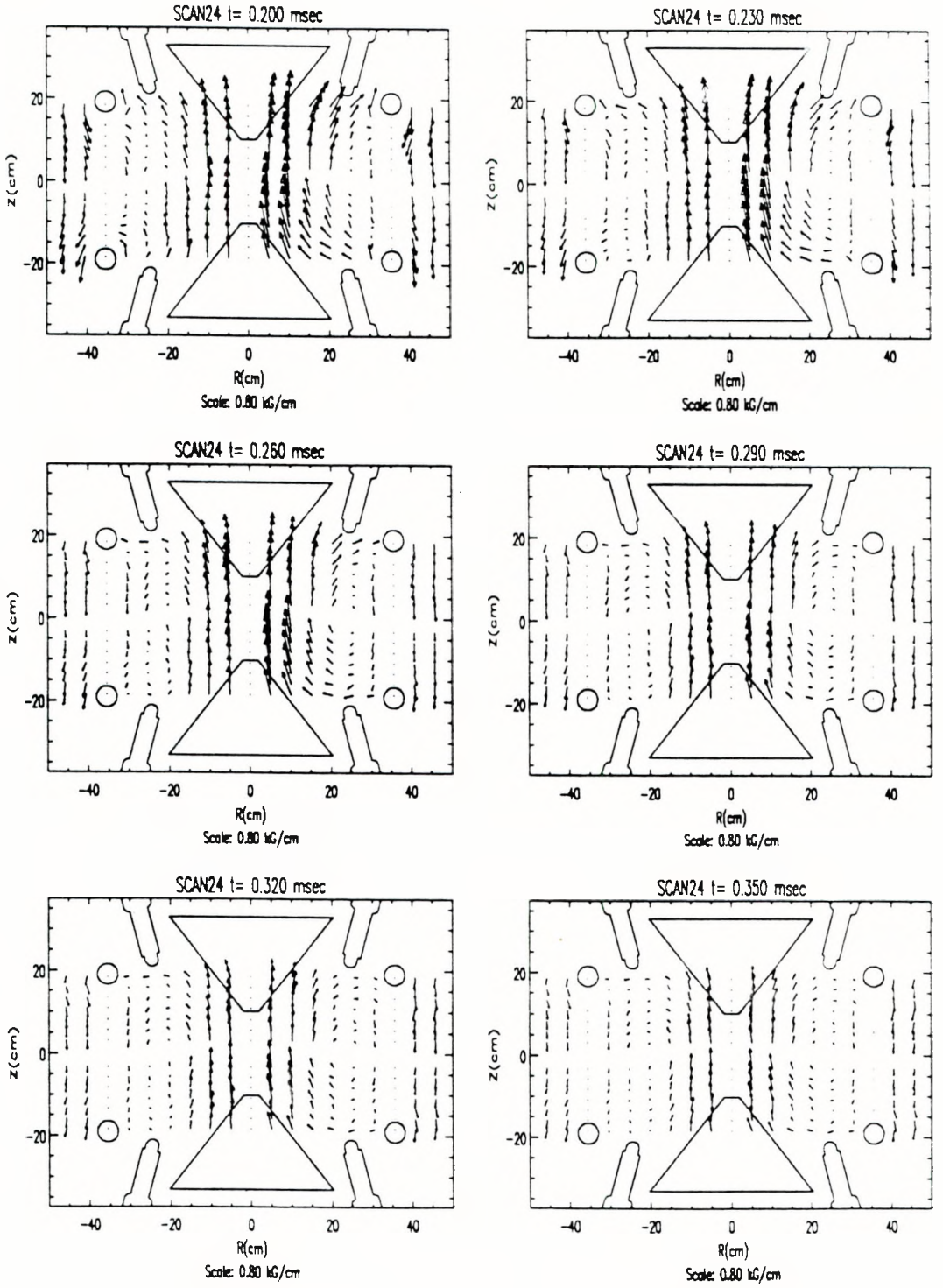

Figure 6.3: Poloidal field structure on the R-Z plane for SCAN24.

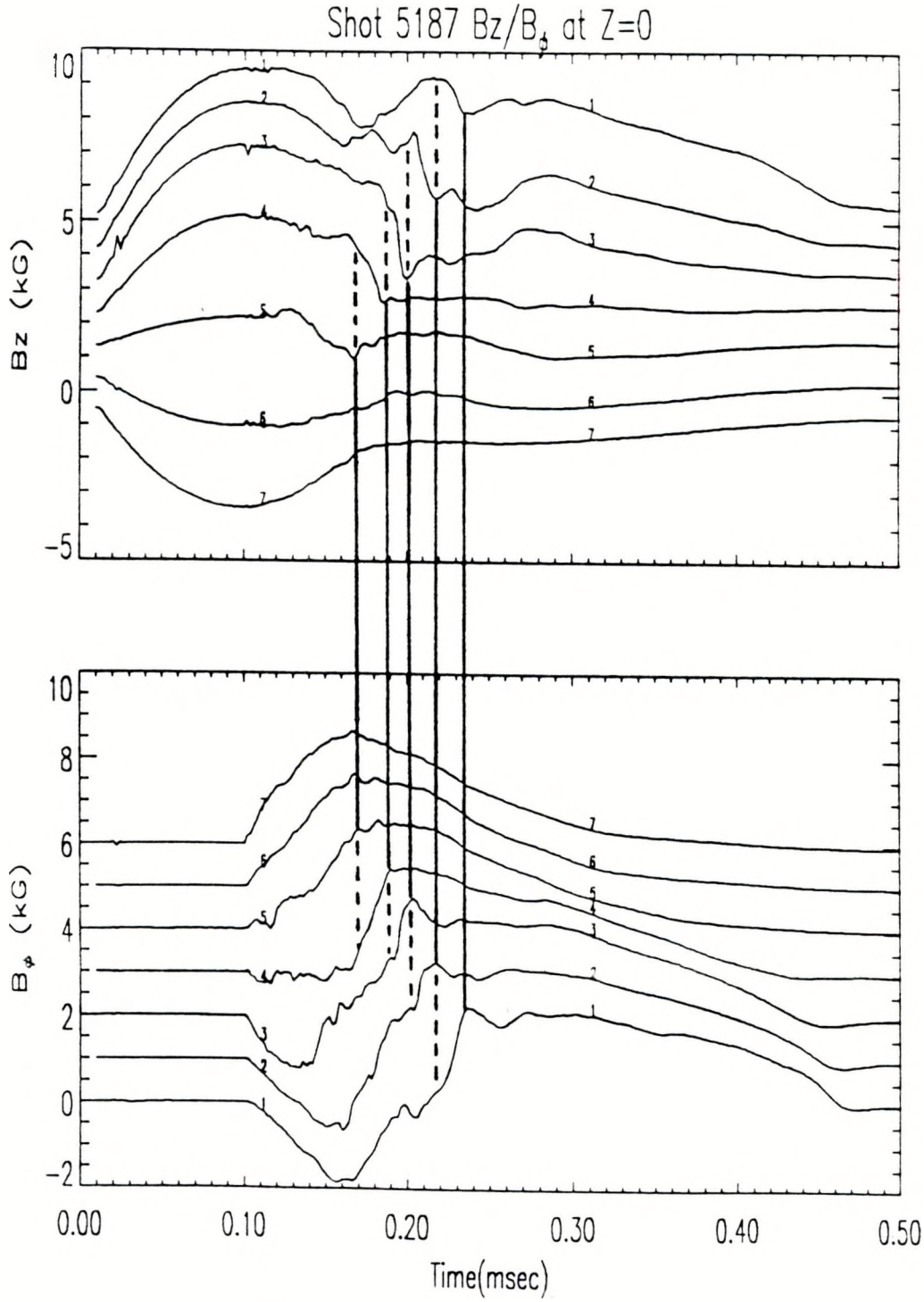

Figure 6.4: The magnetic field on the midplane for MS shot 5187 shows correlation between the B_z and B_ϕ fields. There is a 1 kG DC offset between two nearby coils. Locations #1-7 are at r=(7.18, 13.53, 19.88, 26.23, 32.58, 38.93, 45.28) cm.

The time delays between the sudden changes of the coil signals were all about $\simeq$ 16 μsec. This corresponds to a drift motion of the plasma on the midplane at a velocity $V_d \sim 6.35\text{cm}/16\mu\text{sec}$ [illegible] cm toward the axis.

The drop of the B_z signal when the I_z current passes the coil location can be explained as follow. During the formation time, the reversal coil current decreases in magnitude. A plasma current is induced in the toroidal direction to prevent the change of the poloidal fluxes. On the midplane, this induced current will increase the B_z field at smaller radius and will decrease its magnitude at larger radius. The B_z signal drops when this current sheet crosses a coil. When this current is large enough, the field reverses at larger radius and forms a closed flux surface, and the spheromak is produced.

Afterwards, fluctuations continue to occur in each coil signal with smaller magnitudes. All the signals change in such a way that the magnetic field profile approaches Taylor's minimum energy state configuration (described in the next section). When a spheromak magnetic field profile was developed, at t=0.28 msec for MS shot 5187, all the field signals started to decay exponentially.

The poloidal flux can be calculated from the B_z field measurements, with the assumption of axisymmetry,

$$\Psi(r,z) = \int_0^r 2\pi r' B_z(r',z)\, dr'$$

The value of the flux $\Psi(r,z)$ is strongly dependent on the choice of the origin, because of the weighting factor of r in the integral. In order to account for errors due to small shifts of the plasma center, a new center $r_c(z)$ was evaluated. Assuming that the plasma only shifts radially in the same plane where the measurements were made, then the maximum fluxes calculated at $\pm r$ must be the same after the center is corrected for.

$$\int_{r_c}^{-r_m} (r_c - r')\, Bz(r')\, dr' = \int_{r_c}^{r_m} (r' - r_c)\, Bz(r')\, dr'$$

The temporal development of poloidal flux contours for SCAN24 is shown in Fig. 6.5. For the data shown in Fig. 6.5, the B_z fields were averaged over $\pm Z$, then an iterative process was used to find the new symmetry point until

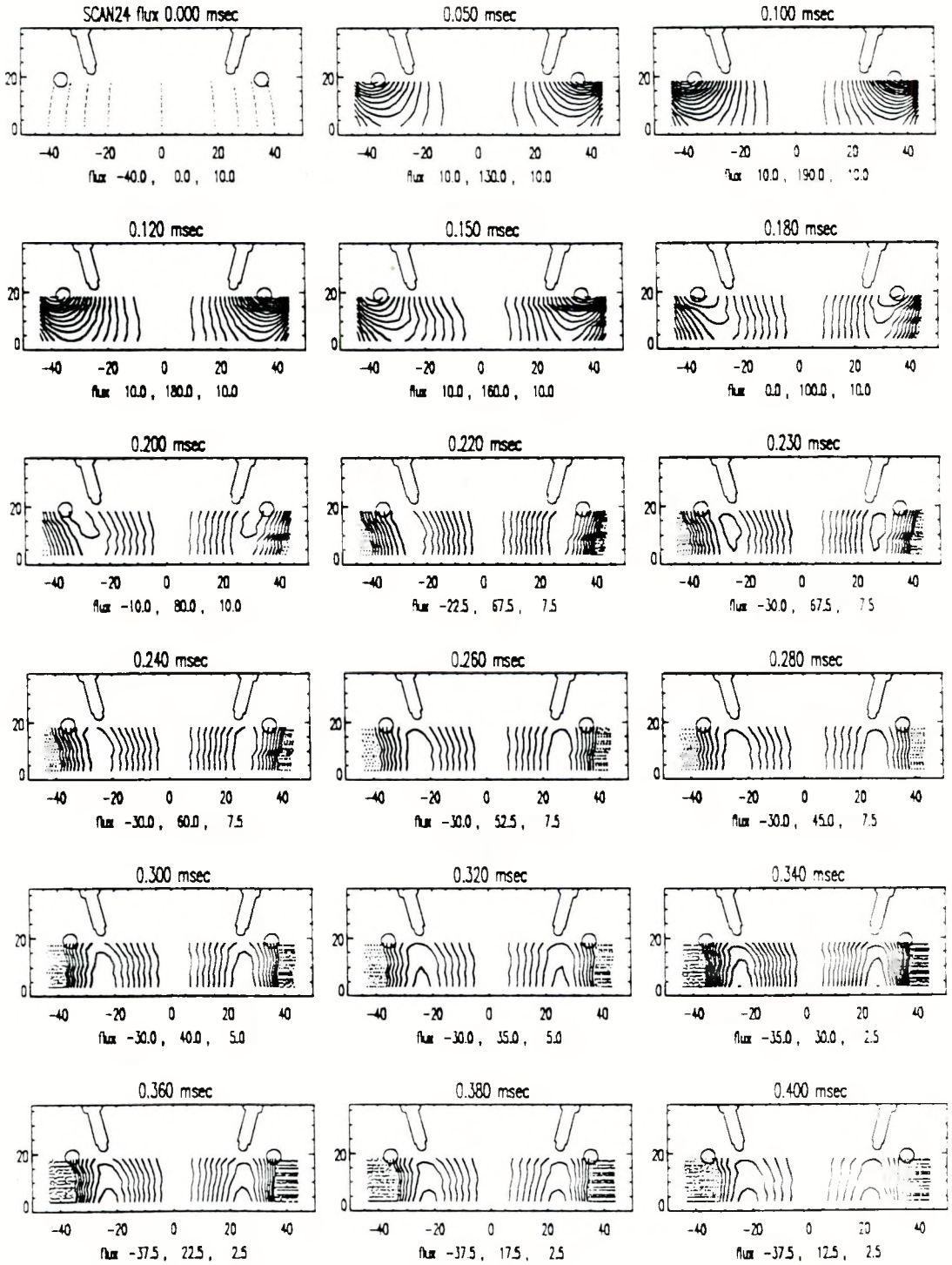

Figure 6.5: Poloidal flux contours for SCAN24 in cylindrical coordinate system (R-Z) with units of cm. Solid lines are fluxes inside the separatrix of the plasma. Dotted lines are the bias fluxes. Units are in mWeber. The minimum and maximum flux of each contour along with the flux increment are shown for each time step.

convergence is achieved. For SCAN24, the shift of the origin $r_c(z,t)$ is usually less than 2 cm, up to 4 cm shifts occur occasionally during the formation phase.

At t=0, only the bias flux is present in the chamber. Then at t=0.1 msec, the reversal flux starts to build up around the reversal coils. The I_z discharge is triggered at t=0.1 msec, and it is not until t=0.18 msec (peak of the I_z) that the flux contours show noticeable differences from the vacuum poloidal fluxes. The flux surfaces start to pull out from the reversal coils, and O-points are formed between the reversal coils and the midplane at t=0.23 msec. The O-points move toward the midplane, and at t=0.26 msec a single O-point is formed on the midplane. The spheromak configuration is formed. The formation process observed is qualitatively similar to the MS formation simulation reported by Guzdar and Finn.[25].

6.2. Taylor Minimum Energy State Spheromak

The poloidal flux (Ψ) contours for SCAN23 are shown in Fig. 6.6. When compared with Fig. 5.11, it shows that for most of the region, the contours of Ψ are lined up with the poloidal current (I_p) contours.

For a plasma in axisymmetric equilibrium, I_p is a poloidal flux function as indicated by Eqs. (2.18) and (2.19). It has been pointed out by Guzdar and Finn[25] that, in axisymmetric configuration, a toroidal flow v_ϕ is produced when I_p is not a function of Ψ.

$$\hat{\phi}\cdot\vec{J}\times\vec{B} = \hat{\phi}\cdot\left[\left(\nabla I_p\times\frac{\hat{\phi}}{2\pi r}\right)\times\left(\nabla\Psi\times\frac{\hat{\phi}}{2\pi r}\right)\right]$$

$$= \frac{1}{(2\pi r)^2}\,\hat{\phi}\cdot\nabla I_p\times\nabla\Psi \qquad (6.1)$$

The force in Eqs. (6.1) is balanced by inertia or viscosity. Since both I_p and Ψ are symmetric about the midplane, the flow v_ϕ is antisymmetric about $z=0$.

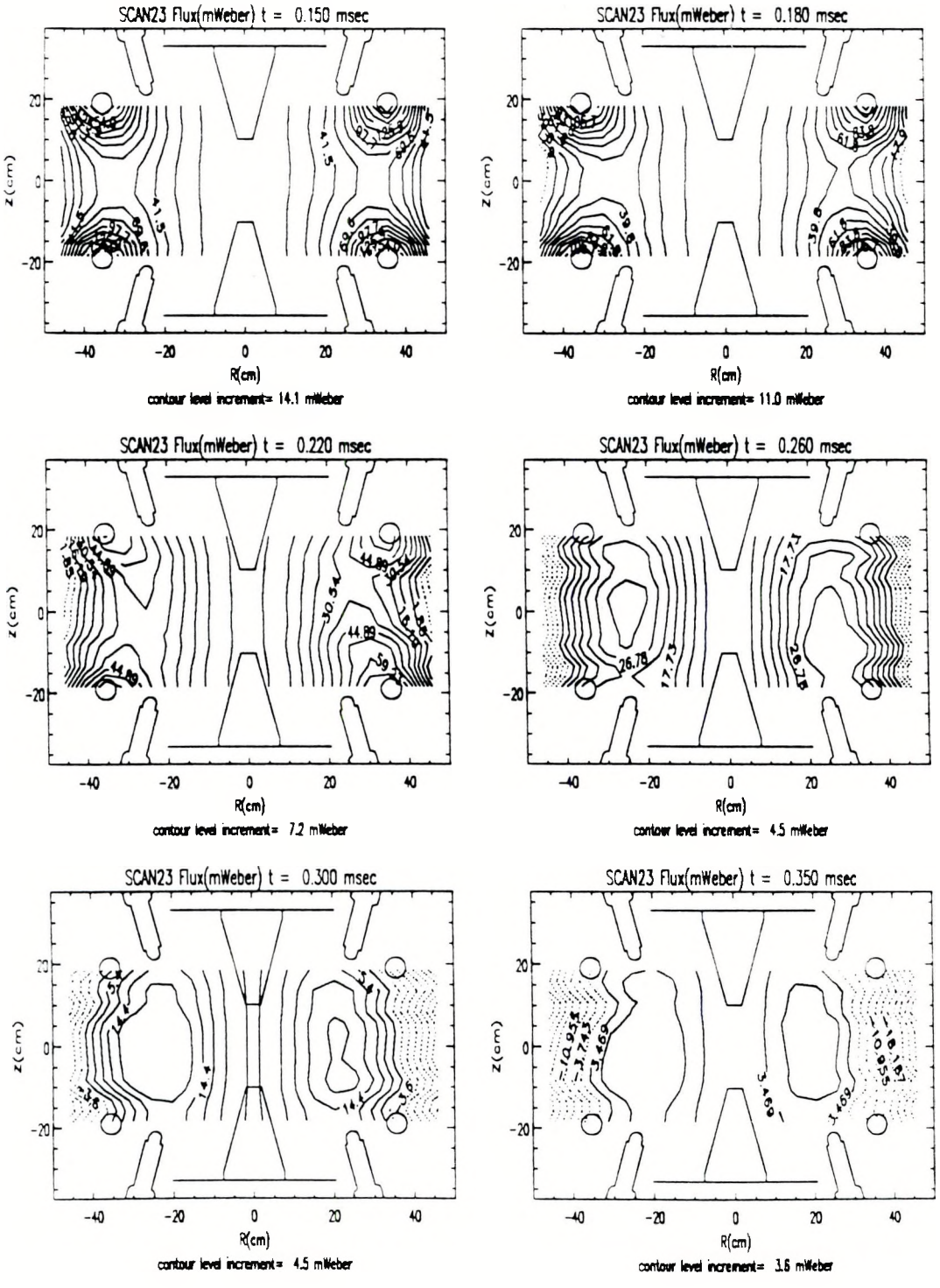

Figure 6.6: Poloidal flux contours for SCAN23.

With the simplified form of the Ohm's law $\vec{E} = -\vec{V} \times \vec{B} + \eta \vec{J}$, where η is the resistivity of the plasma, the equation of the magnetic field is

$$\frac{\partial \vec{B}}{\partial t} = \nabla \times \left(\vec{V} \times \vec{B} \right) - \frac{1}{\mu_0} \nabla \times \left(\eta \nabla \times \vec{B} \right)$$

Considering only the toroidal component of the field, the equation can be transformed to the following form :

$$\frac{\partial I_p}{\partial t} = -r^2 \nabla \cdot \left(\frac{I_p}{r^2} V_p \right) + 2\pi r^2 \vec{B}_p \cdot \nabla \left(\frac{V_\phi}{r} \right) + \frac{r^2}{\mu_0} \nabla \cdot \left(\frac{\eta}{r^2} \nabla I_p \right) \qquad (6.2)$$

The first term on the right hand side of Eq. (6.2) represents convection and compression of the toroidal field, and the third term represents the field diffusion. Guzdar and Finn explained the second term as **differential rotation**. If the rotation frequency $\omega = v_\phi / r$ is a constant on the poloidal flux surface Ψ, i.e. $\omega = \omega(\Psi)$, then the second term vanishes. In their simulation, without the the presence of resistivity and viscosity, the toroidal flow and the differential rotation effect produce a stable oscillation. Adding the resistivity and viscosity damps the oscillation and $I_p = I_p(\Psi)$ is obtained.

All the spheromak experiments to date indicated that during the formation phase, the plasma has a tendency to develop into a Taylor minimum energy configuration.[21,45–46] For the Taylor state spheromak, the ratio of the poloidal current to the poloidal flux is a constant, and it is independent of position (as described in Chapter 2).

$$\mu_0 I_p = k\Psi \qquad (6.3)$$

Figures 6.7 and 6.8 show the poloidal current I_p as a function of poloidal flux Ψ for SCAN23 and SCAN24. The data are taken from coils located at 168 different locations with multiple shots, (r range from -40.6 cm to 40.6 cm, z range from -18.42 to 18.42 cm). When the plasma is reduced to a smaller size, some coils became located outside the separatrix, and the flux had negative values. Fluxes with negative values are outside the range of the plot, and they are not shown in the figure. Before t=0.34 msec for SCAN 23, and before t=0.40 msec for SCAN24, most of the data stay on a line with a slope $k \simeq 12$

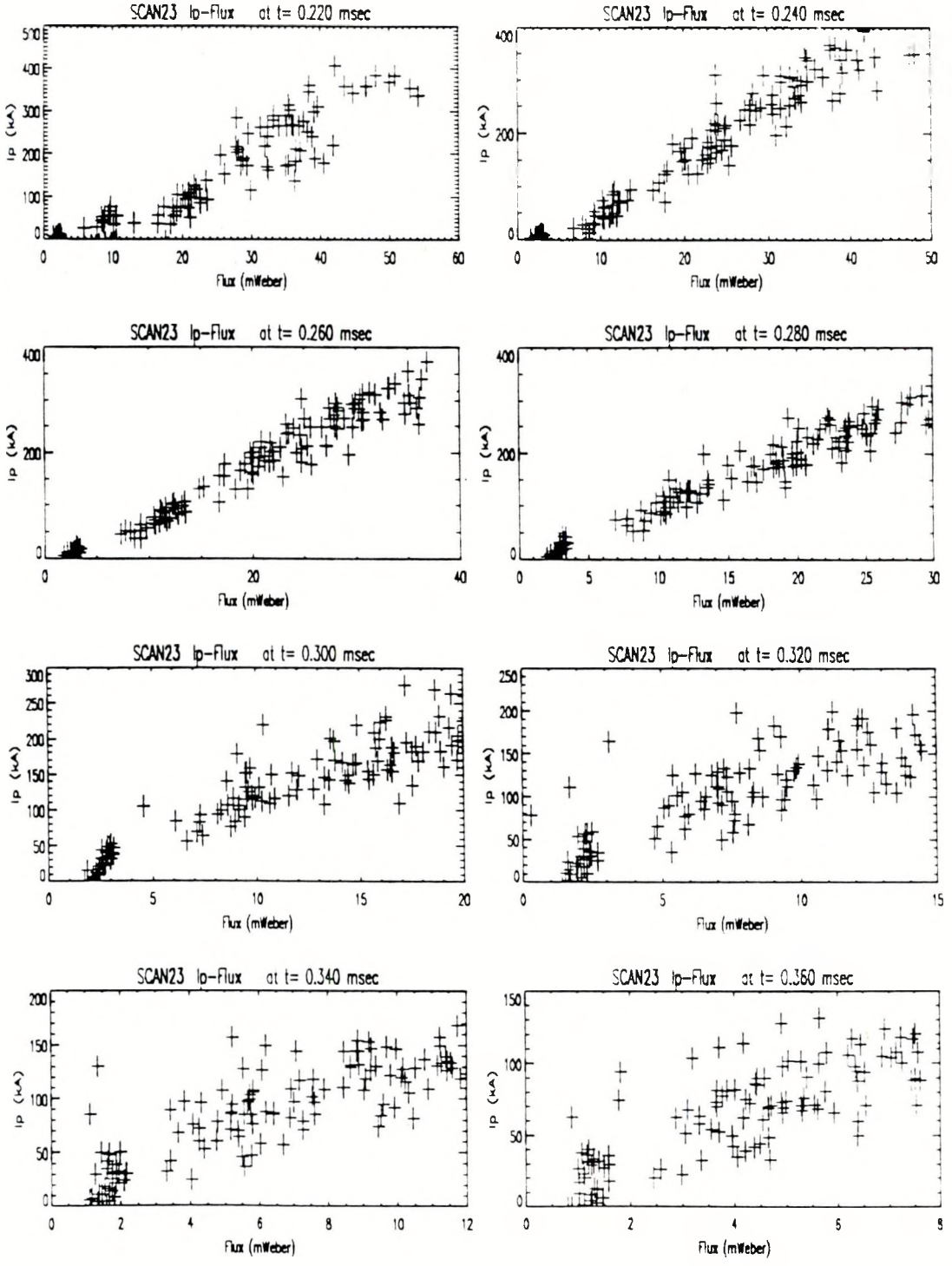

Figure 6.7: Measured poloidal current I_p as a function of poloidal flux for SCAN23.

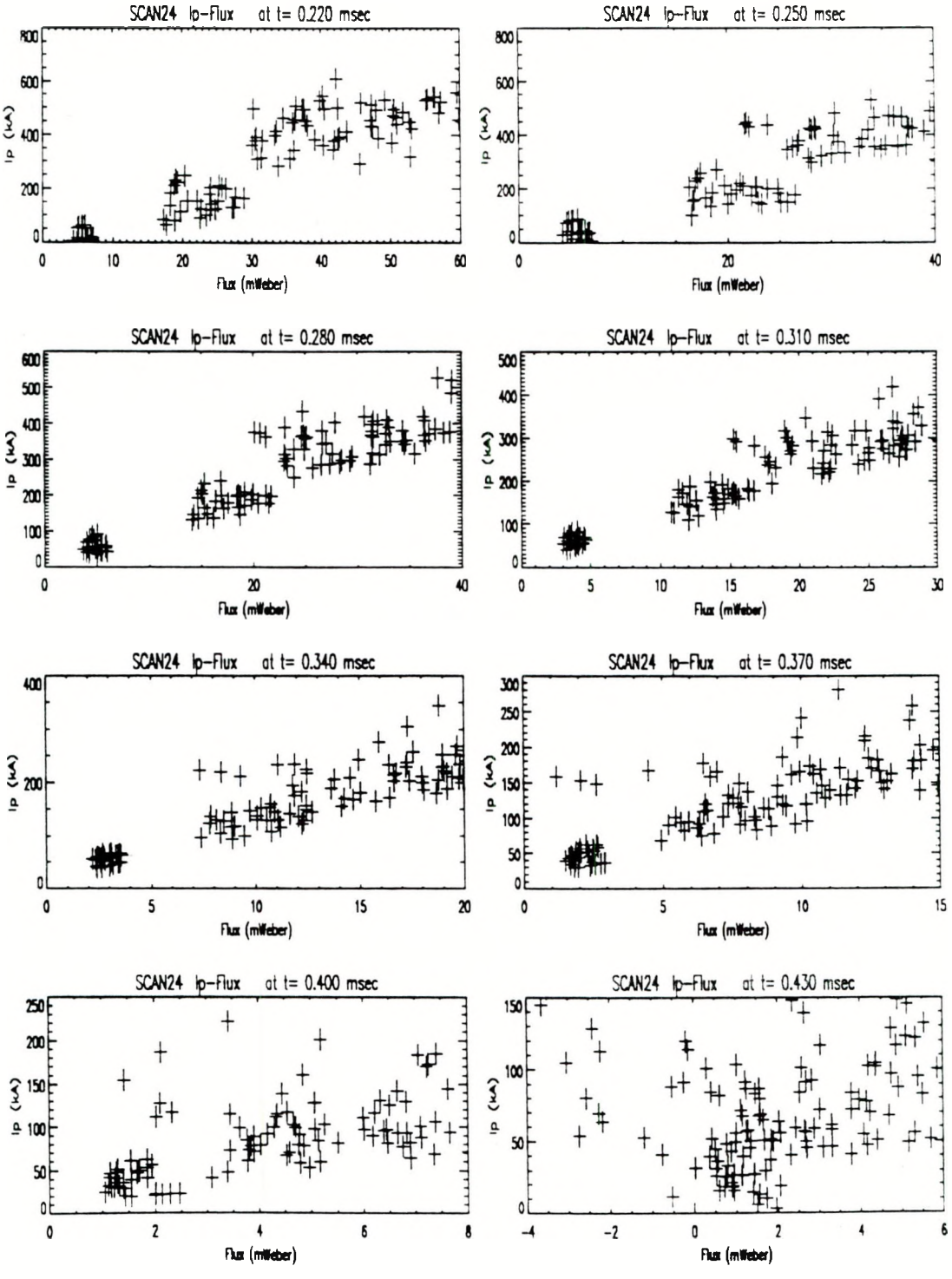

Figure 6.8: Measured poloidal current I_p as a function of poloidal flux for SCAN24.

m^{-1}. This is strong evidence that the spheromaks produced were close to the Taylor minimum energy state configuration.

The slope k as a function of radius r is shown in Figs. 6.9 and 6.10 for both scans. Higher k values appear at radius larger than 30 cm. This is due to the fact that some I_z current is still flowing in the vessel after the formation phase, which effectively increases the I_p values near the separatrix. At the radius outside the separatrix, the poloidal flux becomes negative so $k < 0$, and it is not shown in the diagram.

The constant k in Eqs. (6.3) is related to the size of the spheromak. For a classical spheromak, $kR = 4.4934$ where R is the separatrix radius. The value of k increases slightly for both scans at later times as the spheromak decayed to a smaller size. When the spheromak forms in MS, the plasma tends to have as large size as possible. It is the bias flux which limits the size of the plasma. The separatrix radius of the spheromak after formation in MS is about $\sim$ 35-45 cm. This corresponds to $k \sim$ 10.0-12.8 m^{-1} for the classical spheromak. The number is close to the k values derived from Eqs. (6.3) and shown in Figs. 6.9 and 6.10.

Due to the presence of the two glass plate, the current path between the reversal coils and the vacuum vessel was blocked for the SCAN24 plasma discharges. The poloidal current contours for the SCAN24 are shown in Fig. 6.11. It shows that, at t=0.22 msec, the poloidal current flowing inside the radius of the electrodes ($\simeq$25 cm) is about 560 kA, while it was about 200 kA for SCAN23 (see Fig. 5.11). The peak values of I_z currents are about 730 kA and 550 kA for SCAN24 and SCAN23 respectively. The increase of the poloidal current near the axis is mainly due to the presence of the two glass plates which force all the current to flow inside the radius of the reversal coils. Since the ratio of I_p to Ψ is roughly constant, a spheromak with more poloidal flux was formed in SCAN24 case.

The poloidal flux on the midplane $\Psi(t, r)$ for SCAN23 and SCAN24 is shown in Fig. 6.12. For SCAN23, the poloidal flux at r=20.32 cm (dotted

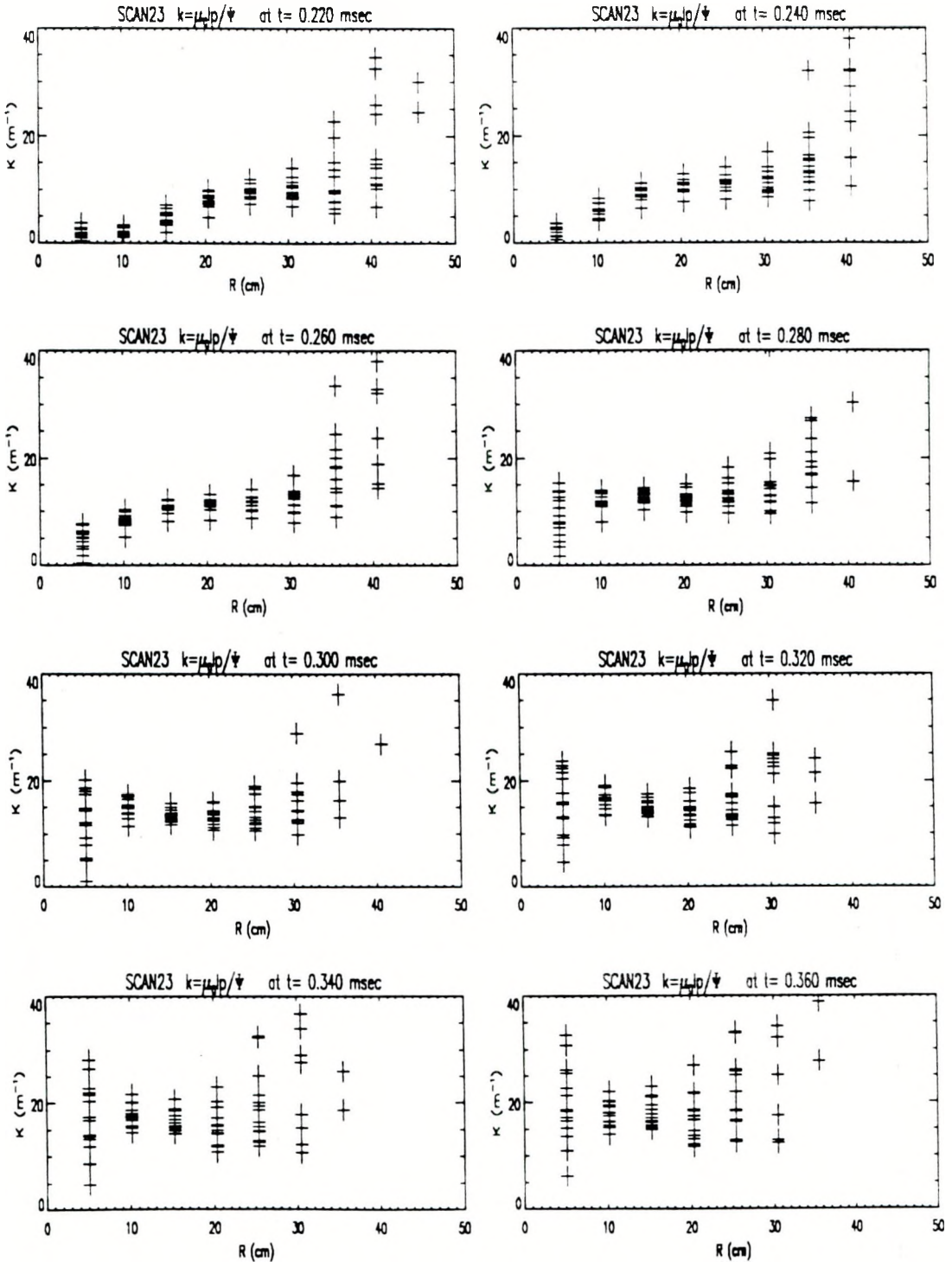

Figure 6.9: $k = \mu_0 I_p/\Psi$ as a function of radius for SCAN23.

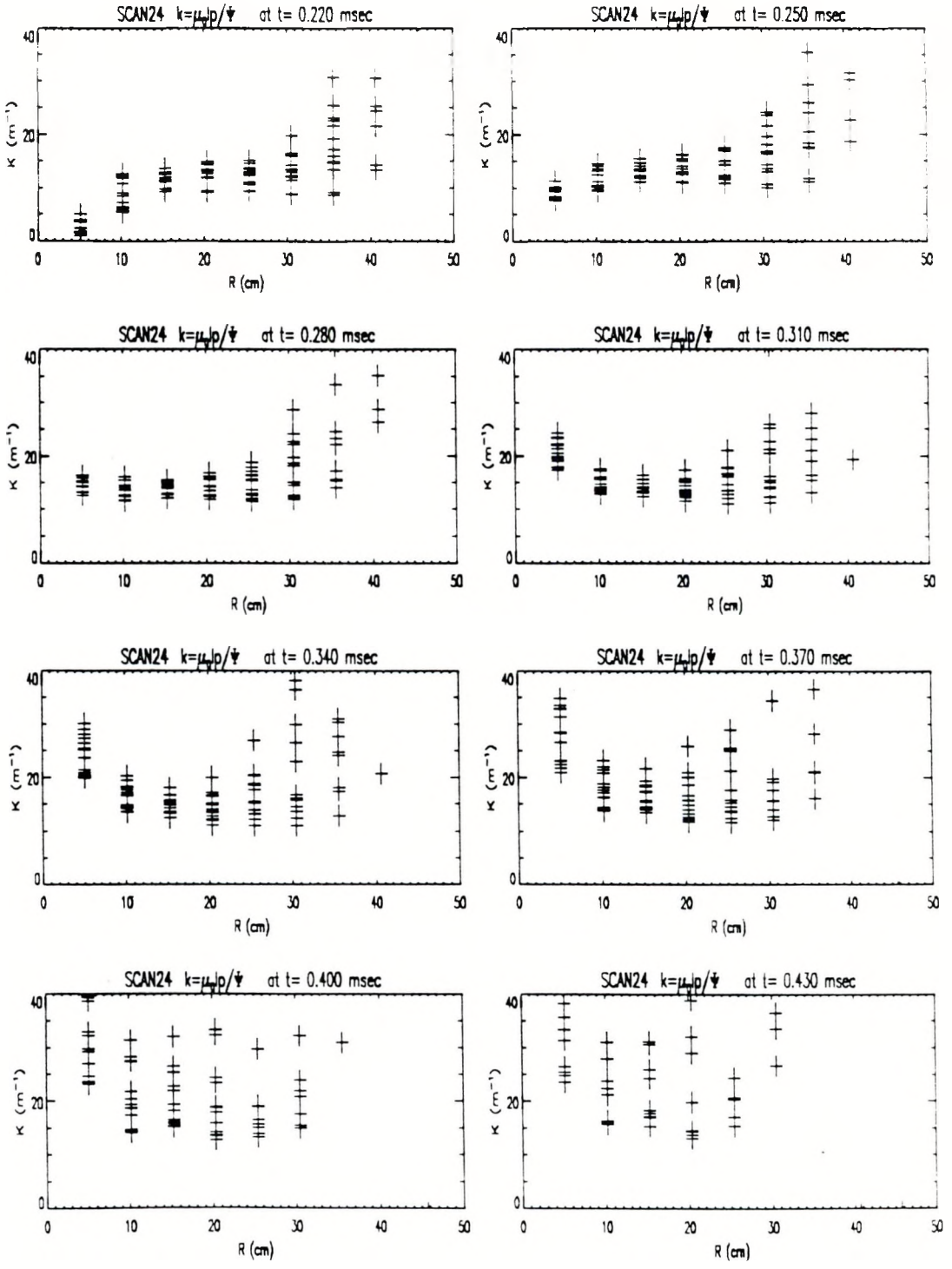

Figure 6.10: $k = \mu_0 I_p / \Psi$ as a function of radius for SCAN24.

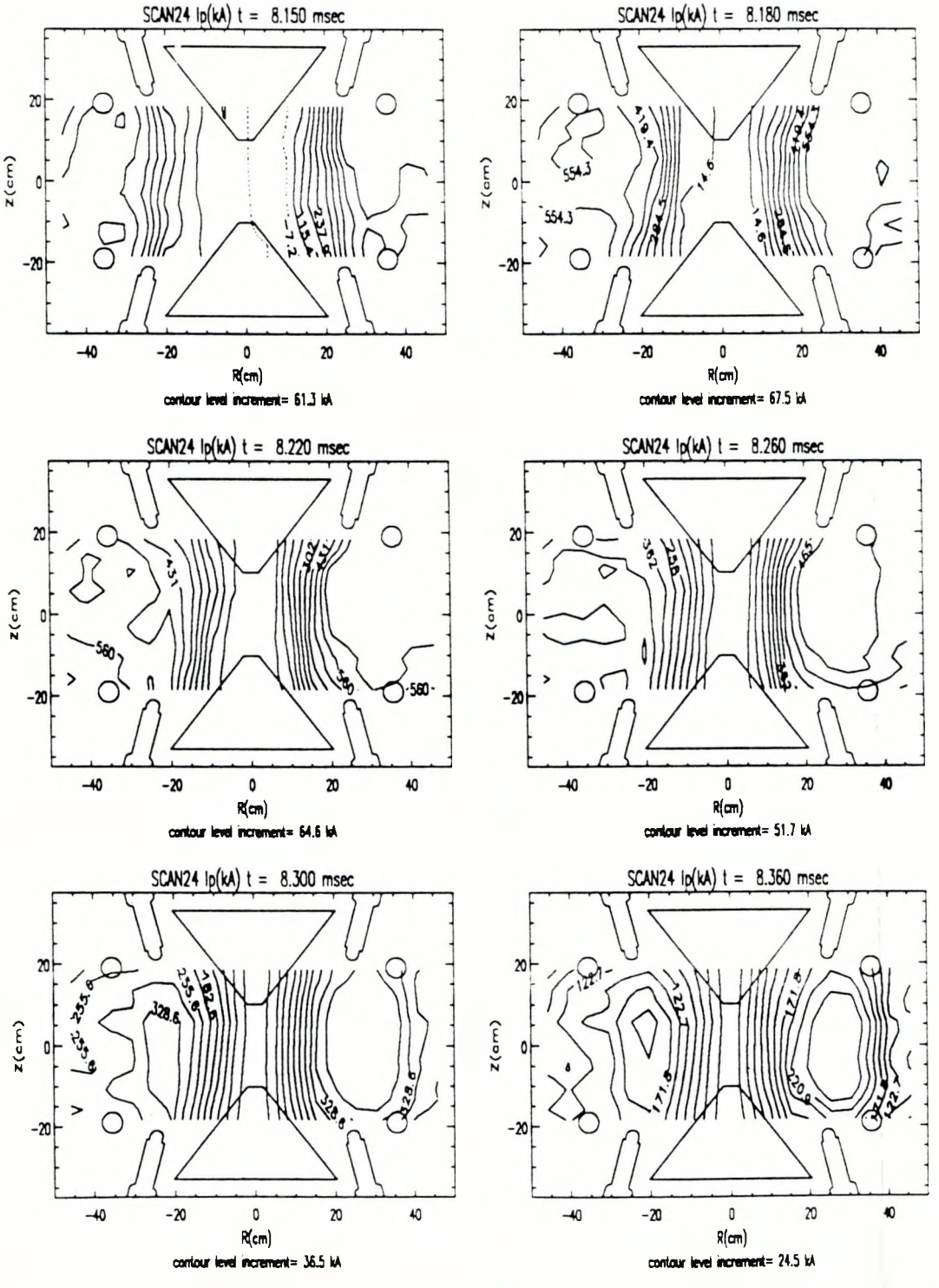

Figure 6.11: Poloidal current contours for SCAN24.

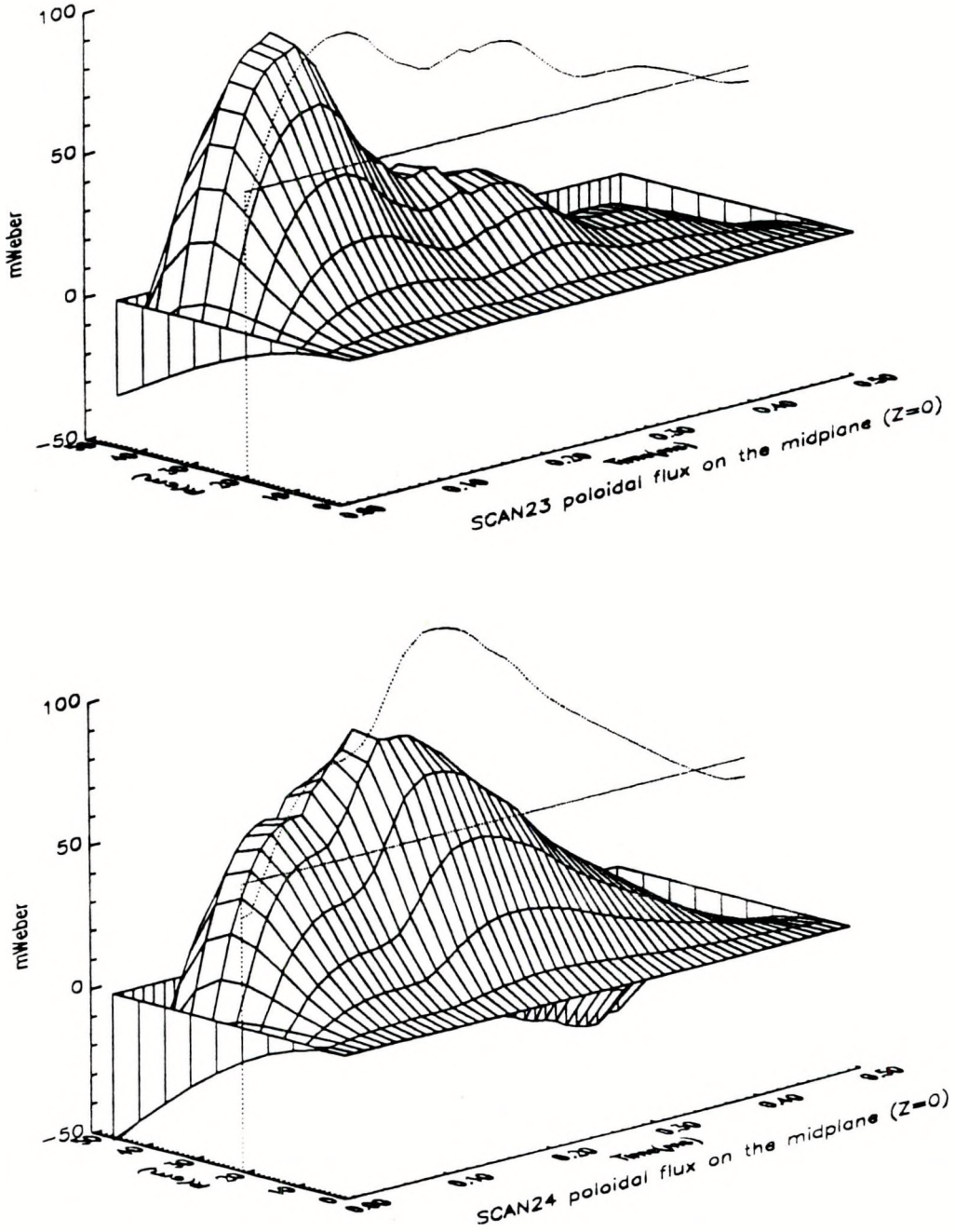

Figure 6.12: 3-D plots of the poloidal flux $\Psi(t, r)$ on the midplane for SCAN23 and SCAN24. Data shown are 5.08 cm apart in r-direction and 10 μsec apart in time. The dotted curves, offset 50 mWeber in z direction, show the poloidal fluxes $\Psi(t)$ at r=20.32 cm.

curve) decreases with the reversal coil current between t=0.10-0.18 msec. During t=0.18-0.26 msec, the poloidal flux is roughly constant. For SCAN24, the poloidal flux at r=20.32 cm, increases after the [illegible] triggered. Between t=0.17-0.22 msec, the poloidal flux stays at a roughly constant value.

During the formation phase, the magnetic profile evolves in such a way that the ratio of the poloidal current to the poloidal flux in the plasma approaches a constant value. When there is not enough I_z current in the central region of the vessel, as in the case of SCAN23, less toroidal current is observed in the plasma. The total poloidal flux is produced from the reversal coil current and the toroidal plasma current in the vessel. The reversal coil current decreases during the formation phase. The poloidal flux generated by the induced toroidal current is not enough to compensate for the loss of the total poloidal flux due to the decrease of the reversal current. The effect is that the total poloidal flux decreases as the reversal current drops. After t=0.18 msec (peak of the I_z current), there is more current flowing into the central region and enough toroidal current is generated to keep the flux constant. At t=0.26 msec, the reversal coil current was crowbarred (see Fig. 6.1), and the flux started to decay.

For SCAN24, there is more poloidal current flowing into the central region of the vessel. However, the reversal current is smaller for the SCAN24 case so at the peak of the reversal current there is less poloidal flux in the chamber compared to SCAN23. Therefore, more toroidal current was observed such that the ratio of the poloidal current to poloidal flux approaches a constant value as the spheromak is formed. At t=0.1 msec on the midplane, the poloidal flux at r=20.32 cm is 46.6 mWeber for SCAN23. At the same time, there is only 34.1 mWeber poloidal flux for SCAN24 at the same location. However, at t=(0.20, 0.25) msec, there is (25.4, 29.1) mWeber poloidal flux for SCAN23, and (70.0, 55.5) mWeber poloidal flux for SCAN24.

The B_z field on the midplane is plotted as a function of radius r and time t with 3-D plots and shown in Fig. 6.13. For SCAN23, between t=0.1-0.2 msec,

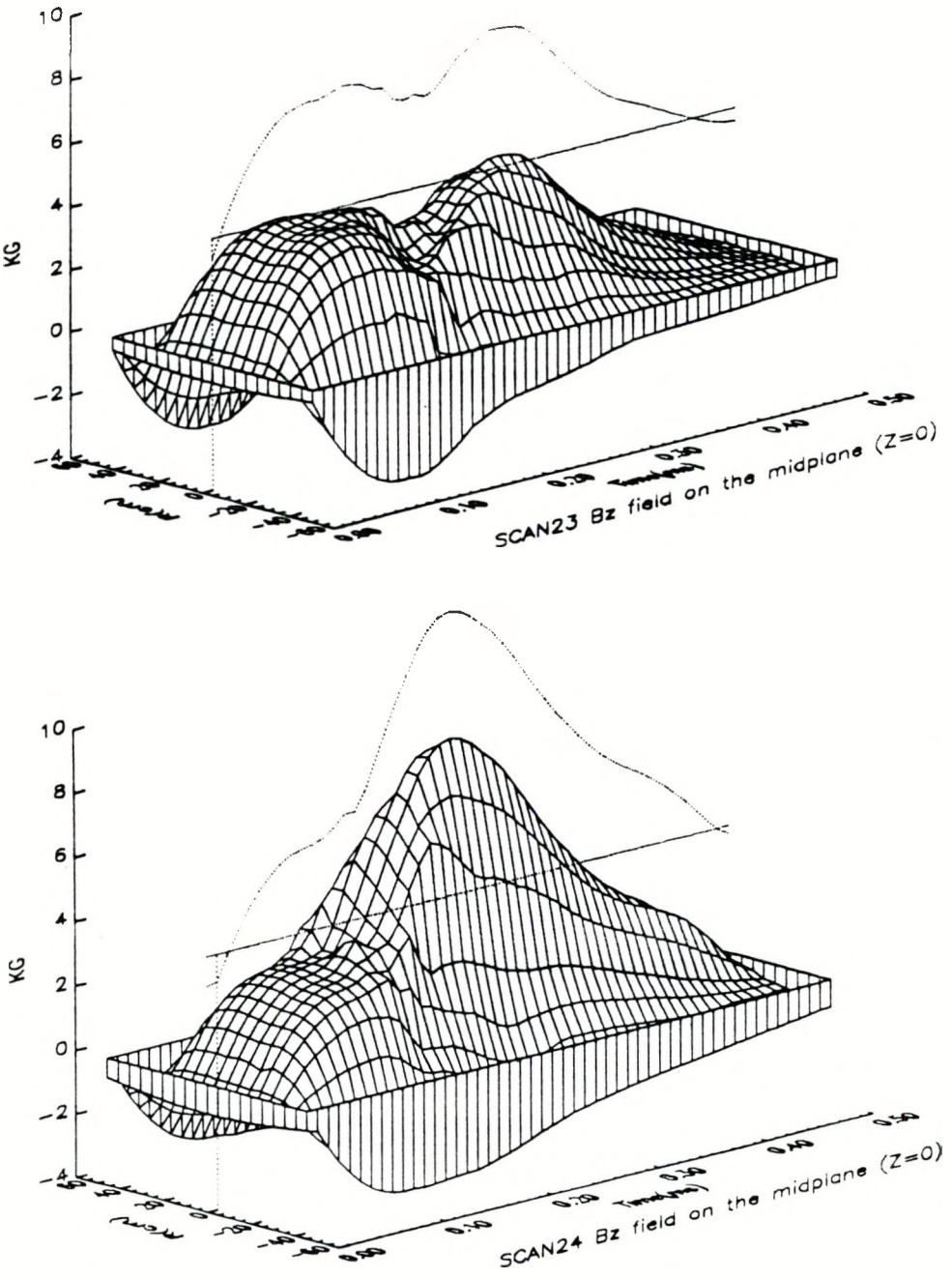

Figure 6.13: 3-D plots of the magnetic field B_z (t,r) on the midplane for SCAN23 and SCAN24. The dotted curves show the magnetic fields B_z (t) at the plasma center.

the magnetic field on the axis decreased as the reversal current dropped. The B_z field started to increase its magnitude 20 μsec after peak of the I_z current (I_z peaks at t=0.18 msec). A second peak (4.1 kG) appeared at the time when the spheromak was formed. For SCAN24, the B_z field on the axis has its highest value (8.6 kG) at t=0.22 msec.

We have shown that the ratio of the poloidal current to poloidal flux I_p/Ψ is roughly a constant when the spheromak is formed, and in the SCAN24 condition, the poloidal flux is larger than that of SCAN23 due to more I_z current flowing in the central region of the chamber during the formation. If we just increase the I_z current alone, the poloidal flux will not continue to increase linearly with the I_z current indefinitely. The reversal coil current also plays an important role during the formation phase of the MS spheromak. This is related to the magnetic helicity injection. The total magnetic helicity of the plasma produced is limited by the helicity injected during the formation phase. The magnetic helicity injection will be discussed in Chapter 8.

6.3. Decay of the Spheromak

Since most of the spheromak field is generated by the plasma current, it will decay due to the finite resistivity of the plasma when the external driving mechanism (e.g. I_z current in MS) is turned off. For plasma with resistivity η, the simplified form of Ohm's law is

$$\vec{E} = -\vec{V} \times \vec{B} + \eta \vec{J} \tag{6.4}$$

With the aid of Faraday's law

$$\nabla \times \vec{E} = -\frac{\partial \vec{B}}{\partial t}$$

and assuming a spatially constant resistivity, we have

$$\begin{aligned} \frac{\partial \vec{B}}{\partial t} &= -\nabla \times \vec{E} \\ &= -\eta \nabla \times \vec{J} + \nabla \times \left(\vec{V} \times \vec{B} \right) \end{aligned} \tag{6.5}$$

MS shot	4150		5194		5475	
coil #	2	3	2	3	2	3
r (cm)	12.7	20.3	13.5	19.9	13.5	19.8
τ_B^* (μsec)	92.	97.	73.	68.	109.	349.
k (m^{-1})	11.4		10.5		11.4	
η ($\mu\Omega$-m)	105.	100.	156.	168.	88.7	27.7
T^{**} (eV)	4.5	4.6	3.4	3.3	5.0	10.9

* between t=0.30-0.35 msec.

** Spitzer resistivity is assumed, $\eta = 9.9 \times 10^{-4} T^{-3/2} \Omega$-m, with $\ln \Lambda = 9.6$ and $Z = 1$.

Table 6.1: Estimate of the resistivity η and the electron temperature T_e from the B_z field decay time τ_B.

For a spheromak in Taylor's minimum energy state, $\nabla \times \vec{B} = k\vec{B}$, so $\mu_0 \vec{J} = k\vec{B}$, and

$$\nabla \times \vec{J} = \frac{k}{\mu_0} \nabla \times \vec{B} = \frac{k^2}{\mu_0} \vec{B}$$

If the spheromak decays with a constant separatrix radius (i.e. $\vec{V} = 0$), then

$$\frac{\partial \vec{B}}{\partial t} = -\frac{\eta k^2}{\mu_0} \vec{B}, \tag{6.6}$$

and the magnetic field decays exponentially with a time constant of $\tau_B = \mu_0 / \eta k^2$.

$$B = B_0 e^{-\frac{\eta k^2}{\mu_0} t} \tag{6.7}$$

It has been shown that the spheromak formed in MS is close to Taylor's minimum energy state. Figure 6.5 shows that the separatrix radius changes slightly between t=0.25-0.35 msec. The magnetic field decay time τ_B can be calculated directly from the probe measurements. We can then estimate the resistivity of the plasma from the field decay time.

The resistivities η estimated from the B_z field decay time between t=0.30-0.35 msec for MS shots (4150, 5194 and 5475) are listed in Table 6.1. MS shot 4150 (magnetic field profile shown in Fig. 5.8) was taken before our attempt of controlling the current path. Shot 5194 (Fig. 5.16) was taken when the I_z current path was blocked by two polyethylene sheets. When the spheromak is

formed, the magnetic field strength of shot 5194 is doubled compared to shot 4150. The ohmic heating power is proportiona.. to the square of the current density J, and for the classical spheromak, the current density J scales linearly with the magnetic field B. Therefore, the ohmic heating power of shot 5194 has been increased four times compared to MS shot 4150, so one would expect higher T_e and longer magnetic field decay time. However, due to the presence of the polyethylene sheets, the line averaged electron density is very high: 6-8$\times 10^{21}$ m^{-3} between t=0.30-0.35 msec. This is an order of magnitude higher than the typical electron density (Fig. 6.14).[26] The field decays even faster due to the high density of plasma which effectively lower the plasma temperature.

Shot 5475 (Fig. 6.15) was taken after the polyethylene sheets had been replaced by two glass plates. The electron density was measured to be about 8-10$\times 10^{20}$ m^{-3} . The peak field at r=7.2 cm was 9.6 kG which is three times the peak field in shot 4150 when the spheromak was formed. The decay time of coils #2 and #3 are both longer compared with the decay time of the other two shots. It also shows that at r=19.8 cm, which is close to the magnetic axis ($\simeq$24 cm), the B_z field has longer decay time (349μsec) compared to the decay time of coil #2 (109μsec). It appears that the plasma is hotter near the magnetic axis for shot 5475.

The Spitzer resistivity is a strong function of T_e,[2]

$$\eta = \frac{m_e^{1/2} Z e^2 \ln\Lambda}{6\sqrt{6}\pi\varepsilon_0^2 (kT)^{3/2}}$$
$$= 1.03 \times 10^{-4} Z \ln\Lambda \, T_e^{-3/2} \ \Omega\text{-m} \qquad (6.8)$$

where Z is the charge of the ion in the plasma and $\ln\Lambda$ is the Coulomb logarithm

$$\ln\Lambda \equiv \ln\left(\frac{12\pi(\varepsilon_0 k T_e)^{3/2}}{n_e^{1/2} Z e^3}\right)$$
$$= 30.37 - \ln\left(\frac{Z n_e^{1/2}}{T_e^{3/2}}\right)$$

with T_e in eV and n_e in m^{-3} . The value of the Coulomb logarithm is relatively insensitive to the value of T_e. With Z=1, $n_e \sim 10^{21}$m^{-3} and $T_e \sim 10$ eV, then

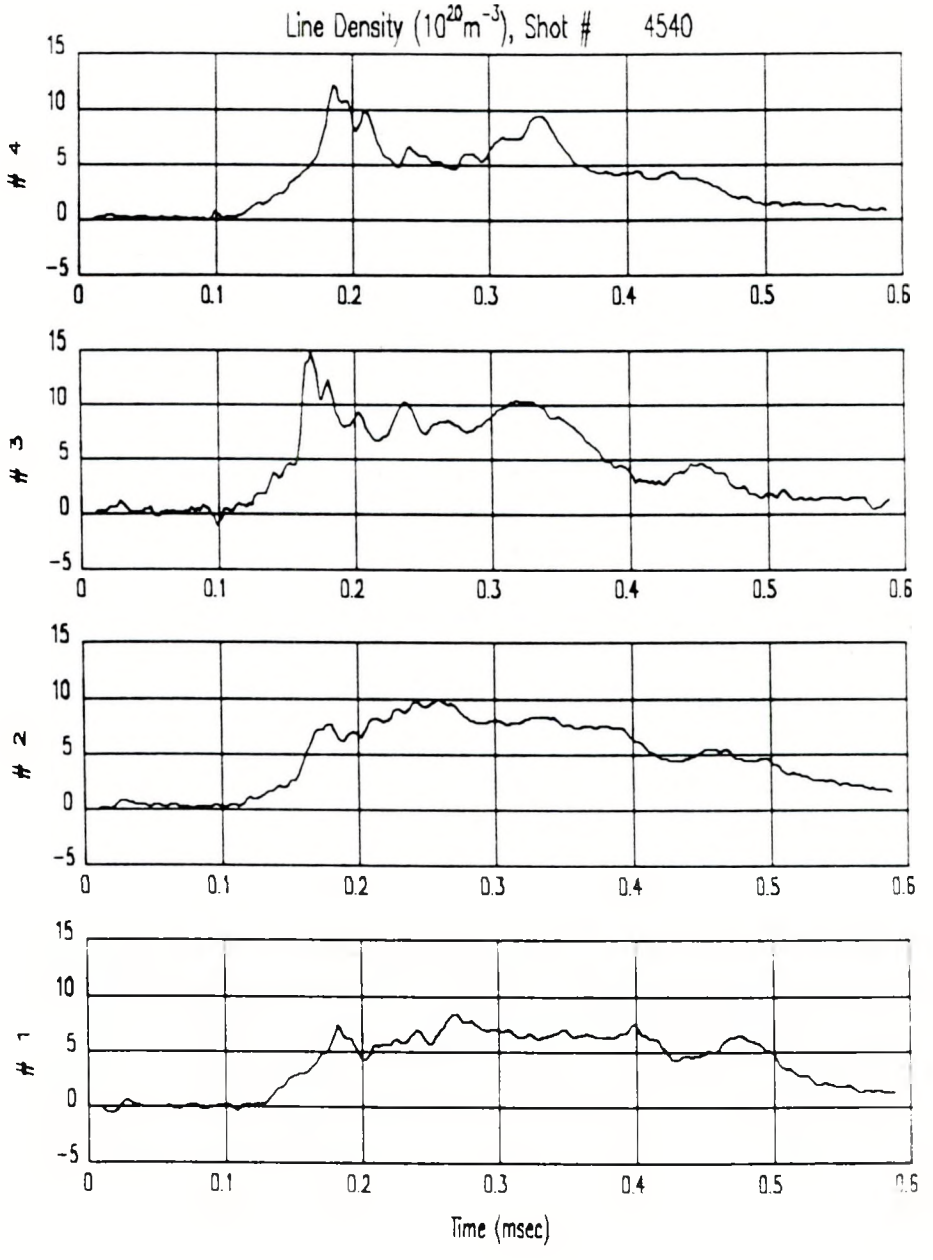

Figure 6.14: Typical line averaged electron density on the midplane. The chord parameters for traces #1-4 are r=(3.81, 11.43, 22.86, 30.48) cm. The chord parameter is defined as the shortest distance between the line of sight and the machine axis.

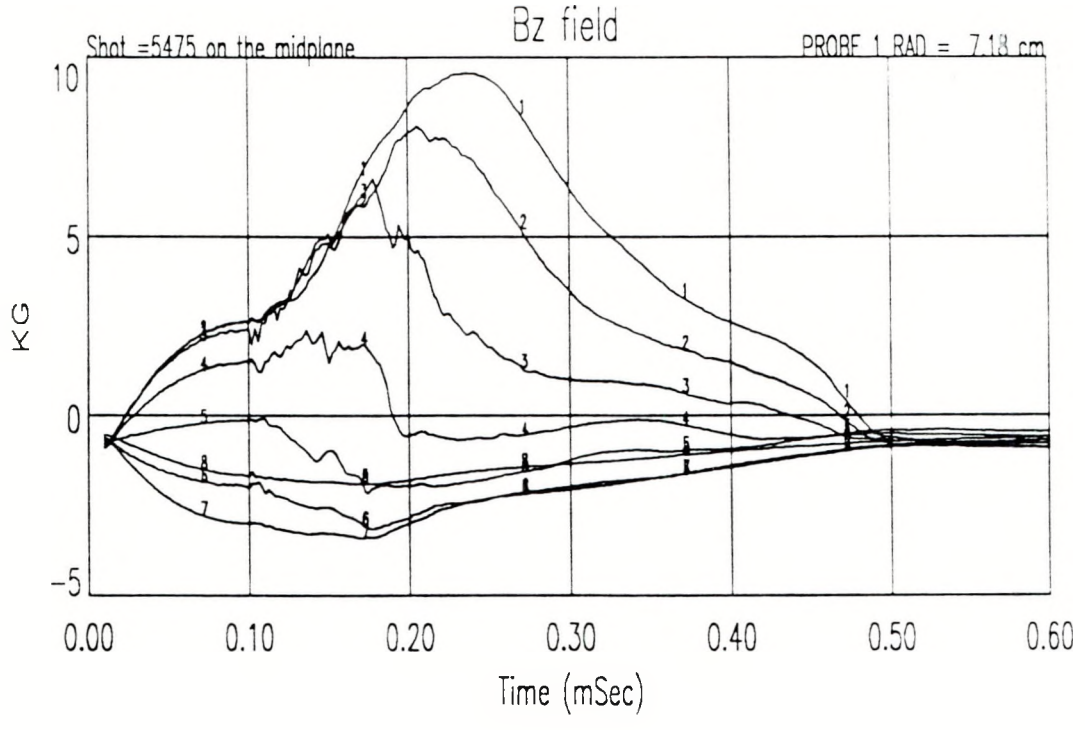

Figure 6.15: B_z fields on the midplane for MS shot 5475.

$\ln \Lambda = 9.6$. The electron temperatures of the plasmas are then estimated with Eq. (6.8) and shown in Table 6.1. The estimated electron temperature T_e is smaller than 15 eV which is consistent with the electron temperature obtained from the spectroscopy analysis (Fig. 6.16).

The magnetic energies of SCAN23 and SCAN24 are shown in Fig. 6.17 as functions of time. Due to the presence of the bias field, the minimum value of the total poloidal energy is not zero. Equations (7.6) and (7.7) indicate that, for spheromak in equilibrium and without any external current source, the poloidal magnetic energy is equal to the toroidal magnetic energy for a force-free spheromak, and that there is more poloidal magnetic energy for plasma with finite pressure. Figure 6.17 shows that the toroidal magnetic energy is larger than the poloidal magnetic energy between t=0.25-0.30 msec for both

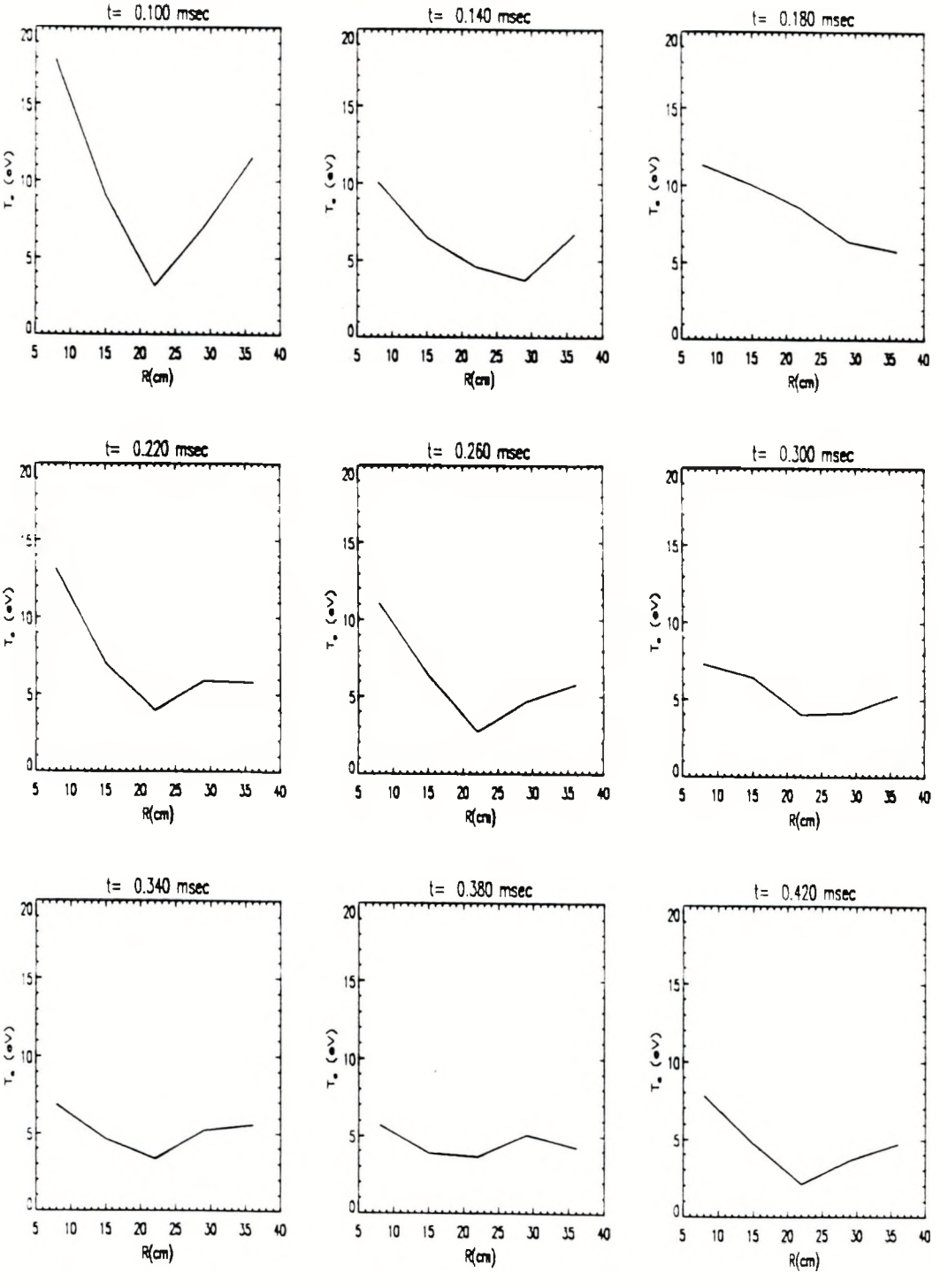

Figure 6.16: Typical electron temperature calculated from the CIV to CIII line ratio.

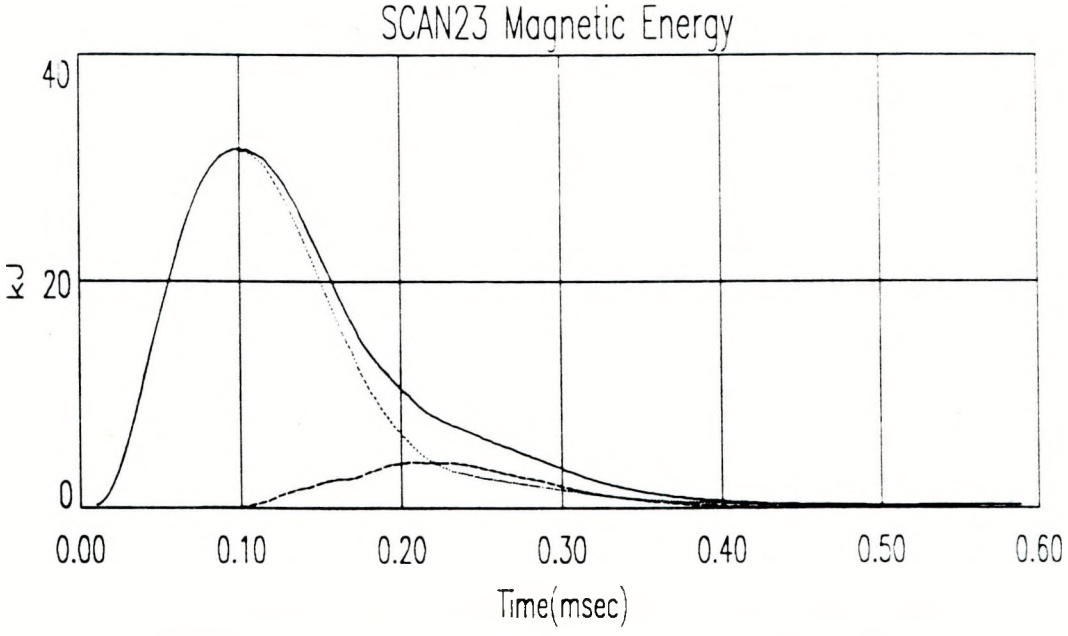

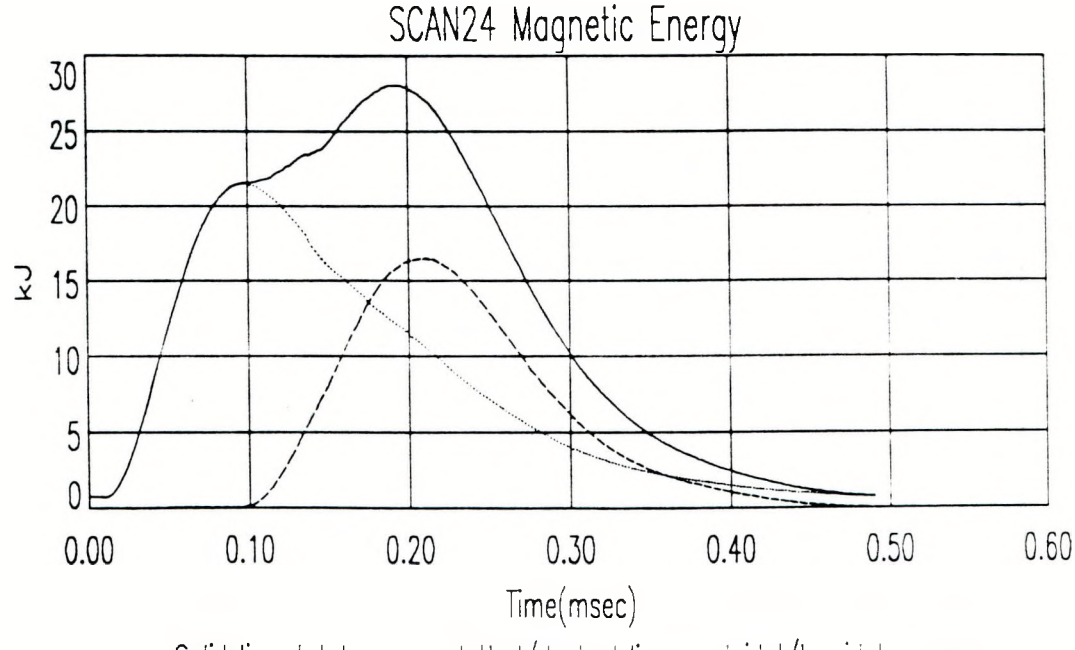

Figure 6.17: Temporal development of the magnetic energy for SCAN23 and SCAN24. The solid curve is the total magnetic energy.

t=0.30-0.40 msec	SCAN23	SCAN24
energy decay time $\tau_W(\mu\text{sec})$	57.8	70.0
resistivity$<\eta>$ ($\mu\Omega$-m)	75	62
temperature T_e (eV)	5.6	6.3
Magnetic energy W^* (kJ)	3.5	10.2
plasma beta β_{vol}^{**}	8.3%	3.2%

* Magnetic energy at t=0.3 msec.
** Plasma density $\sim 6 \times 10^{20}$ m^{-3} .

Table 6.2: Comparison of SCAN23 with SCAN24.

scans. This is attributed to the I_z current that is not completely off during that time and therefore, increases the toroidal energy of the plasma.

The magnetic energy decay time and other parameters for both scans are listed in Table 6.2. Between t=0.3-0.4 msec, the total magnetic energy decay times τ_W for SCAN23 and SCAN24 were 57.8μsec and 70.0μsec, respectively. The volume averaged resistivity is defined as

$$<\eta>_{\text{vol}} = \frac{\mu_0}{2\tau_W <k>^2}$$

where $<k>$ is the volume averaged k. With $<k>$=12, the volume averaged resistivities are 7.5×10^{-5} and $6.2 \times 10^{-5}\Omega$-m for SCAN23 and SCAN24 respectively. The volume averaged electron temperatures are estimated to be 5.6 eV and 6.3 eV.

The plasma beta may be estimated with the assumption that the ion temperature follows the electron temperature closely. The line averaged electron densities, between t=0.30-0.35 msec, are 4-6$\times 10^{20}$ m^{-3} and 6-8$\times 10^{20}$ m^{-3} for SCAN23 and SCAN24 respectively. The characteristic time required for a 90° deflection in the center of mass system for electron-ion collisions is[2]

$$\tau_{90}^{ei} = \frac{6\sqrt{3}\pi m_e^{1/2}\varepsilon_0^2 (kT)^{3/2}}{n_i (Ze^2)^2 \ln\Lambda} = 2.38 \times 10^{11} \frac{T^{3/2}}{n_i Z^2 \ln\Lambda} \qquad (6.9)$$

For "quasineutral" plasma having negligible impurity content (Z=1), $n_i \sim n_e \sim 6 \times 10^{20}\text{m}^{-3}$. The collision time $\tau_{90}^{ei} \sim 0.24$ ns, with $T \sim 6$ eV and

$n_i \sim 6 \times 10^{20} \mathrm{m}^{-3}$. The assumption of the "quasineutrality" is reasonable since the Debye length[47]

$$\lambda_D \equiv \left(\frac{\varepsilon_0 kT}{ne^2}\right)^{1/2} = 7430\left(\frac{T}{n}\right)^{1/2} \tag{6.10}$$

is 7.43×10^{-7} m which is much smaller compared to the dimension of the MS chamber. The characteristic time for energy transfer between the electron and ion is $\tau_E^{ie} \sim (m_i/m_e)\tau_{90}^{ei} = 0.88\mu$sec for deuterium gas, which is much smaller than the characteristic time for change of T_e.

With the electron temperature equal to the ion temperature, the average plasma beta can be estimated

$$\beta_{\mathrm{vol}} = \frac{(n_i kT_i + n_e kT_e)V}{W_B}$$

where $V = 0.27$ m^{-3} is the volume of the spheromak with $R = 0.4$ m, and W_B is the total magnetic energy of the plasma. For SCAN23 and SCAN24 at t=0.3 msec, the total magnetic energies are 3.48 kJ and 10.2 kJ. The average plasma betas are 8.3% and 3.2% respectively. These low plasma beta values also confirm that the spheromak is close to Taylor's minimum energy state.

A bolometer was installed in one of the diagnostic ports at Z=12.7 cm to measure the line averaged impurity radiation power across the axis of the machine. Figure 6.18 shows the radiation energy density and the radiation power density for MS shot 5966. The radiation energy can be directly measured from the bolometer. The data is fitted to a curve (dotted line in the figure) and the radiation power is calculated from the fitted curve, knowing the response function of the bolometer. At t=0.3 msec, it shows that the line averaged radiated power ~ 1.25 kW/cm^{-3} across the axis of the plasma. If we take 50% of 1.25 kW/cm^{-3} to be the volume averaged radiated power, the total radiated power is then 169 MW for 0.27 m^{-3} plasma volume. The dissipation rate of magnetic energy is $W_B/\tau_W = 10.2\mathrm{kJ}/70\mu\mathrm{sec}$=146 MW. The radiation power measured accounts for all the magnetic energy dissipated within instrumental error. This indicates that the spheromak formed in MS is radiation dominated.

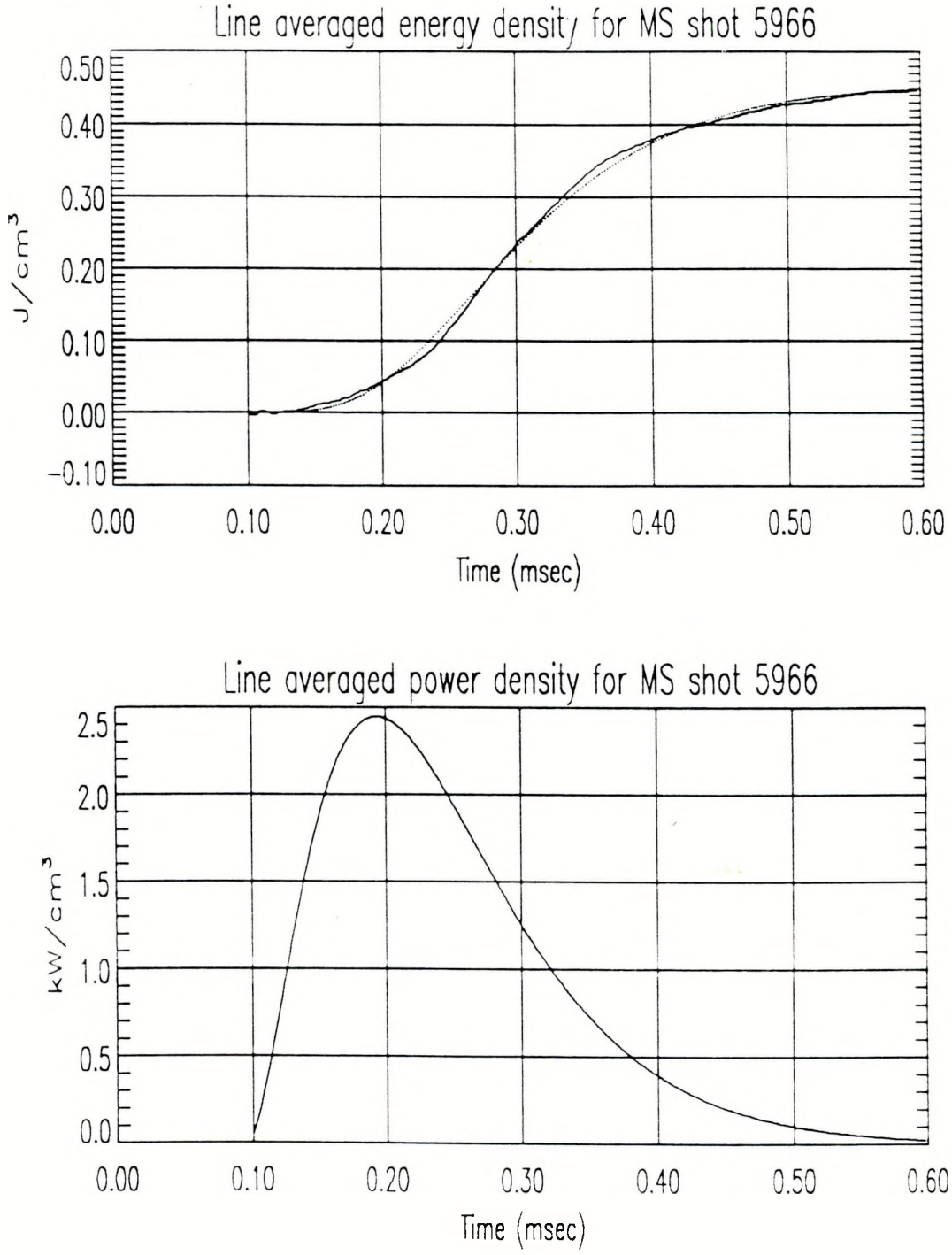

Figure 6.18: Line averaged radiation energy density and line averaged radiation power density for MS shot 5966. The solid line for radiation energy density is the raw data from the bolometer signal. The dotted line is the fitted curve. The radiation power density is calculated from the fitted curve.

Although a 10 kG high field spheromak is produced, the radiation loss causes the plasma average temperature to stay below 15 eV.

Chapter 7.
Grad-Shafranov Equilibrium Code

The MS spheromak is expected to be an axisymmetric configuration. The magnetic field structure of MS has been measured to be axisymmetric after the reversal coils were completely insulated to prevent any direct contact with the plasma. A numerical code first written by John Finn was modified to solve the Grad-Shafranov equation which describes the ideal MHD equilibrium magnetic field structure. Axisymmetric equilibrium states which can exist in the MS experiment are calculated using some assumptions about the plasma pressure and the poloidal current profiles. The numerical calculations are compared with the experimental measurements.

7.1. Numerical Code Description

The source terms of the Grad-Shafranov equation Eq. (2.24), which are the right hand side (RHS) of the equation, need to be specified in order to obtain the equilibrium state solution (RHS $= -2\pi r\mu_0 J_\phi$ is the toroidal current source). In the vacuum region RHS $= 0$ and in the plasma region RHS $= -(2\pi r)^2\mu_0 P' - \mu_0^2 I\, I'$. For $I(\Psi)$, the following form has been chosen

$$\mu_0^2 I^2(\Psi) = k^2\Psi^2\left(1 + \alpha\frac{2\Psi}{3\Psi_m}\right) \tag{7.1}$$

where Ψ_m is the poloidal flux at the magnetic axis, and α is a free parameter which allows a certain degree of control over the current distribution.

- $\alpha > 0$: the current density is more concentrated near the magnetic axis.
- $\alpha = 0$: the poloidal current is scaled linearly with the poloidal flux.
- $\alpha < 0$: the poloidal current has a flattened profile near the magnetic axis. A hollow current profile can be obtained with sufficiently negative α values.

For the pressure profile, the analytic form

$$\frac{\mathrm{d}P}{\mathrm{d}\Psi} = C_p(\Psi_m - \Psi) \tag{7.2}$$

is chosen so that $P' = 0$ at the magnetic axis. The constant C_p may be expressed in terms of the plasma beta at the magnetic axis. It is defined as

$$\beta_m \equiv \frac{P_m}{B_m^2/2\mu_0}$$

where P_m and B_m are the plasma pressure and the magnetic field at the magnetic axis respectively.

$$\begin{aligned}\beta_m &= \frac{2\mu_0 P_m}{\mu_0^2 I_m^2/(2\pi r_m)^2} \\ &= \frac{(2\pi r_m)^2 \mu_0 \Psi_m^2 C_p}{k^2 \Psi_m^2 \left(1+\frac{2}{3}\alpha\right)} \\ C_p &= \frac{k^2\left(1+\frac{2}{3}\alpha\right)\beta_m}{(2\pi r_m)^2 \mu_0} > 0 \end{aligned} \tag{7.3}$$

where r_m is the radius of the magnetic axis, I_m is the total poloidal current of the plasma.

The equation that needs to be solved has the following form

$$\begin{aligned}\triangle^*\Psi &= -k^2\left(\left(1+\alpha\frac{\Psi}{\Psi_m}\right)\Psi + \beta_m\left(1+\frac{2\alpha}{3}\right)\frac{r^2(\Psi_m-\Psi)}{r_m^2}\right) \\ &\qquad \ldots\ldots\ldots\ldots \text{for the plasma region} \\ &= 0. \qquad \ldots\ldots\ldots\ldots \text{for the vacuum region}\end{aligned}$$

The magnetic flux is chosen such that it is negative for the plasma region, and it is positive outside the separatrix (the vacuum region) in the code. The poloidal magnetic fluxes on the metal chamber walls were calculated from the bias current and treated as the boundary conditions. Fields from the plasma current are assumed not to penetrate the walls. In the code, the RHS was chosen according to the sign of the poloidal flux and the plasma boundary was then adjusted by the code. The free parameters are the total poloidal current of

the plasma I_m, the current profile factor α and the plasma beta at the magnetic axis β_m. This is an eigenvalue problem with k as the eigenvalue parameter. The simultaneous over-relaxation (SOR)[48] iteration method was used to solve the equation. At each iteration, k is evaluated as $\mu_0 I_m/(\Psi_m\sqrt{1+2\alpha/3})$. The iteration process continues until k and the equilibrium solution converge.

The equilibrium state was calculated with the bias coil current set at 100A (each bias coil has 600 turns). It should be noted that multiplying the bias coil current by a factor σ is equivalent to multiplying Ψ and I_m by σ, and does not affect k, α and β_m.

If the code is calculated with a parameter $\beta_m = 0$, a force-free equilibrium solution is obtained. If in addition α is set to zero then Taylor's minimum energy state is obtained ($\mathrm{d}I/\mathrm{d}\Psi = k$ is independent of position). The same code can be used to calculate the magnetostatic field. The vacuum poloidal flux due to the bias coil currents and the reversal coil currents in MS is obtained when all three parameters are set to zero ($I_m = \alpha = \beta_m = 0$). Within the reversal coil conductors, the externally supplied current density was used to calculate the RHS $= -2\pi r\mu_0 J_\phi$. The vacuum poloidal flux shown in Fig. 5.13 was calculated with the Grad-Shafranov code.

Numerical Formulas

The Grad-Shafranov equation was solved using the finite difference method in axisymmetric cylindrical coordinate system (r, z, ϕ), with ϕ an ignorable coordinate. We assumed reflection symmetry about the midplane $z = 0$ and the equation was solved in the region $z > 0$. The vessel was divided into an 81×81 equally spaced grid with spacing of 0.635 cm. The Grad-Shafranov equation was translated into the following numerical form

$$\left(\frac{2}{\triangle r^2} + \frac{2}{\triangle z^2}\right)\Psi_{i,j}$$
$$= \mathrm{RHS})_{i,j} - \left(\frac{\Psi_{i+1,j} + \Psi_{i-1,j}}{\triangle r^2} + \frac{\Psi_{i,j+1} - \Psi_{i,j-1}}{\triangle z^2} - \frac{\Psi_{i+1,j} - \Psi_{i-1,j}}{2r\triangle r}\right)$$

When the final equilibrium solution converges then the magnetic field is computed using

$$\begin{aligned} B_r &= -\frac{1}{2\pi r}\frac{\partial \Psi}{\partial z} \quad &\longrightarrow \frac{1}{2\pi r_i}\frac{\Psi_{i,j+1}-\Psi_{i,j-1}}{2\Delta z} \\ B_z &= \frac{1}{2\pi r}\frac{\partial \Psi}{\partial r} \quad &\longrightarrow \frac{1}{2\pi r_i}\frac{\Psi_{i+1,j}-\Psi_{i-1,j}}{2\Delta r} \\ B_\phi &= \frac{\mu_0 I}{2\pi r} \quad &\longrightarrow \frac{\mu_0 I_{i,j}}{2\pi r_i} \end{aligned} \tag{7.4}$$

However, at $r = 0$, the above formulas cannot be directly applied. Both B_r and B_ϕ are zero on the axis, so they did not become a problem. But B_z needs to be evaluated on the axis. The solution is to expand Ψ in terms of r.

$$\Psi(r) = a_0 + a_1 r + a_2 r^2 + a_3 r^3 + \cdots + a_n r^n .$$

Since $\Psi(0) = 0$, then $a_0 = 0$. The field B_z can be expressed as

$$B_z(r) = \frac{1}{2\pi}\left(\frac{a_1}{r} + 2\,a_2 + 3\,a_3 r + \cdots + n, a_n r^{n-1}\right).$$

Since B_z is finite on axis, $a_1 = 0$ and $B_z(0) = 2\,a_2$. At small radius, we can neglect higher order terms and choose $\Psi(r) = a_2\,r^2$. If $\Psi(\Delta) = a_2\Delta^2 = \Psi_1$, and $\Psi(2\Delta) = 4\,a_2\Delta^2 = \Psi_2$, then

$$B_z(0) = \frac{\Psi_2 - \Psi_1}{3\pi\Delta^2} \tag{7.5}$$

From knowledge of the magnetic field, the total magnetic energy of the plasma is then evaluated. The total magnetic helicity is calculated with Eq. (8.9).

7.2. Numerical Code Results

Equilibrium solutions for the Grad-Shafranov equation with the MS boundary conditions are discussed with various plasma conditions. The magnetic fields (B_z) measured on the midplane are then compared with the fields calculated from the code.

7.2.1 Equilibrium Solutions

The axisymmetric equilibrium solutions of Taylor's minimum energy state spheromak are shown in Fig. 7.1 for three different poloidal currents in the plasma. The diagrams shown on the left are the poloidal flux contours. The I_z electrode, reversal coil and parts of the chamber wall are also plotted as references. Contours in the plasma region are plotted as solid lines and those in the vacuum region are plotted as dotted lines. For the diagrams shown on the right, the solid curves are the B_z and B_ϕ fields on the midplane of the vessel as a function of radius (scale indicated on the left side of the diagram). The dotted curves are the poloidal flux on the midplane (scale indicated on the right side of the diagram)

For 100A (600 turn) bias coils current, the optimized solution appears to be the one with 80 kA of poloidal current in the plasma with the plasma separatrix just detached from the electrodes. For solutions with more than 80 kA of poloidal current, the plasma is intercepted by the electrodes and even in contact with the reversal coils. In those case, the electrodes and the reversal coils serve as heat sink, which will cool the plasma, and also bring in impurities when the plasma impact with those surfaces. Ideally, we would like to produce a plasma with as large current as possible (larger magnetic energy), and not in contact with any external material at the same time. This means that the bias coils current has to be increased proportionally when more plasma current is produced. We can then expect the bias coils current to scale with the main I_z current. From the experience of operating the MS machine, better magnetic profiles were obtained when the bias coils current scaled with the main I_z current and the reversal coils current. It scaled with the reversal coils current because the toroidal current of the plasma is induced from the decay of the the reversal current during the formation phase. For the spheromak, the toroidal current also scales with the poloidal current.

Figure 7.2 shows the plasma equilibrium solutions for 80 kA of poloidal current and different values of α and β. The top diagram shows equilibrium

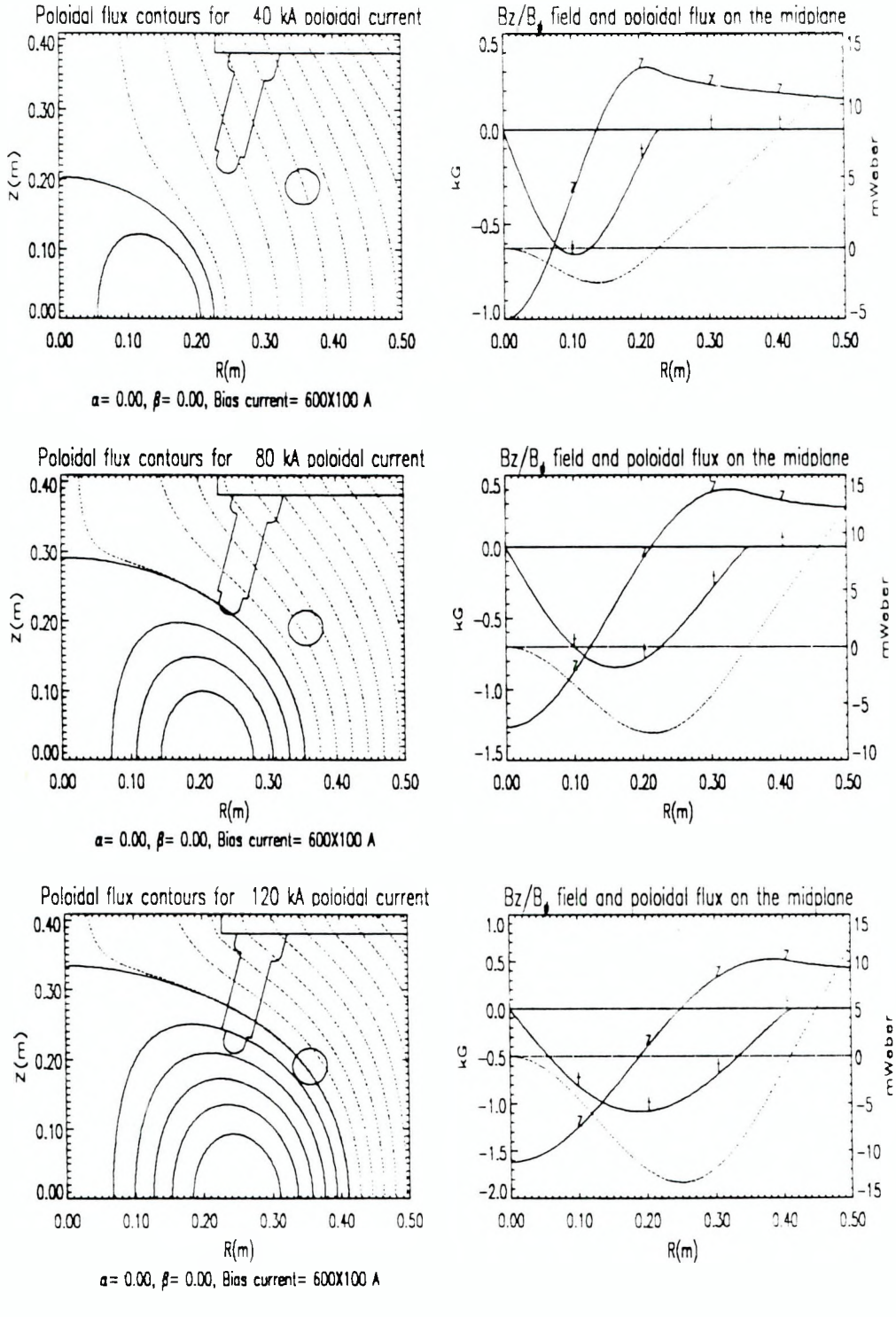

Figure 7.1: Equilibrium solutions of Taylor's minimum energy state spheromak are shown for three different total poloidal currents.

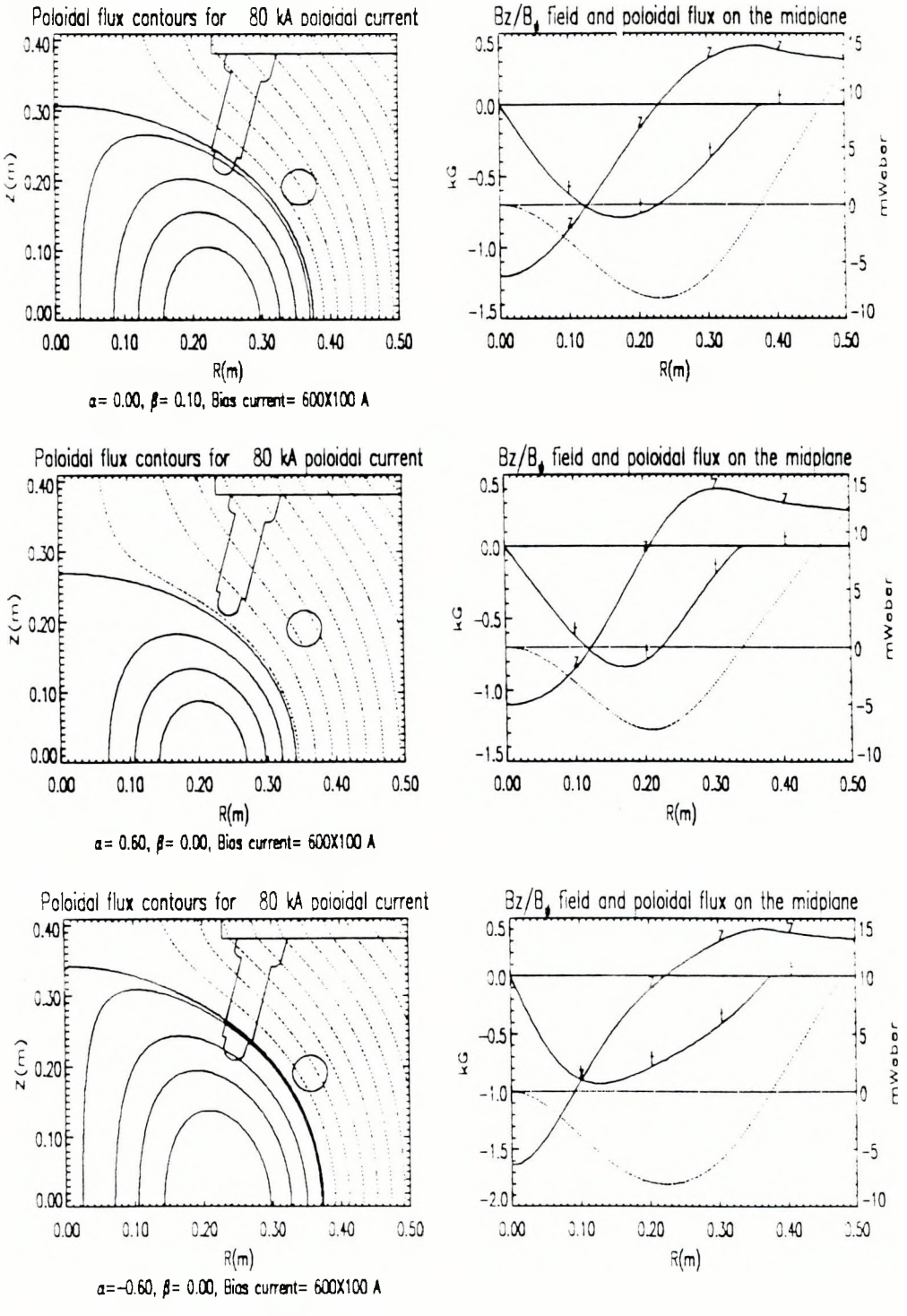

Figure 7.2: Equilibrium solutions for 80 kA poloidal plasma current for different α and β_m parameters.

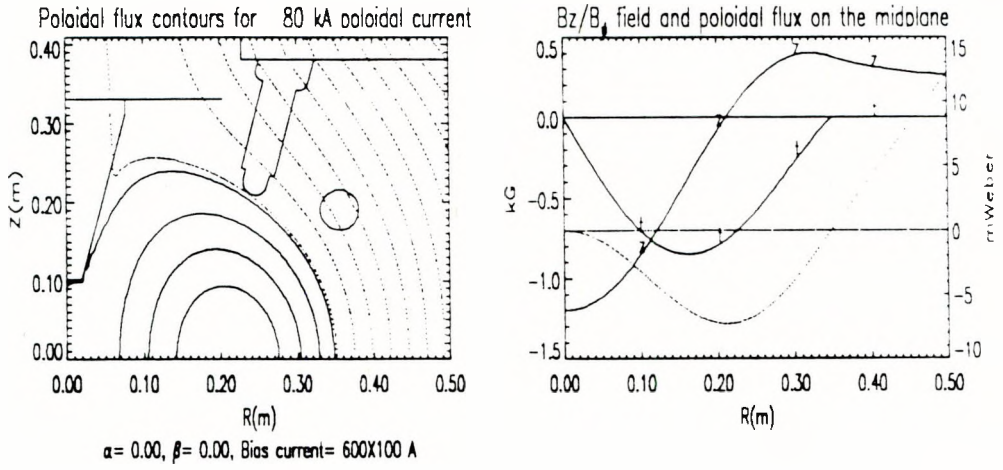

Figure 7.3: Equilibrium solutions for Taylor state plasma with the stabilizing cone on axis.

solutions for 10% plasma beta at the magnetic axis and $\alpha = 0$. The added plasma pressure effectively increases the toroidal current density in the plasma region. The plasma has a larger volume than obtained with the Taylor state plasma for the same total poloidal current. This is a manifestation of the well-known property of the toroidal plasma that the poloidal field contains the plasma pressure. The other two diagrams show solutions for $\alpha = \pm 0.6$ and $\beta_m = 0$. For the case with $\alpha = 0.6$, the plasma current is more concentrated near the magnetic axis which effectively reduces the field on axis (B_z field changes from 1.27 kG $\rightarrow$ 1.11 kG when compared with Taylor state for the same poloidal current). In the case where $\alpha = -0.6$, the poloidal current has a flattened profile near the magnetic axis, and the B_ϕ field peaks closer to the axis. A hollow current profile can be obtained with more negative α value.

Stabilizing cones were installed in the vessel to stabilize the shift and tilt motion of the plasma. To understand the effects of the cone on the equilibrium state, additional constraints were added in the code to simulate the cones. The cone was treated as a perfectly conducting material with bias flux embedded in it. Figure 7.3 shows the Taylor state with the stabilizing cone on axis. The location and the size of the cone are exactly the same as the aluminum

cones used in MS. Although the flux surfaces near the cones are changed, the magnetic fields and the fluxes on the midplane are almost identical to the case without cones. On the midplane, the only noticeable difference is that the B_z field near the axis is slightly reduced in magnitude.

Figures 7.4(a-e) show the dependence of various plasma properties on the total poloidal current I_m in the plasma for three different sets of parameters (α, β_m). Figure 7.4(a) shows the maximum poloidal flux of the plasma as a function of I_m. Figure 7.4(b) shows how the separatrix radius at the midplane of the plasma varies with the plasma current. The largest separatrix radius is limited by the chamber size, since the field was assumed not to penetrate the walls. For plasma with current I_m larger than about 100 kA, the separatrix radius does not increase much when I_m is increased. However, when I_m drops below about 50 kA, the separatrix radius of the spheromak changes rapidly with I_m. The slope in Fig. 7.4(a) is $1/k$, which gives indications about the size of the plasma for a given I_m. The slope is small for plasma with I_m less than 50 kA and roughly approaches a constant value for I_m larger than 100 kA. The two diagrams therefore show a consistent result.

Figure 7.4(c-e) show the magnetic field at the plasma center, the total magnetic helicity and the total magnetic energy as a function of plasma current. For the Taylor minimum energy state, the total poloidal energy is equal to the total toroidal energy (shown in Fig. 7.4(f) as solid line). This can be shown as

$$\begin{aligned} W_p &= \frac{1}{2\mu_0}\int \vec{B}_p^2\,d\tau \\ &= \frac{1}{2\mu_0}\int \vec{B}_p\cdot\nabla\times\vec{A}_\phi\,d\tau \\ &= \frac{1}{2\mu_0}\int \left(\nabla\cdot\left(\vec{A}_\phi\times\vec{B}_p\right)+\vec{A}_\phi\cdot\nabla\times\vec{B}_p\right)d\tau \\ &= \frac{1}{2\mu_0}\int_s \vec{A}_\phi\times\vec{B}_p\cdot d\vec{S}+\frac{1}{2}\int \vec{A}_\phi\cdot\vec{J}_\phi\,d\tau \\ &= \frac{1}{2\mu_0}\int \vec{B}_\phi^2\,d\tau \\ &= W_\phi \end{aligned} \tag{7.6}$$

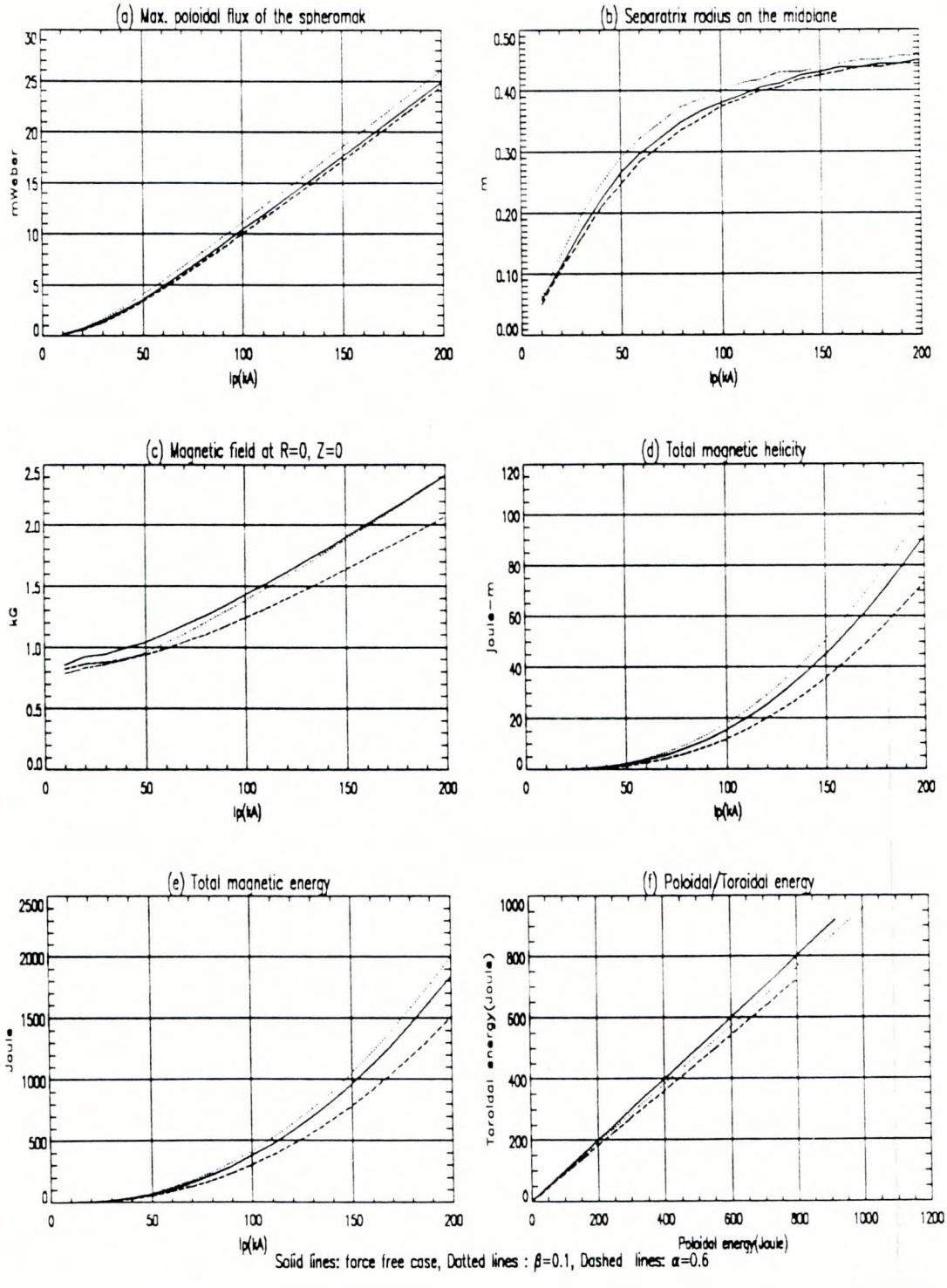

Figure 7.4: Maximum poloidal flux, separatrix radius, total magnetic energy, total magnetic helicity and B_z field at the center of the plasma, as a function of plasma current are shown for three different cases. (1)Solid lines represent the Taylor state, $\alpha = \beta_m = 0$ (2)Dotted lines represent plasma with $\alpha = 0, \beta_m = 0.1$ (3)Dashed lines represent plasma with $\alpha = 0.6, \beta_m = 0$.

where $\mu_0\vec{J}_\phi = k\vec{B}_\phi = k^2\vec{A}_\phi$, W_p and W_ϕ are the total poloidal energy and the total toroidal energy, respectively. The above surface integral vanishes because it contains $A_\phi = \Psi/(2\pi r)$, which is zero on the plasma boundary.

For the case with $\alpha = 0$ ($\mu_0 I_p = k\Psi$ — $\vec{B}_\phi = k\vec{A}_\phi$) and finite plasma pressure ($\vec{J}_\phi = k\vec{B}_\phi/\mu_0 + 2\pi r P'$)

$$W_p = W_t + \frac{1}{2}\int \Psi \frac{\mathrm{d}P}{\mathrm{d}\Psi}\,\mathrm{d}\tau \tag{7.7}$$

The dotted curve in Fig. 7.4(f) shows that the poloidal energy is larger than the toroidal energy for the equilibrium solution with $\beta_m = 0.1$. This can be explained from Eqs. (7.2) and (7.3),

$$\Psi\frac{\mathrm{d}P}{\mathrm{d}\Psi} = C_p\Psi(\Psi_m - \Psi) > 0.$$

The integral is positive, so the total poloidal energy is larger than the total toroidal energy for the assumed pressure profile. A similar result is shown for the solution with $\alpha = 0.6$ and $\beta_m = 0$.

7.2.2 Comparison with Measurements

The equilibrium solutions for 100A bias coil current have been calculated with different poloidal current I_m, α and β_m values. The solutions are stored into separate files. Each file contains solutions with the same values of α and β_m but different poloidal currents. For axisymmetric plasma, the poloidal current profile can be obtained from the B_ϕ fields measured on the midplane. The total poloidal current of the spheromak, which is also the maximum poloidal current on the midplane, can be calculated as a function of time from the probe measurements. From knowledge of the total poloidal current, the B_z field on the midplane can be calculated from the equilibrium solution, with α and β_m as fitting parameters.

Figure 7.5 shows the B_z field at six radii on the midplane of the vessel (solid lines) and the calculated B_z fields (dotted lines between t=0.25-0.35 msec) for MS shot 4150. The fields are first fitted with the Taylor minimum

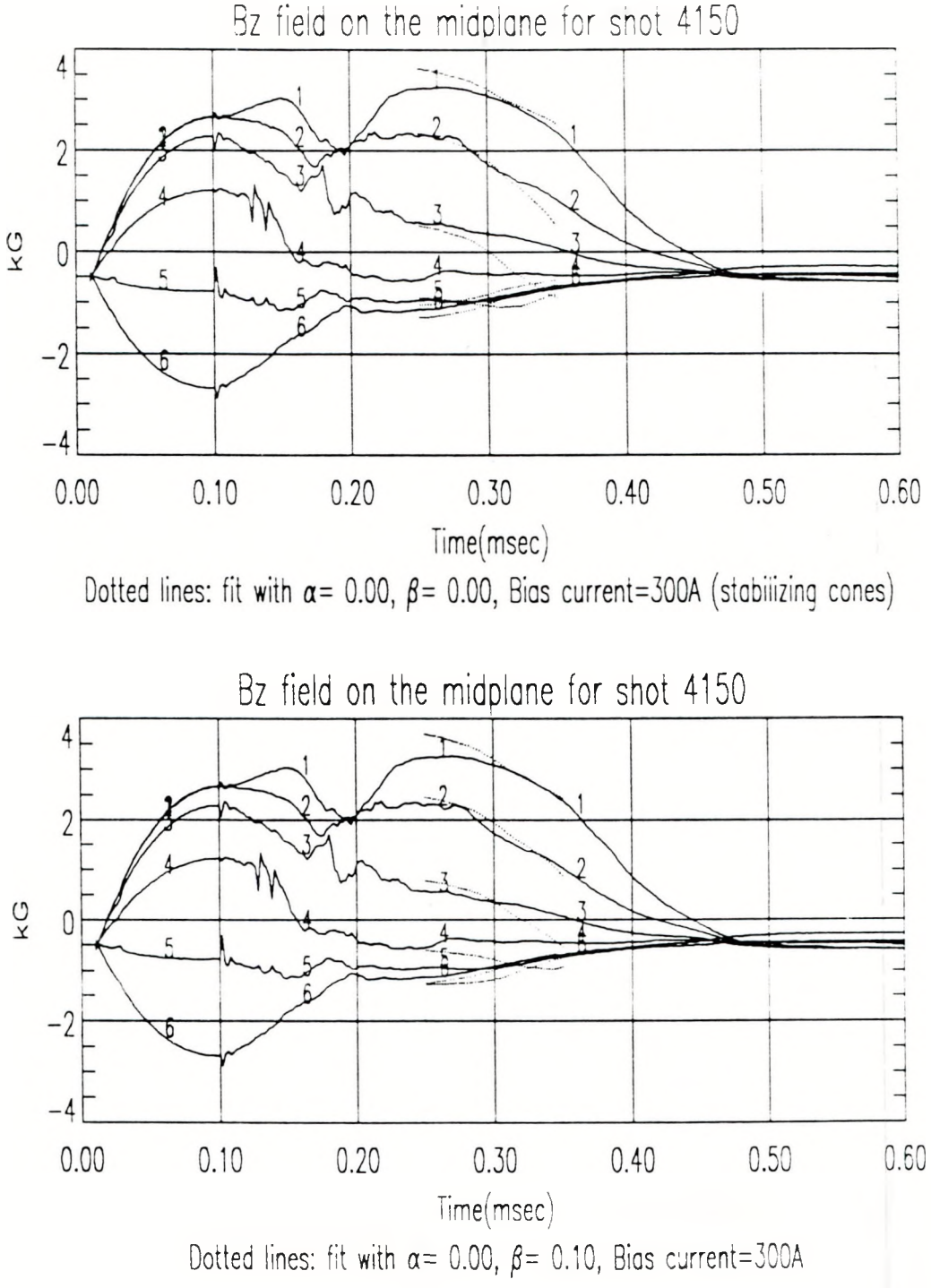

Figure 7.5: B_z fields on the midplane fitted with the Taylor state and plasma beta β_m=0.1 at the magnetic axis. The total poloidal current used is calculated from the B_ϕ field measurements.

energy state plasma (with the stabilizing cone). Between t=0.25-0.30 msec, the fitted data show good agreement with the measured fields. This indicates that the plasma produced was close to the Taylor minimum energy states (the same sets of data were also compared with the classical spheromak and shown in Fig. 5.9). When fitted with 10% plasma beta at the magnetic axis, better agreement between calculated fields and measured values was obtained between t=0.30-0.35 msec. The bias current used for shot 4150 is 300 A. The magnetic fields calculated from the solution are all multiplied by a factor of 3 to get the fitted data.

Figure 7.6 shows the B_z fields on the midplane for MS shots 5435 and 5493. The data were taken after the I_z current path between the reversal coil and the vacuum chamber wall was blocked by the two glass plates. All the I_z current was flowing in the central region of the vessel, and the B_z fields show much higher values than fields for shot 4150. These fields are fitted to the solution with $\alpha = -0.6, \beta = 0.1$, and good agreement was obtained between t=0.25-0.40 msec. The close fit between the data measured and the fields calculated from the Grad-Shafranov code solutions indicates that the plasma produced in MS stays very close to the equilibrium state after the spheromak is formed.

For MS shot 5435, between t=0.25-0.35 msec, the magnetic axis appears to be located at a fixed position (in the middle of coils #4 and #5). The fitted curves show that the magnetic axis is located between coils #4 and #5 during the same period. However, the calculated fields also indicates that the magnetic axis continuous moving toward the axis as the poloidal current decreases, and it become located at the coil #4 position at t=0.35 msec. This is the reason that the fitted data of coils near the magnetic axis deviate more from the measured field. The deviations between the measured fields and calculated fields could be due to some I_z current still flowing in the vessel after the spheromak was formed (as shown in Fig. 3.3). In the code, it is assumed that there is no external current source other than the plasma current.

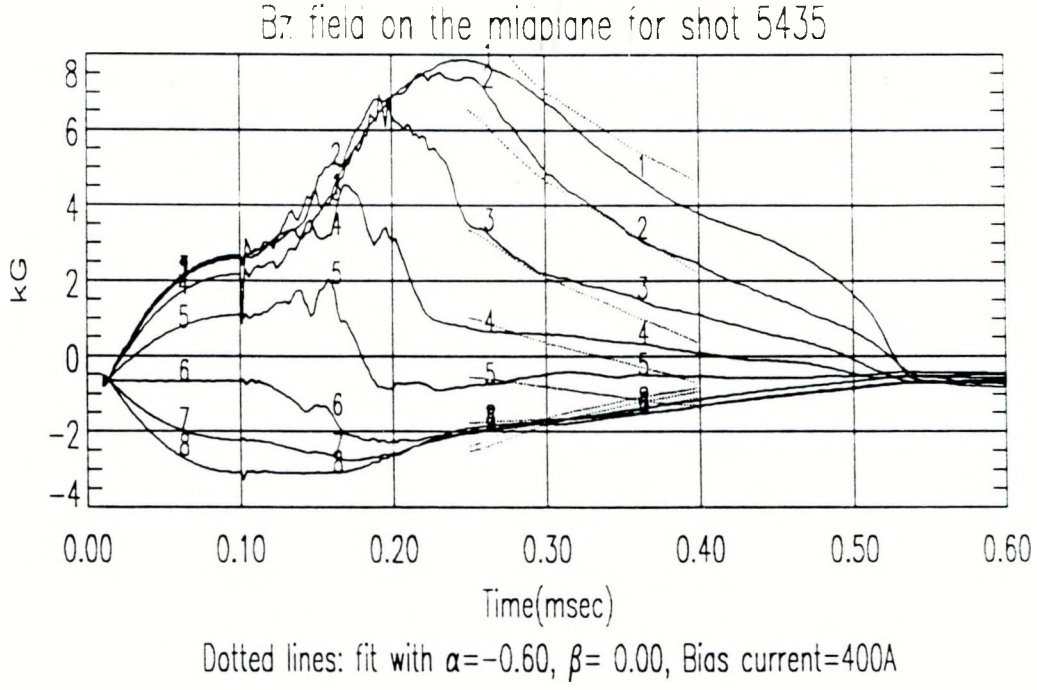

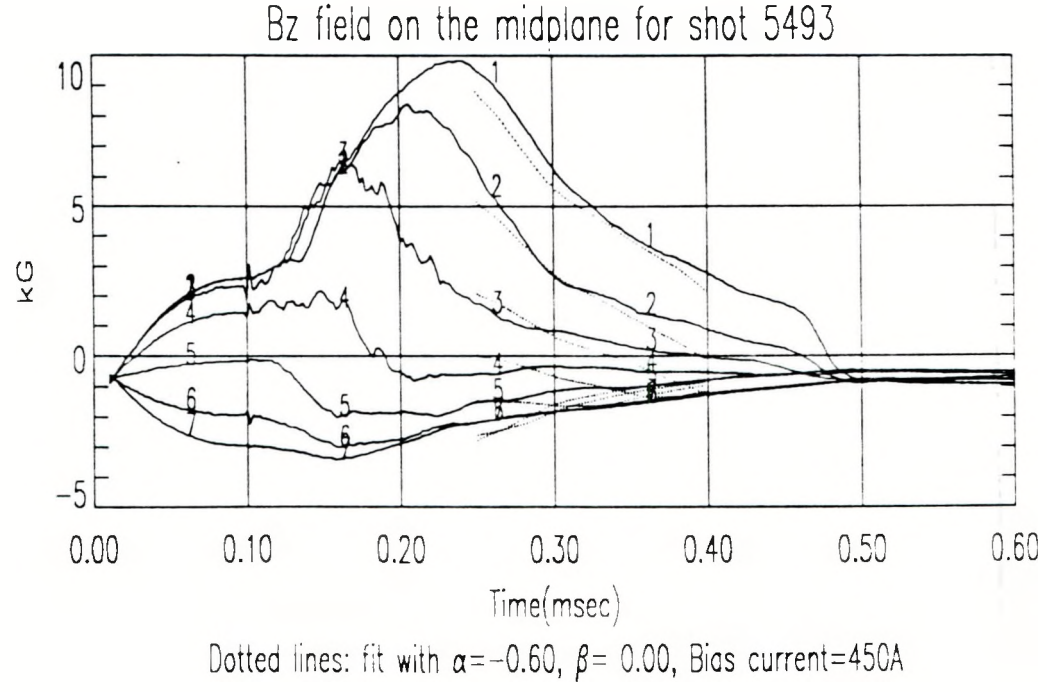

Figure 7.6: B_z fields on the midplane for MS shots 5435 and 5493. (fitted to equilibrium solution with $\alpha = -0.6, \beta_m = 0.1$). The total poloidal currents used are calculated from the B_ϕ field measurements.

Chapter 8.
Magnetic Helicity

The magnetic field is a divergence-free vector field. Moffatt[34] has shown that the pseudoscalar "**magnetic helicity**" is a measure of the linkage of the magnetic field lines inside a magnetic surface. Magnetic helicity is defined by the volume integral

$$H \equiv \int_{\tau} \vec{A} \cdot \vec{B} \, d\tau. \tag{8.1}$$

where $\vec{B} = \nabla \times \vec{A}$. Magnetic helicity has been recognized as a global invariant quantity for a high conductivity plasma during the relaxation process. For a slightly resistive turbulent plasma, this leads to Taylor's force-free equilibrium.[33] The magnetic helicity of the spheromak is determined by the helicity injected during the formation phase. How to effectively inject magnetic helicity in the plasma becomes an important issue. An important application is that the plasma can be sustained against resistive decay by injecting helicity into the plasma volume.

Magnetic helicity is well defined by Eq. (8.1) only if the boundary is a closed flux surface. This is demonstrated by the following gauge transformation: let $\vec{A} \rightarrow \vec{A} + \nabla\chi$, then $H \rightarrow H + \delta H$ and

$$\delta H = \int_{\tau} \nabla\chi \cdot \vec{B} \, d\tau = \int_{s} \chi \vec{B} \cdot \hat{n} \, dS.$$

The above integration vanishes only when the boundary is a magnetic surface.

8.1. Generalized Magnetic Helicity

The gauge problem has been studied by a number of workers. Three generalized magnetic helicities have been defined in the literature.[27,49–50] The definition proposed by Finn and Antonsen[50] turns out to be the most general form.

Berger and Field[27] define the relative helicity for an open field line system as

$$H_{BF} \equiv \int_{\tau_a+\tau_b} \left(\vec{A} \cdot \vec{B} - \vec{A}' \cdot \vec{B}' \right) \, d\tau, \tag{8.2}$$

where $\vec{B}$ and $\vec{B}'$ are two magnetic fields which are different in some region of space, τ_a, typically the volume of interest, and are the same in the rest of space, τ_b. The vector potentials $\vec{A}$ and $\vec{A}'$ are vector potentials which generate $\vec{B}$ and $\vec{B}'$. To ensure $\nabla \cdot B = 0$, it is required that

$$\vec{B} \cdot \hat{n} = \vec{B}' \cdot \hat{n} \tag{8.3}$$

on the boundary between τ_a and τ_b, where $\hat{n}$ is the normal vector pointing away from volume τ_a. Berger and Field also have shown that the relative helicity is independent of the common extension into τ_b.

In region τ_b, the magnetic fields $\vec{B}$ and $\vec{B}'$ are the same, therefore, $\vec{A}' = \vec{A} + \nabla\chi$. The integration in Eq. (8.2) for region τ_b is

$$\int_{\tau_b} \left(\vec{A} \cdot \vec{B} - \vec{A}' \cdot \vec{B}' \right) \, d\tau = \int_{\tau_b} \nabla\chi \cdot \vec{B}' \, d\tau = \int_{s_b} \chi \vec{B}' \cdot \hat{n} \, dS$$

If χ is a constant on the boundary, then the contribution from τ_b vanishes. This leads to the definition proposed by Jensen and Chu.[49]

$$H_{JC} \equiv \int_{\tau} \left(\vec{A} \cdot \vec{B} - \vec{A}' \cdot \vec{B}' \right) \, d\tau. \tag{8.4}$$

Only the region of interest needs to be integrated over, with the condition that the tangential components of the vector potentials $\vec{A}$ and $\vec{A}'$ are the same on the surface of the volume.

Finn and Antonsen[50] noticed that Eq. (8.2) is not invariant if different gauges are used in τ_a and τ_b. For $\vec{A} \to \vec{A} + \nabla\chi$, $\vec{A}' \to \vec{A}' + \nabla\chi'$, the difference

is

$$\int_{\tau_a+\tau_b} \left(\nabla\lambda\cdot\vec{B}-\nabla\lambda'\cdot\vec{B}'\right)\,d\tau=\int_{s_a}\left(\lambda_{in}-\lambda_{out}-\lambda'_{in}+\lambda'_{out}\right)\vec{B}\cdot\hat{n}\,dS.$$

Therefore, gauge invariance can be guaranteed if $\lambda_{in}-\lambda_{out}=\lambda'_{in}-\lambda'_{out}$ on the boundary. This is less restrictive than the boundary condition required by Jensen and Chu.

A more generalized helicity is then proposed by Finn and Antonsen as

$$H_{FA}\equiv\int_\tau\left(\vec{A}+\vec{A}'\right)\cdot\left(\vec{B}-\vec{B}'\right)\,d\tau, \tag{8.5}$$

This definition has the advantage of requiring integration only over the region of interest and also allows different gauge transformations for $\vec{A}$ and $\vec{A}'$.

$$\begin{aligned}H_{FA}&=\int_\tau\left(\vec{A}\cdot\vec{B}-\vec{A}'\cdot\vec{B}'\right)\,d\tau+\int_\tau\left(\vec{A}'\cdot\vec{B}-\vec{A}\cdot\vec{B}'\right)\,d\tau\\&=H_{JC}+\int_s\left(\vec{A}\times\vec{A}'\right)\cdot\hat{n}\,dS\end{aligned}$$

If $\vec{A}=\vec{A}'$ on the boundary then the surface term vanishes, and H_{FA} is equivalent to H_{JC}. All three definitions Eqs. (8.2),(8.4) and (8.5) for generalized magnetic helicity basically are the same if the tangential component of the vector potential is continuous on the boundary.

The definition proposed by Berger and Field requires the same gauge transformation over all spaces and it also requires integration over all spaces. The definition proposed by Jensen and Chu has the advantage of only involving integration over the region of interest but requires the tangential component of the vector potential to be continuous on the boundary. Finn and Antonsen solved the gauge problem, and their definition only involves integration over the volume of interest. The definition proposed by Finn and Antonsen is adopted for this study.

From Eq. (8.5), the time rate of change of the magnetic helicity can be expressed as[50]

$$\frac{dH}{dt}=-2\int_\tau\left(\vec{E}\cdot\vec{B}-\vec{E}'\cdot\vec{B}'\right)\,d\tau+\int_s\left(\vec{A}+\vec{A}'\right)\times\left(\vec{E}-\vec{E}'\right)\cdot\hat{n}\,dS \tag{8.6}$$

for a fixed boundary volume. Finn and Antonsen have shown that $\vec{E}'$ can be any vector satisfying $\nabla \times \vec{E}' = -\partial \vec{B}'/\partial t$ in all space. It is usually chosen to be a vacuum field, $\nabla \cdot \vec{E}' = 0$.

8.2. Axisymmetric Systems

For practical purpose, most of the magnetic confinement devices being investigated have an axisymmetric boundary configuration. The vector field can be divided into a toroidal component and a poloidal component, with $\hat{\phi}$ the symmetry angle (toroidal) and,

$$\vec{B} = \vec{B}_p + \vec{B}_\phi, \qquad \vec{B}_p \cdot \vec{B}_\phi = 0.$$
$$\vec{B}_p = \nabla \times \vec{A}_\phi, \qquad \vec{B}_\phi = \nabla \times \vec{A}_p.$$

In such a case, from Eq. (8.5),

$$H = \int_\tau \left(\vec{A}_p + \vec{A}'_p\right) \cdot \left(\vec{B}_p - \vec{B}'_p\right)\, d\tau + \int_\tau \left(\vec{A}_\phi + \vec{A}'_\phi\right) \cdot \left(\vec{B}_\phi - \vec{B}'_\phi\right)\, d\tau.$$

The first term on the right hand side can be expressed as

$$\begin{aligned}
&\int_\tau \left(\vec{A}_p + \vec{A}'_p\right) \cdot \left(\vec{B}_p - \vec{B}'_p\right)\, d\tau \\
&= \int_\tau \left(\vec{A}_p + \vec{A}'_p\right) \cdot \nabla \times \left(\vec{A}_\phi - \vec{A}'_\phi\right)\, d\tau \\
&= \int_\tau \left(\vec{A}_\phi - \vec{A}'_\phi\right) \cdot \nabla \times \left(\vec{A}_p + \vec{A}'_p\right)\, d\tau - \int_\tau \nabla \cdot \left[\left(\vec{A}_p + \vec{A}'_p\right) \times \left(\vec{A}_\phi - \vec{A}'_\phi\right)\right]\, d\tau \\
&= \int_\tau \left(\vec{A}_\phi - \vec{A}'_\phi\right) \cdot \left(\vec{B}_\phi + \vec{B}'_\phi\right)\, d\tau - \int_s \left(\vec{A}_p + \vec{A}'_p\right) \times \left(\vec{A}_\phi - \vec{A}'_\phi\right) \cdot \hat{n}\, dS
\end{aligned}$$

From Eq. (8.3), the toroidal components of the vector potentials are only different by a gradient field which is an effect of the gauge transformation.

For an axisymmetric system $\vec{A}_\phi = \vec{A}'_\phi$ on the boundary. The helicity can be simplified as

$$\begin{aligned}
H_{rel} &= \int_\tau \left[\left(\vec{A}_\phi + \vec{A}'_\phi\right) \cdot \left(\vec{B}_\phi - \vec{B}'_\phi\right) - \left(\vec{A}_\phi - \vec{A}'_\phi\right) \cdot \left(\vec{B}_\phi + \vec{B}'_\phi\right)\right]\, d\tau \\
&= 2 \int_\tau \left(\vec{A}_\phi \cdot \vec{B}_\phi - \vec{A}'_\phi \cdot \vec{B}'_\phi\right)\, d\tau \qquad (8.7) \\
&= 2 \int_\tau \left(\Psi_p B_\phi - \Psi'_p B'_\phi\right)\, dr\, dz \qquad (8.8)
\end{aligned}$$

where $\Psi_p = 2\pi r A_\phi$ is the poloidal flux. For a simply connected volume as in the case of MS, $\vec{B}'_\phi = 0$.

$$H_{rel} = 2\int_\tau \vec{A}_\phi \cdot \vec{B}_\phi \, d\tau = 2\int_\tau \Psi_p B_\phi \, dr\, dz \tag{8.9}$$

The magnetic helicity for two untwisted closed flux tubes linked once is $\pm 2\Phi\Psi$, where Φ and Ψ are the magnetic fluxes of the tubes. Eq. (8.9) gives the same result as calculated by Eq. (8.1) when the boundary is a flux surface. The difference between Eqs. (8.9) and (8.1) can be calculated

$$\begin{aligned} H &= \int_\tau \left(\vec{A}_\phi \cdot \vec{B}_\phi + \vec{A}_p \cdot \vec{B}_p\right) d\tau \\ \vec{A}_p \cdot \vec{B}_p &= \vec{A}_p \cdot \nabla \times \vec{A}_\phi \\ &= \nabla \cdot \left(\vec{A}_\phi \times \vec{A}_p\right) + \vec{A}_\phi \cdot \nabla \times \vec{A}_p \\ H - H_{rel} &= \int_s \vec{A}_\phi \times \vec{A}_p \cdot \hat{n}\, dS \\ &= \oint \Psi \vec{A}_p \cdot d\vec{\ell} \end{aligned} \tag{8.10}$$

It is $\vec{A}_p$ which causes the gauge problem, and this term disappears with the new definition Eq. (8.9). For a simply connected volume with constant flux boundary, Eq. (8.10) gives $\Psi \oint \vec{A}_p \cdot d\vec{\ell} = 0$, therefore, the two definitions are equivalent.

From Eq. (8.9) and $\vec{E}_\phi = -\partial \vec{A}_\phi / \partial t$ inside the boundary, the derivative of the helicity can be calculated as

$$\begin{aligned} \frac{d}{dt} 2\int_\tau \vec{A}_\phi \cdot \vec{B}_\phi \, d\tau &= 2\int_\tau \left(\frac{\partial \vec{A}_\phi}{\partial t} \cdot \vec{B}_\phi + \vec{A}_\phi \cdot \frac{\partial \vec{B}_\phi}{\partial t}\right) d\tau \\ &= 2\int_\tau \left(-\vec{E}_\phi \cdot \vec{B}_\phi - \vec{A}_\phi \cdot \nabla \times \vec{E}_p\right) d\tau \\ &= -2\int_\tau \vec{E}_\phi \cdot \vec{B}_\phi \, d\tau - 2\int_\tau \left(\nabla \cdot \left(\vec{E}_p \times \vec{A}_\phi\right) + \vec{E}_p \cdot \nabla \times \vec{A}_\phi\right) d\tau \\ &= -2\int_\tau \vec{E} \cdot \vec{B}\, d\tau - 2\int_s \vec{E}_p \times \vec{A}_\phi \cdot \hat{n}\, dS \end{aligned} \tag{8.11}$$

For a non-ideal plasma, assuming linear Ohm's law $\vec{E} = \eta \vec{J} + \vec{V} \times \vec{B}$,

$$\frac{dH}{dt} = -2\int_\tau \eta \vec{J} \cdot \vec{B}\, d\tau - 2\int_s \vec{E}_p \times \vec{A}_\phi \cdot \hat{n}\, dS. \tag{8.12}$$

The volume integration represents the helicity dissipation rate due to finite resistivity. The surface integration represents the helicity injected from the boundary.

$$\begin{aligned} -2\int_s \vec{E}_p \times \vec{A}_o \cdot \hat{n}\, dS &= -2\oint \Psi_p \left(\vec{E}_p \cdot d\vec{\ell}_p\right) \\ &= -2\int_s \left(\Phi \vec{B}_p - \frac{\partial \vec{A}_p}{\partial t} \times \vec{A}_o\right) \cdot \hat{n}\, dS \\ &= -2\int_s \Phi \vec{B}_p \cdot \hat{n}\, dS \end{aligned} \tag{8.13}$$

where the loop integration is carried out along the poloidal boundary and $\vec{E}_p = -\nabla\Phi - \frac{\partial \vec{A}_p}{\partial t}$. The second term in the surface integral vanishes for axisymmetric configurations.

8.3. Helicity Balance

For simplicity, a constant factor $2\mu_0$ has been neglected in the above discussion of this chapter. From Eq. (8.9), the magnetic helicity in MS is evaluated as

$$H = \frac{2}{2\mu_0}\int \Psi B_\phi\, dr\, dz \tag{8.14}$$

All the quantities are in MKS units. The poloidal flux Ψ is calculated from the B_z measurements, and B_ϕ is obtained directly from the probe signals. The magnetic field was not measured inside the entire MS main chamber, but only in the region between the tips of the I_z electrodes (shown in Fig. 4.1). However, this is the region where the spheromak is formed. The helicity calculated in this region should represent most of the helicity of the spheromak.

From Eq. (8.13), the helicity injection rate is calculated using

$$\dot{H}_{inj}(t) = \frac{2}{2\mu_0} V(t)\, \Psi_{boundary}(t) \tag{8.15}$$

where $V(t)$ is the voltage measured between the anode and the cathode of the I_z electrodes with a voltage divider, and $\Psi_{boundary}(t) = -\int \vec{B}\cdot\hat{n}\, dS$ is the total

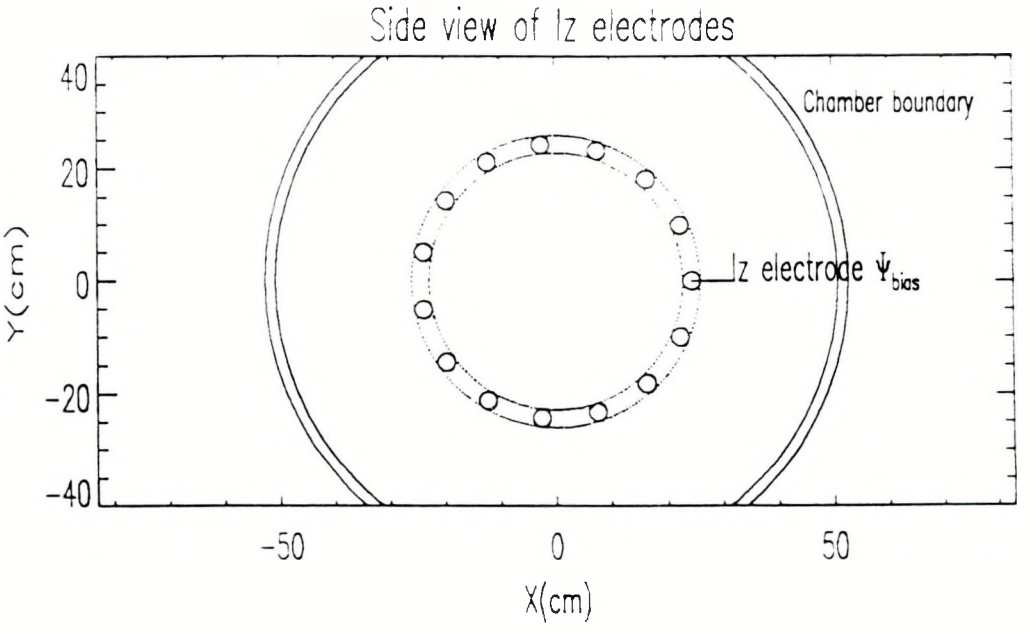

Figure 8.1: Side view of the I_z electrodes. The total poloidal flux inside the two dotted circles is used as $\Psi_{boundary}$ for helicity injection rate calculation.

poloidal flux that enters the area of the voltage sources on the boundary. The helicity injected into the system is

$$H_{inj} = \int_0^t \dot{H}_{inj}\,(t')\;\mathrm{d}t' = \frac{1}{\mu_0}\int_0^t V\,(t')\;\Psi_{boundary}\,(t')\;\mathrm{d}t' \qquad (8.16)$$

On the time scale of the experiment, only the field produced by the bias coil current can penetrate the electrodes and become embedded in them. It turns out that if only the bias flux Ψ_{bias} is used for $\Psi_{boundary}$, the injected helicity calculated from Eq. (8.16) is not only too small to account for the helicity evaluated from Eq. (8.14), but has the wrong sign.

If the total poloidal flux Ψ_{total} in an annular ring containing the I_z electrodes (dotted circles in Fig. 8.1) is used for $\Psi_{boundary}$, then the injected helicity calculated with Eq. (8.16) is close to the helicity measured for SCAN24. The space between the I_z electrodes appears to be acting like a virtual voltage source. The total flux Ψ_{total} is calculated as follows: In the area of the I_z electrodes (small solid circles), the flux produced from the bias coil current Ψ_{bias}

is used for $\Psi_{boundary}$. In the area between the two dotted circles and outside the area of the electrodes, the flux calculated from the probe measurement is used for $\Psi_{boundary}$.

In the area between the electrodes, the magnetic field signal is similar to the reversal current waveform between t=0.1-0.2 msec. This is because the tips of the I_z electrodes are close to the reversal coils and most of the poloidal field inside the chamber is produced by the two reversal coils during the same period. The flux produced by the reversal coil current is much larger than the bias flux in the area between the electrodes, and a positive helicity is obtained.

Figure 8.2 shows the measured I_z voltage for SCAN23 and SCAN24 plasma discharges. The voltages for two different plasma shots are shown for each scan. The I_z capacitor banks are charged at 13kV and 12kV for SCAN23 and SCAN24 respectively. Between SCAN23 and SCAN24, the I_z capacitor bank has been upgraded from 2.88 mF to 5.76 mF. This is the reason that more I_z current discharged in SCAN24 (shown in Fig. 6.1) even though the capacitor bank is charged at lower voltage. The digitizer is operated at 2 μsec clock rate, so the transient full voltage is not seen in the figure. When a 10 MHz digitizer is used, twice the charge voltage of the bank is observed briefly, due to the transient reflection of the signal in the transmission lines.

The magnetic helicity of the plasma is shown in Fig. 8.3 for SCAN23 and SCAN24. The magnetic helicity calculated with Eqs. (8.14) is plotted with solid curves. The dotted and dashed curves are injected helicity calculated from the I_z voltage measured from two different plasma shots. For SCAN23, the I_z voltage used in Eqs. (8.15) is the voltage of shot 4565 and 4663. The difference between the dotted curves and the dashed curves reflects the uncertainty of the calculated values. Most of the errors are come from the I_z voltage measurements. There are more fluctuations in the voltage measurements in the first 30 μsec after the I_z is triggered. The total poloidal flux near the tips of the electrodes is mostly generated from the reversal coil current. When I_z is triggered, the reversal current is at its peak value, and the helicity injection

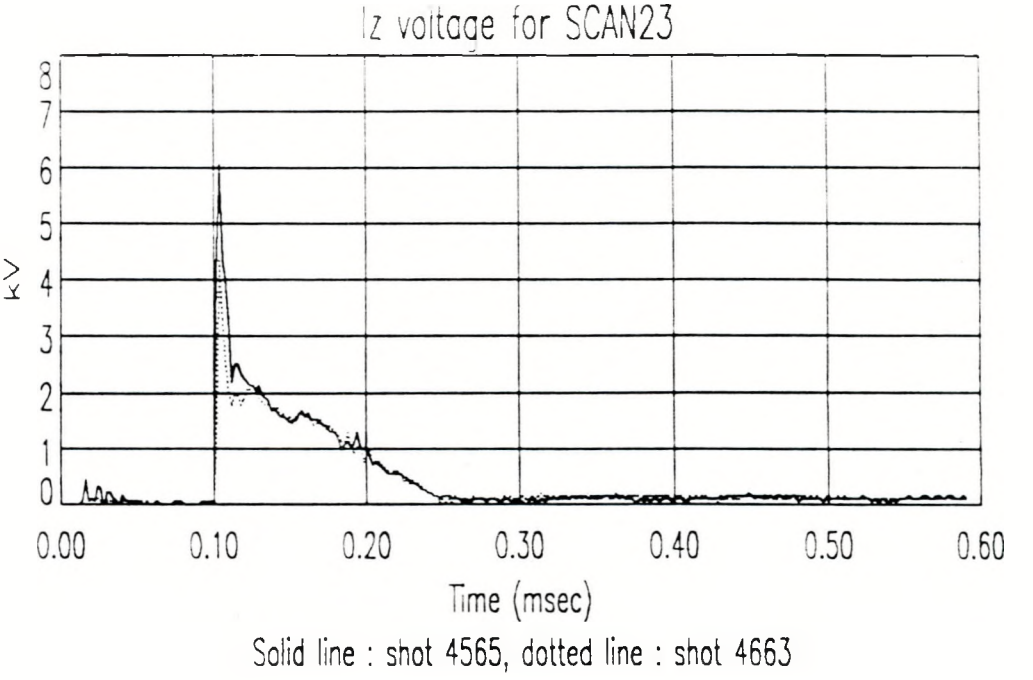

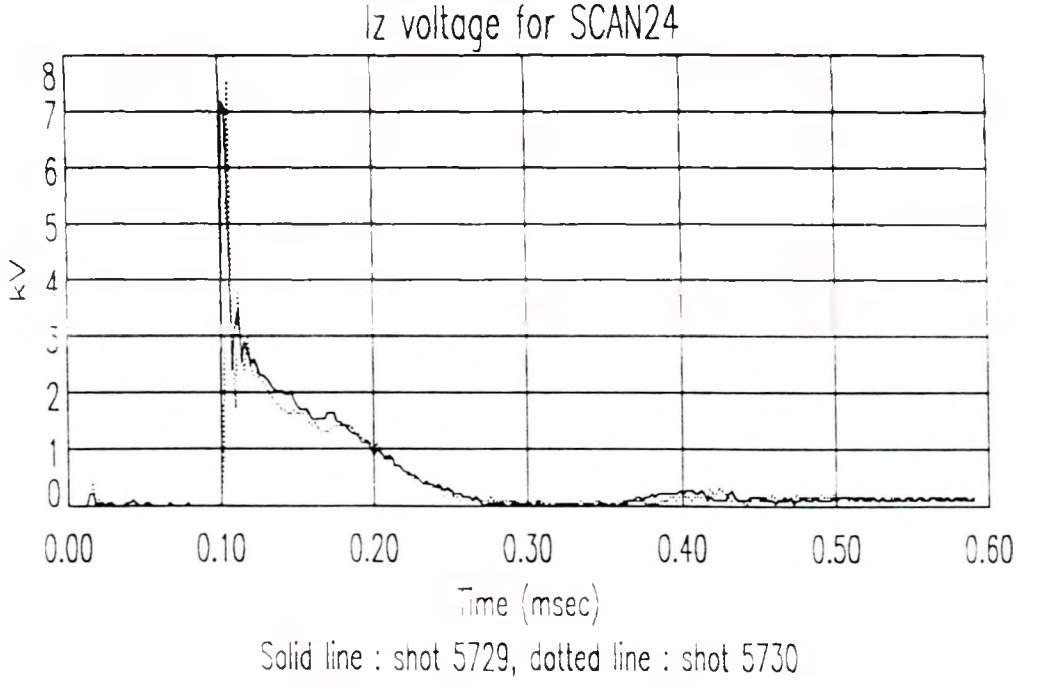

Figure 8.2: Voltage between the anode and cathode of the I_z electrodes for SCAN23 and SCAN24 plasma shots.

rate is largest at that time. The I_z voltage measured is heavily weighted during that time. Small fluctuations in the I_z voltage measurement produce big changes in the helicity injection rate.

There are two dotted and dashed lines for each scan in Fig. 8.3, one has positive values and the other has negative values. The negative curves are obtained when we use the bias flux Ψ_{bias} as $\Psi_{boundary}$. This calculated helicity becomes too small to account for the helicity measured in both cases. When the total poloidal flux Ψ_{total} in an annular ring is used for $\Psi_{boundary}$, we get the positive curves. In the SCAN23 case, when the total helicity Ψ_{total} is used, the helicity injected is almost four times the maximum magnetic helicity measured. Much better agreement is seen between the measured helicity and the helicity calculated from the injection rate for the SCAN24 case before t=0.20 msec.

The I_z voltages are about the same for both cases, but there is more reversal coil current discharged for SCAN23 plasma shots (shown in Fig. 6.1). Effectively, SCAN23 has more helicity injected when compared with the SCAN24 case. However, more magnetic helicity was obtained for SCAN24. It is believed that much of the magnetic helicity was wasted due to the current flowing between the reversal coils and the vacuum vessel for SCAN23 plasma shots. When that current path is blocked and all the current flows into the central region of the vessel, the helicity injected is more efficiently transferred to the plasma.

There is another factor which affects the helicity injection. The injected helicity shown in Fig. 8.3 assumes that the only voltage source is the region of the annular ring containing the I_z electrodes. As described in Chapter 5, an electric field is induced inside the radius of the I_z electrodes and causes a reversed current to flow in the central region of the vessel before the peak of the I_z current. This induced field is another voltage source between the two boundaries and is opposite to the I_z voltage. Effectively, it acts like a "helicity extraction" instead of "helicity injection" mechanism. In SCAN24, more

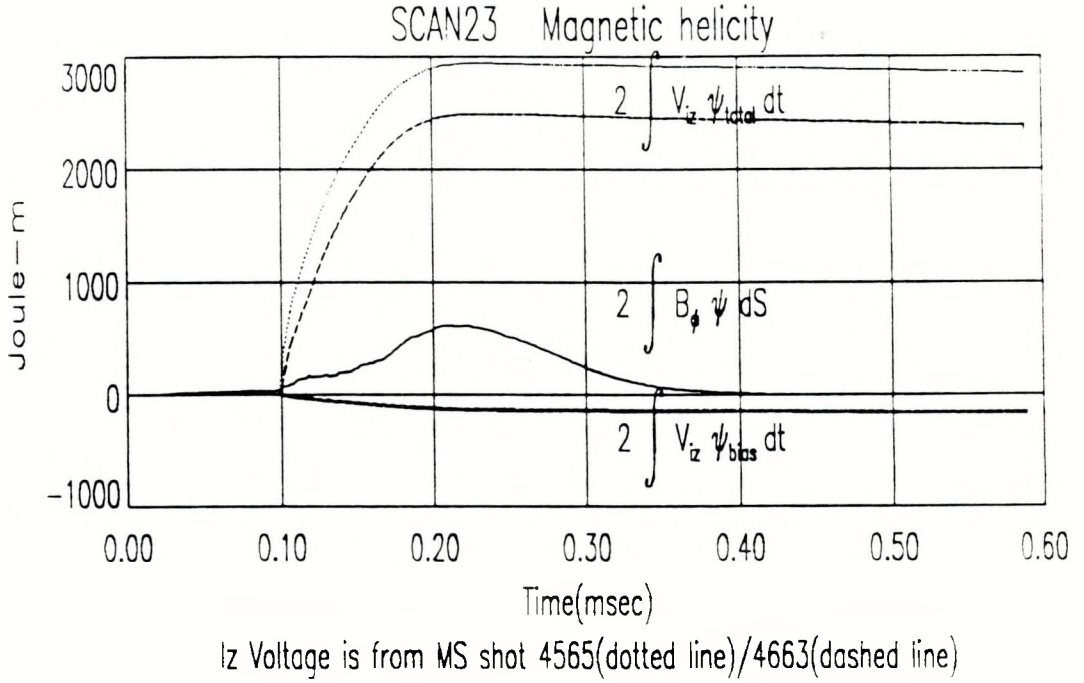

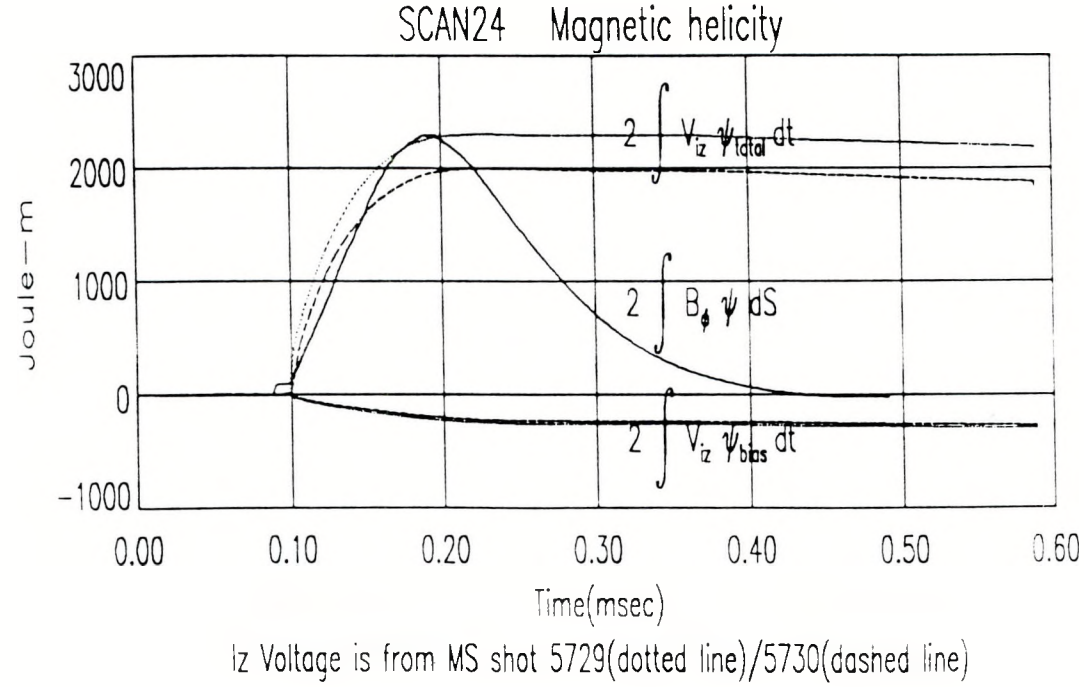

Figure 8.3: Magnetic helicity for SCAN23 and SCAN24 conditions. The solid line is the magnetic helicity calculated with Eqs. (8.14). The dotted lines and dashed lines are the magnetic helicity calculated from the helicity injection rate in Eq. (8.15).

current was flowing in the central region of the vessel. The reversed current disappears much earlier and occurs in a smaller volume (compare Figs. 5.11 and 6.11). The "extraction" effect of the reversed current is smaller for SCAN24 compared with SCAN23.

It has been shown in Chapter 6 that during the formation phase, the ratio of poloidal current I_p to poloidal flux Ψ approaches the eigenvalue k and stays at roughly that same value after the spheromak is formed. In SCAN24, more I_z current is flowing in the central region of the vessel and the poloidal flux increases proportionally. The helicity is proportional to $(\Psi \cdot I_p)$ from Eq. (8.14). The poloidal current increases by about a factor 2 from SCAN23 to SCAN24, and the helicity measured indeed increases by about a factor 4. The helicity measured balanced with the helicity injected in SCAN24.

Scaling with Machine Parameters:

It is interesting to know how the magnetic helicity scales with the MS machine parameters, e.g. bias coil current, reversal coil current and I_z current.

From energy balance: We have observed that the poloidal flux Ψ scales linearly with the poloidal current I_p of the spheromak, and the poloidal current I_p is proportional to the I_z current in the central region of the vessel (comparing SCAN23 and SCAN24). If we keep increasing the I_z current alone, it is possible for the poloidal flux to scale linearly with I_z indefinitely. When we increase the I_z current, the I_z voltage V_{iz} will increase proportionally and the power input P then scales with I_z^2. The magnetic energy W of the plasma scales with B^2 which is proportional to Ψ^2. Therefore, the magnetic energy and the power input both scale with I_z^2.

$$P \propto I_z V_{iz} \propto I_z^2 \quad \text{during the formation} \tag{8.17a}$$

$$W \propto \Psi^2 \propto I_z^2 \quad \text{when the spheromak is formed} \tag{8.17b}$$

From helicity balance: With the aid of Eq. (8.14), the magnetic helicity of the plasma scales with $\Psi \cdot I_p \propto I_z^2$. We have shown that the magnetic helicity injection rate is propotional to the I_z voltage and the poloidal flux $\Psi_{boundary}$ near the tips of the I_z electrodes. The poloidal flux near the tip of the I_z electrodes is mostly produced from the reversal coil current with a small contribution from the bias coil current. From the probe measurements, we have $\Psi_{boundary} \propto 0.008\, I_{rev} - I_{bias}$. For typical plasma shots, $I_{rev} \sim 250$ kA and $I_{bias} \sim 400$ A, therefore, the reversal coil current contributes 84% of $\Psi_{boundary}$.

$$\dot{H} \propto I_z\, \Psi_{boundary} \quad \text{during formation} \tag{8.18a}$$

$$H \propto I_p^2 \propto \Psi^2 \quad \text{when the spheromak is formed} \tag{8.18b}$$

From Eq. (8.17) alone, if we doubled the I_z current, we could produce a plasma with twice as much magnetic flux. From Eq. (8.18b), the magnetic helicity would then increase by a factor 4. However, Eq. (8.18a) indicates that the helicity injection rate only increases by a factor 2. Therefore, the magnetic flux may only increase by a factor of $\sqrt{2}$ if $k = W/H$ is to remain at a constant value. This indicates that some of the energy must be dissipated during the formation phase.

To test the above simplified argument, the reversal coil current was changed while holding I_z and the bias coil current constant. Figures 8.4 and 8.5 show the poloidal flux and the poloidal current for MS shots with two different reversal currents. Typical numbers are listed in Table 8.1.

Before t=0.18 msec, the poloidal current profile on the midplane is about the same in both cases. For the low reversal current case (shot 5728), between t=0.10-0.18 msec, additional poloidal flux is generated after the I_z discharged. After t=0.18 msec, both poloidal flux and poloidal current dropped, and the ratio $\mu_0 I_p/\Psi$ becomes a constant ($\simeq$11 m^{-1}) between t=0.20-0.30 msec (Fig. 8.6).

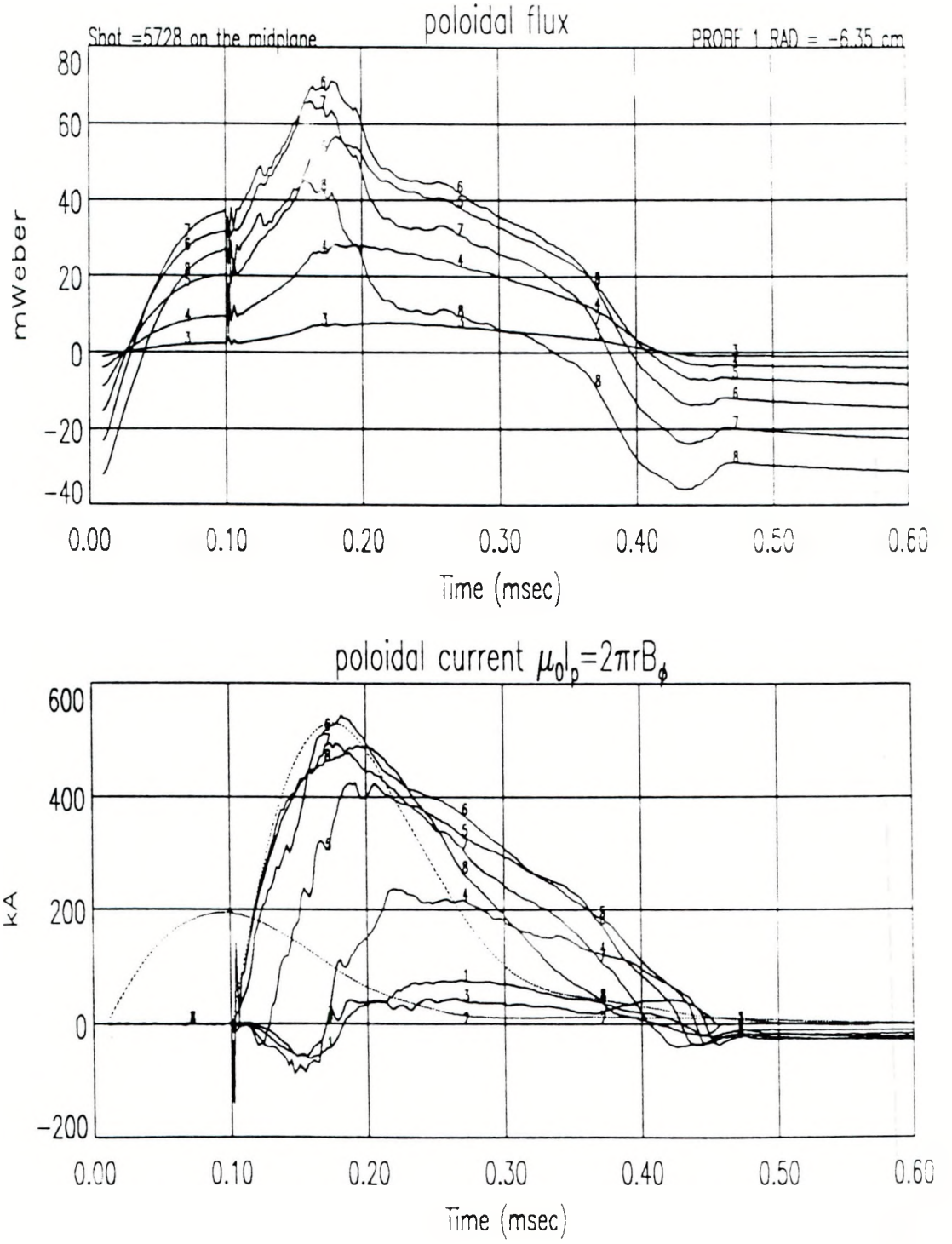

Figure 8.4: Poloidal flux and poloidal current profiles on the midplane for shot 5728. Locations # 1-8 are at r=(-6.35, 0.00, 6.35, 12.7, 19.1, 25.4, 31.8, 38.1) cm.

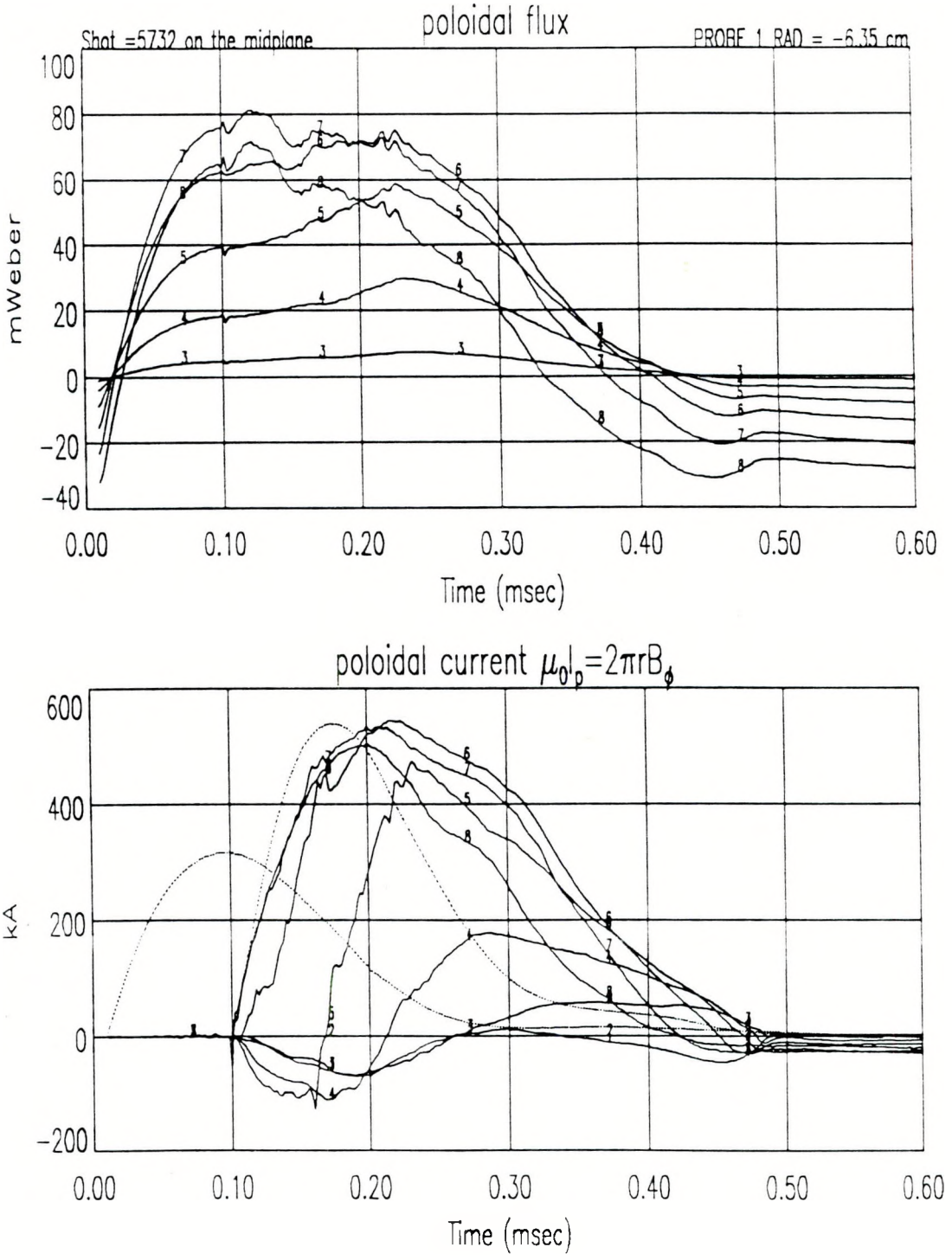

Figure 8.5: Poloidal flux and poloidal current profiles on the midplane for shot 5732. Locations # 1-8 are at r=(-6.35, 0.00, 6.35, 12.7, 19.1, 25.4, 31.8, 38.1) cm.

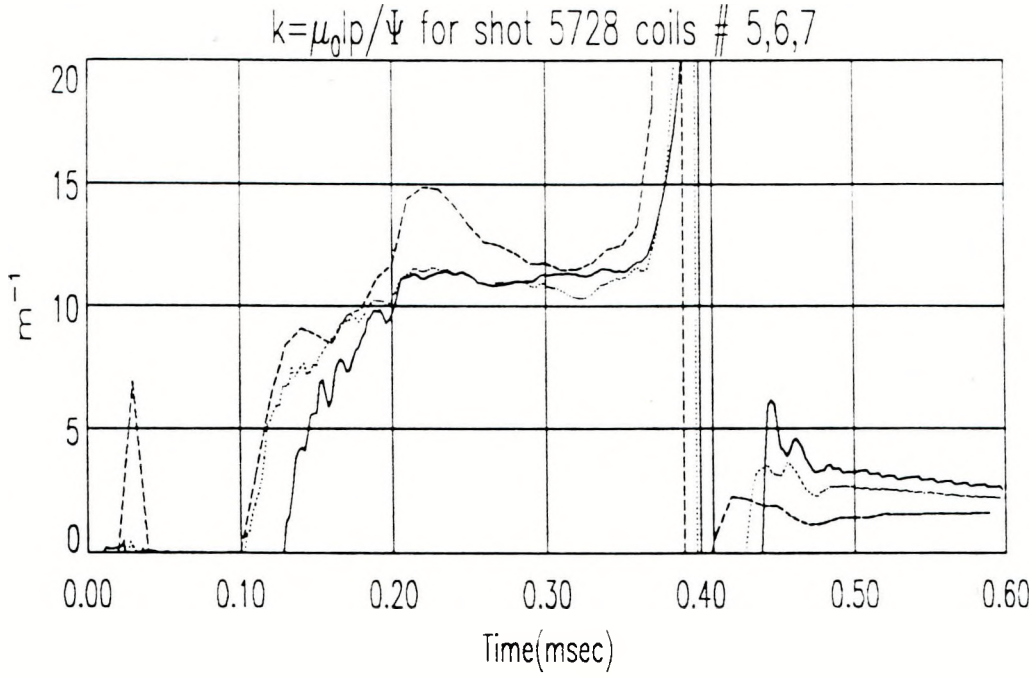

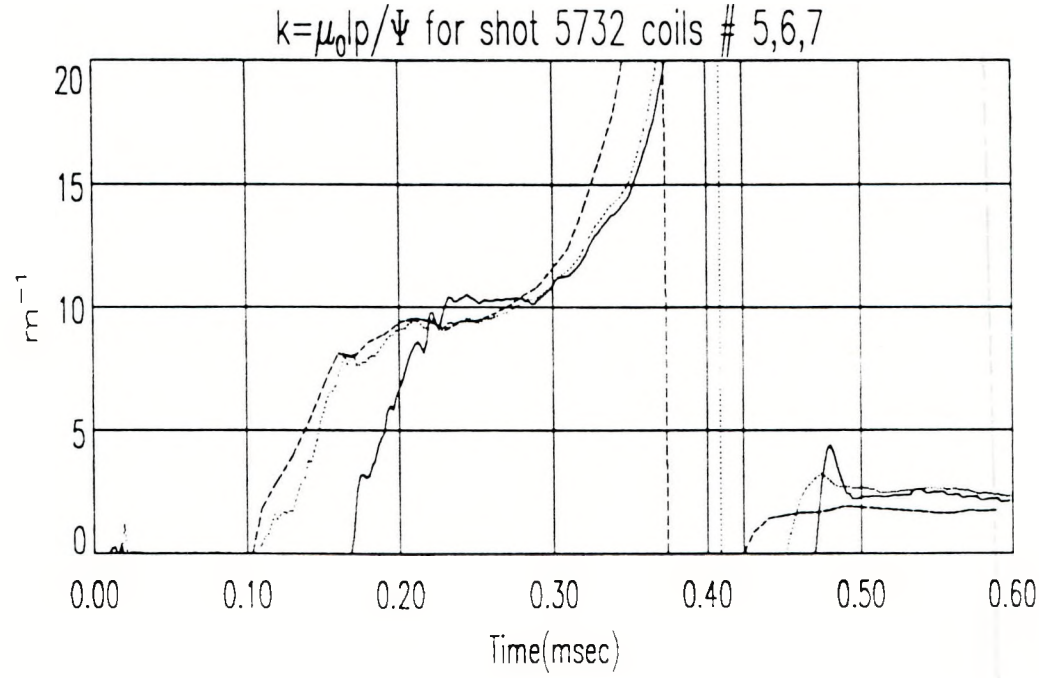

Figure 8.6: $k = \mu_0 I_p/\Psi$ on the midplane for shots 5728 and 5732. Solid, dotted, dashed lines are signals for coils #5, #6 and #7 respectively. Locations # 5-7 are at r=(19.1, 25.4, 31.8) cm.

	5728		5732	
	max. I_p^*	max. Ψ^*	max. I_p^*	max. Ψ^*
t=0.10 (msec)	0	37.4	0	75.8
t=0.18 (msec)	536	70.9	500	73.2
t=0.25 (msec)	398	44.3	505	67.5
max. I_{rev}(kA)	200		318	

Bias current=400 A, max. I_z =535 kA for both shots.
* I_p (kA), Ψ(mWeber)

Table 8.1: Comparison of the poloidal current and poloidal flux for shots 5728 with 5732

For the high reversal current case (shot 5732), the ratio $\mu_0 I_p/\Psi$ starts to approach 10 m^{-1} after the I_z is triggered and stays constant between t=0.20-0.30 msec. More helicity is injected for this shot and more poloidal current is produced when the spheromak formed. From Eq. (8.18), the injection rate increased by about 1.78. Therefore, we may expect I_p to increase by a factor of $\sqrt{1.78} = 1.34$. Between t=0.25-0.30 msec, the ratio of the poloidal currents I_p between the two cases is about 1.27, which is consistent with the scaling rule.

8.4. Helicity Decay

After t=0.25 msec, the I_z voltage drops to about zero (Fig. 8.2) and the helicity injection rate becomes small. The helicity starts to decay due to the finite resistivity of the plasma. Table 8.2 lists the magnetic helicity decay time and the magnetic energy decay time for SCAN23 and SCAN24. We have shown that the volume averaged resistivity is smaller for SCAN24 when compared with SCAN23, so the helicity decays faster for the SCAN23 case. It also shows that the magnetic helicity decays faster than the magnetic energy.

From Eq. (2.9), $W = kH$ for a spheromak in the Taylor's state.

$$\dot{W} = \dot{k}H + k\dot{H}$$
$$\frac{\dot{W}}{W} = \frac{\dot{k}}{k} + \frac{\dot{H}}{H}$$

Decay time of the magnetic helicity (magnetic energy)		
time\ SCAN	SCAN23	SCAN24
t=0.30-0.35 msec	36.6(56.9)	51.9(70.0)
t=0.35-0.40 msec	27.0(58.6)	36.9(70.0)

Table 8.2: Comparison of the magnetic helicity decay time and magnetic energy decay time for SCAN23 and SCAN24.

$$-\frac{1}{\tau_W} = -\frac{1}{\tau_H} + \frac{\dot{k}}{k} \tag{8.19}$$

where τ_W and τ_H are the decay time of the magnetic energy and magnetic helicity respectively. If the spheromak decays with the same boundary, i.e. constant radius separatrix, then $\dot{k} = 0$, and the magnetic energy decays at the same rate as the magnetic helicity. If the separatrix radius becomes smaller as the spheromak decays, $\dot{k}/k > 0$ and $\tau_H < \tau_W$. The magnetic helicity then decays faster than the magnetic energy.

Chapter 9.
Conclusion

This thesis describes the studies done on the magnetic field structure of the MS spheromak. The magnetic field structure of the plasma has been mapped out by arrays of passive magnetic pickup coils. In early work, due to the current flowing from the plasma to the bare metal of the reversal coils, the spheromak produced was forming initially off-center, and then drifting, generally further off center. A symmetric plasma was produced after the reversal coils were completely wrapped with teflon tape to prevent direct contact with the plasma. The teflon tape was covered with Nichrome foil to prevent sputtering, evaporation or gas desorption in the presence of plasma.

The I_z discharge current paths play an important role during the formation phase in MS. It is observed that the I_z current closely follows the poloidal field lines. There are two different paths linking the anode and the cathode electrodes: One inside the inner radius of the reversal coils and the other one between the outer radius of the reversal coils and the vacuum chamber wall. The magnetic field is more than doubled after the current path between the reversal coils and the chamber wall is blocked by two annular glass plates.

It is observed that during the formation phase, the magnetic profile evolves in such a way that the ratio of the poloidal current I_p to poloidal flux Ψ in the plasma approaches a constant value k, $\mu_0 I_p = k\Psi$. This constant k is related to the size of the spheromak produced (k ~10-12 m^{-1} in MS). When the spheromak is formed, the magnetic field configuration is close to the force free or Taylor's minimum energy state, $\mu_0 \vec{J} = k\vec{B}$. The formation process observed is qualitatively similar to the MS formation simulation reported by Guzdar and Finn.[25] The magnetic field then decays exponentially. Comparison of the Grad-Shafranov equilibrium code calculation with the experimental measurement indicated that the magnetic field profile remains close to the equilibrium state during the decay phase.

The maximum poloidal current or maximum poloidal magnetic flux of the spheromak is determined by the magnetic helicity injection mechanism during the formation phase. Due to the gauge problem in the definition of the magnetic helicity for an open field line configuration, the generalized magnetic helicity defined by Finn and Antonsen[50] is adopted for this study. The magnetic helicity injection rate in MS is mostly determined by the I_z voltage and the reversal coil current. However, the I_z current path also influences the magnetic helicity injection. Before our attempts of controlling the I_z current path, the magnetic helicity measured was too small to account for the magnetic helicity injected during the plasma formation. More magnetic helicity is observed after the current path between the reversal coils and the vessel wall is blocked, and the measured magnetic helicity agrees with the magnetic helicity injected.

A spheromak with 10 kG maximum field is produced. However, it is still a radiation dominated cold plasma with electron temperature $\sim$ 15 eV. The limiting factors are the high plasma density (electron density $\sim 6-8\times10^{20}\mathrm{m}^{-3}$) and the presence of low–Z impurities (mainly carbon and oxygen). The volume averaged plasma beta is about 3%. The most recent MS studies have been concentrated on burning through the radiation barrier.

An analytic model which studied the radiation dominated compact toroid has been reported.[22] The condition to burn-through the oxygen radiation barrier at approximately 20 eV is

$$f < 0.026 \left(\frac{\mathrm{B_c\,(Tesla)}}{R\,(\mathrm{m})\, n_e\,(10^{20}\mathrm{m}^{-3})} \right)^2 \qquad (9.1)$$

where n_e is the electron density, $f = n_{oxygen}/n_e$ represents the oxygen impurity level, B_c is the magnetic field at the center of the machine and R is the midplane radius of the separatrix of the plasma. The density limits have been observed in CTX[14] and S-1[15] devices. To overcome the radiation barrier, increasing the B_c/n_e ratio and decreasing the impurity levels would be required.

The impurity levels in the experiment are not known, however, the 0-D power balance code calculation[26] indicated the oxygen impurity in MS to be

about 1.5% of the electron density. For electron density equal to $6 \times 10^{20} m^{-3}$, B_c =1 Tesla and R=0.4 m, this impurity level is three times higher than the burn through requirement. The electron density measured[26] corresponds to several times the amount of D_2 gas puffed into the chamber and does not scale with the amount of gas puffed. This indicates that most of the density is coming from inside the chamber, either from the chamber walls or from the electrode tips. Recent efforts are devoted to the Ti gettering technique to reduce the plasma density and the impurity concentrations.

References

1. Edward Teller, *Fusion*, Vol. 1, Academic Press Inc., New York (1981).
2. W. M. Stacey, *Fusion Plasma Analysis*, John Wiley & Sons. New York (1981).
3. G. J. Pert, *Plasma Physics and Nuclear Fusion Research*, Academic Press. New York (1981).
4. K. Miyamoto, *Plasma Physics for Nuclear Fusion*, MIT Press, Cambridge (1980).
5. D. M. Meade and the TFTR group, Recent TFTR Results, in 13^{th} *International conference on Plasma Physics and Controlled Nuclear Fusion Research*, Washington DC (1990).
6. P. Rebut and JET team, Recent JET Results and Future Prospects, in 13^{th} *International conference on Plasma Physics and Controlled Nuclear Fusion Research*, Washington DC (1990).
7. D. J. Sigmar *et al.*, Physics Objectives and Design of CIT, in 13^{th} *International conference on Plasma Physics and Controlled Nuclear Fusion Research*, Washington DC (1990).
8. M. Bussac, H. P. Furth, M. Okabayashi, M. Rosenbluth and M. Todd. *Plasma Physics and Controlled Fusion Research: Proceedings of the seventh International Conference on Plasma Physics and Controlled Nuclear Fusion*,Nucl. Fusion Supplement 3, 249 (1979).
9. G. C. Goldenbaum, J. H. Irby, Y. P. Chong, G. W. Hart, Phys. Rev. Lett. 44, 393 (1980).
10. M. Yamada, H. P. Furth, W. Hsu, A. Janos, S. Jardin, M. Okabayashi, J. Sinnis, T. H. Stix and K. Yamazaki, Phys. Rev. Lett. 46, 188 (1981).

11. W. C. Turner, E. H. A. Granneman, C. W. Hartman, D. S. Prono, J. Taska and A. C. Smith, J. Applied Phys. 52, 175 (1981).

12. T. R. Jarboe, Cris W. Barnes, D. A. Platts and B. L. Wright CPPCF 9, 161 (1985).

13. J. A. Antoniades, C. Chin-Fatt, A. W. DeSilva, G. C. Goldenbaum, R. A. Hess and R. S. Shaw, "MS– The University of Maryland Spheromak Fusion Experiment" University of Maryland technical report – Laboratory for Plasma Research (1986).

14. J. C. Fernández, C. W. Barnes, T. R. Jarboe, I. Henins, H. W. Hoida, P. L. Klingner, S. O. Knox, G. J. Marklin and B. L. Wright, Nucl. Fusion 28, 1555 (1988).

15. F. M. Levinton, D. D. Meyerhofer, R. M. Mayo, A. C. Janos, Y. Ono, Y. Ueda and M. Yamada, Nucl. Fusion 30, 871 (1990).

16. T. Uyama, Y. Honda, M. Nagata, M. Nishikawa, A. Ozaki, N. Satomi and K. Watanabe, Nucl. Fusion 27, 799 (1987).

17. M. N. Rosenbluth and M. N. Bussac, Nucl. Fusion 19, 489 (1979).

18. J. M. Finn and W. M. Manheimer, Phys. Fluid 24, 1336 (1981).

19. G. C. Goldenbaum, Phys. Scripta T2/2, 359 (1982).

20. M. Yamada *et al.*, Investigation of Confinement Properties of Spheromak, 12^{th} *International Conference on Plasma Physics and Controlled Nuclear Fusion Research*, France (1988).

21. W. C. Turner, G. C. Goldenbaum, E. H. A. Granneman, J. H. Hammer, C. W. Hartman, D. S. Prono and J. Taska, Phys. Fluid 26, 1965 (1983).

22. S. P. Auerbach, Phys. Fluids 27, 1108 (1982).

23. G. W. Hart, Ph.D. thesis, University of Maryland (1983).

24. T. A. Peyser, Ph.D. thesis, University of Maryland (1987).

25. P. N. Guzdar, J. M. Finn, K. W. Whang and A. Bondeson, Phys. Fluids 28, 3154 (1985).

26. A. Filuk, Ph.D. thesis, University of Maryland (1991).

27. M. Berger and G. Field, J. Fluid Mech. 147, 133 (1984).

28. M. Ono, C. J. Greene, D. Darrow, C. Forest, H. Park and T. H. Fox, Phys. Rev. Lett. 59, 2165 (1987).

29. D. S. Darrow, M. Ono, C. B. Forest, G. J. Greene, Y. S. Hwang and H. K. Park, Phys. Fluids B 2, 1415 (1990).

30. A. H. Boozer, Phys. Fluids 29, 4123 (1986).

31. J. M. Finn, Phys. Fluids 29, 2630 (1986).

32. M. R. Brown and P. M. Bellan, Phys. Fluids B 2, 1306 (1990).

33. J. B. Taylor Rev. Mod. Phys. 58, 741 (1986).

34. Moffatt, H. K., *Magnetic field generation in Electrically conducting Fluids*, Cambridge University Press, New York (1978).

35. M. N. Bussac, H. P. Furth, M. Okabayashi, M. N. Rosenbluth, A. M. M. Todd, *Plasma Physics and Controlled Nuclear Fusion Research*, 3, 249 (1978).

36. V. D. Shafranov, *Review of Plasma Physics* (translated from the Russian), edited by Acad. M. A. Leontovich, Consultants Bureau, New York 2, 106, (1966).

37. J.-L. Gauvreau, G. C. Goldenbaum, C. Chin-Fatt, A. W. DeSilva and R. A. Hess, Bull. Am. Phys. Soc. 35, 2056 (1990).

38. H. R. Griem, *Plasma Spectroscopy*, McGraw-Hill, New York (1964).

39. S. C. Jardin and U. R. Christensen, Nucl. Fusion 21, 1665 (1981).

40. G. C. Goldenbaum, H. Bruhns, C. Chin-Fatt, Y. P. Chong, A. W. DeSilva, H. R. Grie G. W. Hart, R. A. Hess, J. H. Irby, R. S. Shaw and Z. Y. Zhu, Nucl. trum. Methods 207, 129 (1983).

41. A. C. Janos, in *Proceedings of the Eighth U.S. Japan Workshop on Compact Toroid Research*, Osaka, Japan (1986).

42. S. C. Jardin, A. C. Janos and M. Yamada, Nucl. Fusion 26, 647 (1986).

43. Kozo Katayama and Makoto Katsurai, Phys. Fluids 29, 1939 (1986).

44. B. Barrow and G. C. Goldenbaum, Phys. Rev. Lett 64, 1269 (1990).

45. G. W. Hart, A. Janos, D. D. Meyerhofer and M. Yamada, Phys. Fluid 29, 1994 (1986).

46. A. Janos, Phys. Fluid 29, 3342 (1986).

47. F. F. Chen, *Plasma Physics and Controlled Fusion*, Plenum Press, New York (1983).

48. W. H. Press, B. P. Flannery, S. A. Teukolsky and W. T. Vetterling, *Numerical Recipes : The Art of Scientific Computing*, Cambridge University Press, New York (1986).

49. T. Jensen and M. S. Chu, Phys. Fluids 27, 2881 (1984).

50. J. M. Finn and T. M. Antonsen Jr., Comments Plasma Phys. 9, 111 (1985).